A Novel Microfluidic Concept for Bioanalysis using Controlled Recirculating Flows

Dissertation submitted to the Faculty of Sciences of the University of Neuchâtel, to
obtain the degree of Doctor of Science by
Gian-Luca Lettieri

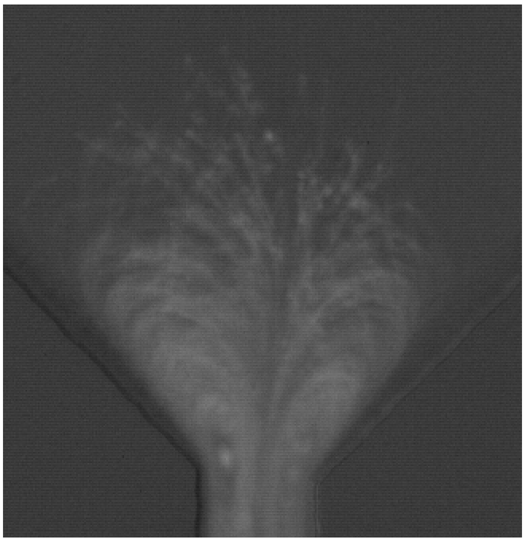

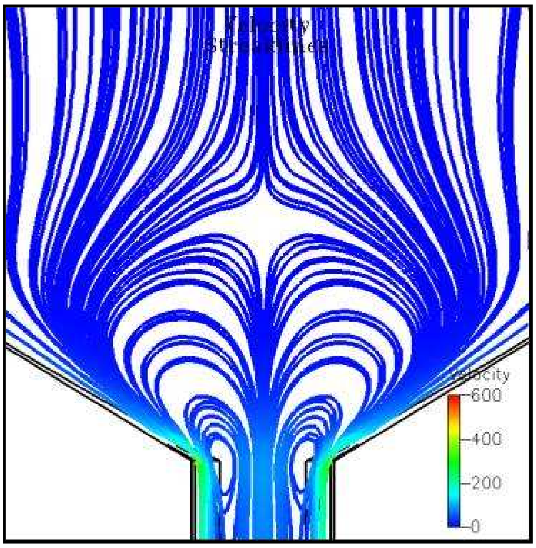

Institute of Microtechnology
University of Neuchâtel
Rue Jaquet-Droz 1, CH-2007 Neuchâtel
Switzerland
2004

IMPRIMATUR POUR LA THESE

A novel microfluidic concept for bioanalysis using controlled recirculating flows

M. Gian-Luca LETTIERI

UNIVERSITE DE NEUCHATEL

FACULTE DES SCIENCES

La Faculté des sciences de l'Université de
Neuchâtel, sur le rapport des membres du jury

Mme E. Verpoorte, MM. N. de Rooij (directeur de thèse),
T. Ward et G. Stemme (Stockholm S)

autorise l'impression de la présente thèse.

Neuchâtel, le 9 février 2004

La doyenne:

Martine Rahier

Abstract

There are only a few examples in which beads are employed for heterogeneous assays on microfluidic devices, because of the difficulties associated with packing and handling these in etched microstructures. To date, the approach generally adopted for on-chip, bead-based chemistry has been to fabricate a retaining feature in the microchannel to confine beads to a specific location within the microfluidic network. This thesis is devoted to the development of a microfluidic device for the capture, preconcentration, and controlled manipulation of particles and biomolecules in etched microchannels using fluid flows only. The working principle of the microfluidic device relies on the formation of controlled micrometer size recirculating flows at low Reynolds number ($Re < 0.1$). The chips feature planar diverging and converging channel elements connected by narrow microchannels. Creation of bi-directional liquid movement by opposing electro-osmotic and pressure-driven flows leads to the generation of controlled recirculating flows at these elements. The presence of a bi-directional flow at diverging and converging elements produces adverse pressure gradients at these locations, forcing the flow to reverse direction streamline. Simulation and visualisation with small polymer beads (1 - 6 μm) provided firm evidence of recirculating flows in these devices, at low Re. Generally, this type of flow behaviours, is expected only at much higher Re. Based on these observations, a theoretical model was developed to predict the formation of the controlled recirculating flows. This model indicates that particles and biomolecular species are trapped when all three contributions to their velocity (electro-osmotic and electrophoretic mobility, applied pressure) lead to an overall velocity of zero. It was shown that beads can actually be captured in the controlled rotating flow patterns. The clusters of freely moving beads that result can be perfused sequentially with different solutions, since a net flow still exists at zero net bead velocity. Binding curves were determined for the reaction of streptavidin-coated beads and fluorescein-labeled biotin. Similarly, molecules of λDNA (48 kbp) could be trapped, preconcentrated and

released without issues of clogging, showing a possible applicability for DNA extraction. Preliminary experiments indicated that preconcentration of fluorescein-labelled biotin can be also achieved using the recirculating flow devices, demonstrating another potential of this biomolecular-and-particle-handling approach for bioanalysis.

1 Introduction

In 1947, the bipolar transistor, one of the most important semiconductor devices, was invented by a research team at Bell Laboratories. Thus the microelectronics field was born, and a few decades later, computers the size of a room can be reduced to the size of a notebook. In the late 80's, an exciting new field, based on microelectronics technology and involving chemistry, biology, microtechnology and physics, was born with the introduction of the micro total analysis system concept [1].

This chapter first introduces the concept of the micro total analysis systems and the transport mechanisms involved in these systems, and discusses the applicability of fluid mechanics from macroscopic systems to microfluidic systems. It then gives an overview of the state-of-the-art for bead-based analysis and DNA extraction. The chapter ends with the objectives and outline of this thesis.

1.1 The Micro Total Analysis Systems Concept

Over the past decade, a need for miniaturization in laboratories for low cost, fast and sensitive measurements at low concentration has developed within the field of chemical production, DNA analysis, drug discovery and environmental analysis [2-4]. The idea is to place all the functions carried out in a laboratory onto a chip (Lab-on-a-chip). In 1992, the integration of capillary electrophoresis (CE) separation onto planar chips was reported by Manz et al. [5], giving rise to the first examples of miniaturized total chemical analysis systems (μTAS) [1, 5-9]. Since then, the μTAS has not ceased to evolve toward a real lab-on-a-chip, with the integration of sample handling such as valves and pumps [10-14], chemical mixing and reaction [11, 15-17], PCR [18, 19], DNA separation [20-24] or cell handling [25]. Basically, a μTAS device improves the performance of an analysis due to its size. The importance of μTAS devices can be judged to some extent by comparison with their conventional analogues. Miniaturization mainly leads to the reduction of reagent consumption, greater separation efficiencies and, most important, reduced analysis time. On the other hand, the applicability of μTAS for biochemical analysis is also determined by considerations such as improved analytical performance, component integration, increased throughput and automation.

1.2 Transport Mechanisms

The potential benefits of microfluidic devices for many applications in the life sciences have been demonstrated, particularly with respect to fast analysis and high throughput. Most successful examples to date have employed structures based on microchannel networks formed in planar glass or plastic substrates, in which solutions are pumped using applied electric fields [26-28]. The mechanism underlying this pumping principle is electro-osmosis, a bulk flow which originates at the surface of charged substrates like glass and requires no pumps, valves or other moving parts [16]. An additional advantage of using electric fields is that species may also be separated electrophoretically as a function of their different charge-to-mass ratios [2, 16, 26-28]. Many chip-based applications therefore involve capillary electrophoresis (CE) in free solution.

The first μTAS were fabricated on glass or silicon wafers and then used for electro-osmotic pumping and electrophoretic separation (silicon quickly proved to be impracticable since this application uses high electric fields, see below). Electro-osmosis can be described as the motion of a liquid over a charged surface caused by an electric field. This motion is also called electro-osmotic flow (EOF). A prerequisite for electro-osmosis is the presence of immobilized surface charges on the capillary wall in contact with an electrolyte solution [16]. The microchannel walls of glass materials, made of SiO_2, have silanol (SiOH) groups on their surface. The silanol groups remain mainly protonated in acidic media ($pH < 7$) producing a low surface charge on the microchannel walls. Since the pKa of silanol groups is roughly 6, increased deprotonation is observed when the medium is basic. As a result, the microchannel walls are covered by fixed, negatively charged SiO^- groups. These fixed negative charges attract positive ions present in the buffer solution, generating a static layer referred to as the Stern Layer. A second layer of positively charged ions, more diffuse and separated from the Stern layer by a plane of shear, is generated. This diffuse layer is referred as the Helmholtz Layer [29]. Application of an external electric field results in a net migration toward the cathode (negative electrode) of the positive ions present in the Helmholtz layer. Consequently, flow moves first in a thin annular region defined by the Helmholtz layers towards the negative electrode. The constant motion of the annular region is transferred to the rest of the medium present in the microchannel by viscous forces. The transfer process is established on a time scale between 100 μs and 1 ms. The resulting flow is the EOF, which ideally produces a flat flow profile. The velocity due to electro-osmotic pumping is given by the Smoluchowski equation [16, 29]:

$$u_{EOF} = \mu_{EOF} E \qquad \textbf{Eq 1.1}$$

where μ_{EOF} is the electroosmotic mobility of the solution [cm^2/Vs] and E [V/m] the electric field. The μ_{EOF} is given by the electrical potential, ζ, in the shear plane between the fixed and the flowing layers of liquid in the double layer at the surface:

$$\mu_{EOF} = \frac{\varepsilon\zeta}{4\pi\eta} \qquad \textbf{Eq 1.2}$$

where ε [A·s/V·m] is the solution's dielectric constant and η [Pa·s] the solution viscosity. The potential, ζ, is called the zeta potential. The EOF strongly depends on ζ. For example, an increase of the ionic strength of the buffer induces a lower ζ and, hence, a lower μ_{EOF}. On the other hand, the EOF is generated uniformly in the direction of the E and no pressure drop is observed in the microchannel (this is true only for $Re < 1$ according to [30]). EOF can then be used to transport fluid, and especially charged species, with minimal hydrodynamic forces in microfluidic devices. In this case, the charged species will move relative to the EOF, allowing electrophoretic separation. Moreover, EOF is easy to implement.

When charged species are under the influence of an axial *E,* the resulting ion migration velocity, u_{ep}, is given by:

$$u_{ep} = \mu_{ep} E = \frac{z_i e}{\chi_i} E \qquad \textbf{Eq 1.3}$$

where μ_{ep} is the electrophoretic mobility, $z_i e$ the net charge on ion *i* and χ_i the friction coefficient of species *i.* Assuming spherical ions of radius, r_i, the friction coefficient can be written:

$$\chi_i = 6\pi r_i \eta \qquad \textbf{Eq 1.4}$$

Separation of different species can then be achieved by the exploiting differential migration velocities dictated by the net charges and the friction coefficient of the individual species. (Note that the ionic strength of the buffer can influence the charge in the case of beads). The net velocity of an analyte is the sum of the electrophoretic velocity and the electro-osmotic velocity, $u_{ep} + u_{EOF}$. The simplicity of electrophoretic separation, the high resolution [7] and the possibility of performing parallel separations makes the EOF transport mechanism very attractive. However, EOF is not compatible with high ionic-strength buffers, which limit the *E* used due to Joule heating and reduce μ_{EOF} by reducing ζ. Moreover, EOF is not compatible with silicon substrates due to its requirement for high voltages, since silicon is a semi-conductor.

Fluid flow in microchannel networks can also be achieved by employing pressure-driven flows. Pressure-driven flows within microfluidic devices can be generated by external means (hydrostatic pressure, syringe pumps or peristaltic pumps) or by integrated transducers. Some examples of integrated micro-pumps for the generation of pressure-driven flows are discussed in section 1.3. In EOF, a plug-like profile is observed, whereas flow induced by pressure yields a parabolic flow profile. Pressure-driven flows can then be an alternative to electro-osmotic pumping only to some extent, depending on the application. The fact that pressure-driven flows induce parabolic flow profiles renders the separation of analytes less efficient, since the dispersion of the solute zone is increased [31]. The analytical behavior of pressure-driven flows in microchannels are discussed more in detail in section 1.3 and Chapter 3.

1.3 Fluid Mechanics: From Macrofluidic to Microfluidic

Historically, the first microfluidic devices fabricated using microelectronics technology were investigated in the 70's at Stanford University [32] and at IBM [33], where a silicon-based gas chromatograph and an inkjet printer nozzle were developed, respectively. Since then, several categories of microfluidic devices have been developed for different applications. One of these categories is related to microfluidic devices for flow control, and includes passive/active valves and micropumps [10, 13, 34-36], reactors and mixers [37, 38], inkjet [39] and pressure flow sensors [40]. In these microfluidic systems, the theory of fluid mechanics for macroscopic pipe systems can be used to calculate liquid flow parameters such as pressure drop. However, it was observed that not all of macroscopic fluid mechanics can be applied to microfluidic systems [41-43]. This is essentially due to the Reynolds number, as discussed below.

1.3.1 The Reynolds Number [44]

A viscous flow, that is, a flow where the effects of viscosity are important, is classified as either a laminar flow or a turbulent flow. In a laminar flow, the streamlines never intersect (Figure 1.1 *(a)*). A laminar flow may be unsteady (time dependent) or steady. In a turbulent flow, velocity and pressure show random variation with time and space coordinates (Figure 1.1 *(b)*). In macroscopic pipe systems, no general analysis of fluid motion yet exists. There are certain known particular solutions and a lot of experimental data, especially for diffuser and nozzle elements. The reason is that a profound change in fluid behaviour occurs at certain Reynolds numbers. The flow ceases to be laminar and becomes turbulent. The changeover is called transition to turbulence (Figure 1.1 *(b)*).

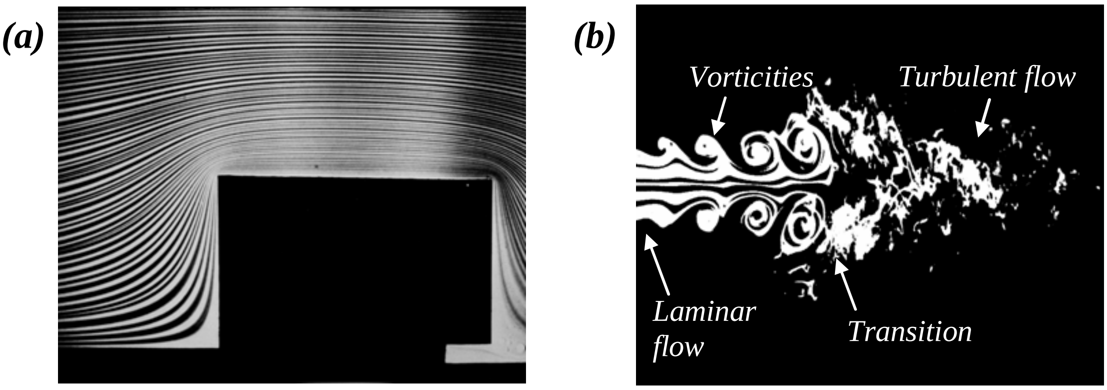

Figure 1.1
(a) Creeping flow past a rectangular block (Re < 1). (b) Instability of air flowing from a circular tube (Re = 10000) [45].

Transition depends upon many effects, e.g., wall roughness or fluctuation in the inlet stream. The primary parameter which describes transition is the Reynolds number, Re, which is defined by:

$$\mathrm{Re} = \frac{ud\rho}{\eta} \qquad \textbf{Eq 1.5}$$

where *u* is the average stream velocity [m/s], ρ is the solution density (kg/m^3) and *d* the diameter of the channel [m]. The Re can be regarded as a ratio of the inertial force to the viscous force and is a dimensionless parameter. To determine whether a given flow is laminar or turbulent in macroscopic systems, the Re is evaluated and compared to the transitional Reynolds number, Re_t, 2300 [44]. For very low Re (0< Re < 1), flow is laminar. Inertia effects are negligible and a viscous creeping flow is observed. For 1 < Re < 2300, flow is laminar and above 2300, the flow is considered turbulent and inertial forces dominate over the viscous forces.

In the early 90’s, it was demonstrated that the Re_t for macroscopic pipe systems can not always be used for microfluidic systems to determine the flow regime [41]. In their study, Gravesen et al. observed that none of the microfluidic devices considered operated in the region of fully developed turbulent flow but in regions where viscous losses dominate or regions where inertial losses dominate.

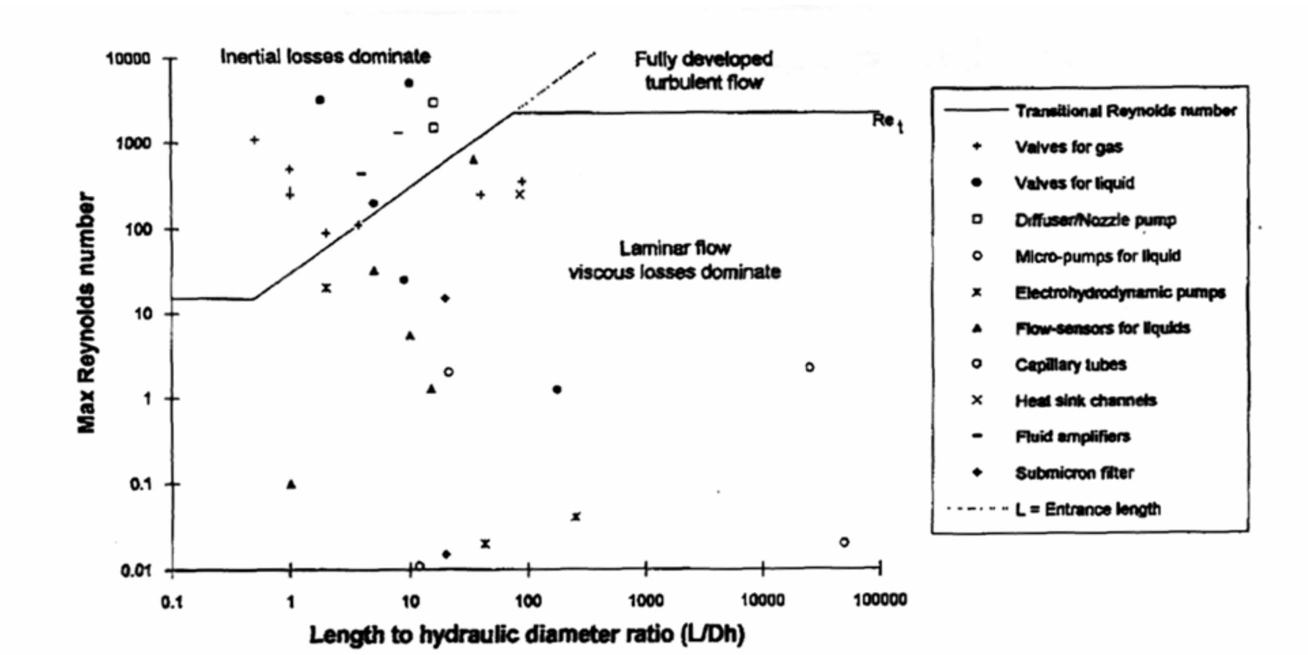

Figure 1.2
Reynolds number map for different microfluidic devices[41].

Figure 1.2 shows the maximum Re plotted as a function of the ratio of the length of the channel and the hydraulic diameter (D_H = 4x (wetted perimeter/ cross-section area), see Chapter 2). Therefore, the Re_t in certain microfluidic systems have little relevance. The main reason is that the length of the element in the direction of the flow can still be shorter than the length for fully developed laminar or turbulent flow (see Figure 1.1 *(b)*). However, alternative values of the transitional number were introduced which depend on the ratio between the length of the channel, L, and the hydraulic diameter. According to [41], for $1 < L/D_H < 70$ the transition number is estimated as:

$$\mathrm{Re}_t \cong 30\frac{L}{D_H},\ 1 < L/D_H < 70 \tag*{\textbf{Eq 1.6}}$$

1.3.2 Energy Equation, Head Loss and Minor Loss [44]

In many fluid flows, useful forms of energy (kinetic energy and potential energy) and flow work are converted into unusable energy forms (internal energy or heat transfer) [46]. Energy losses are due to two effects: viscosity causing internal friction (solid walls introduce friction) and changes in channel geometry inducing flow separation (Figure).

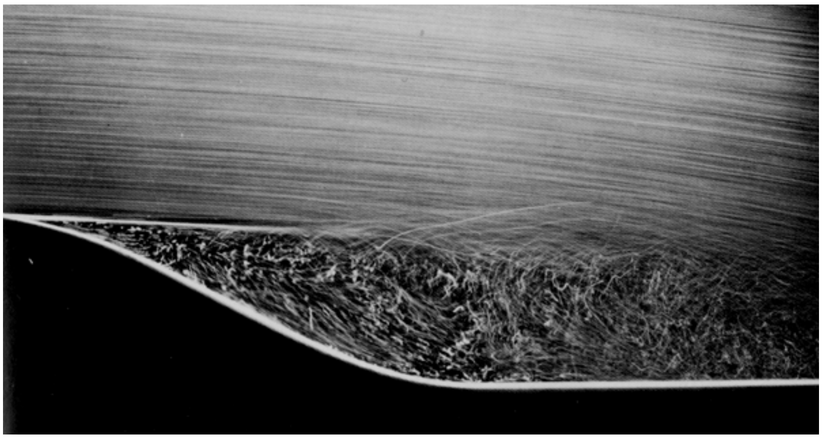

Figure 1.3
Laminar separation of a liquid flow from a curved wall (Re = 20,000)[45].

Consider a situation where the flow is steady and incompressible, and the losses are negligible (frictionless flow, no change in channel geometry) in a channel with one entrance and one exit. The energy equation is given by:

$$\left(\frac{p}{\rho g}+\frac{u^2}{2g}+Z\right)_{in}=\left(\frac{p}{\rho g}+\frac{u^2}{2g}+Z\right)_{out} \qquad \textbf{Eq 1.7}$$

where p is the pressure [Pa], g the acceleration due to gravity [kg·m/s^2] and Z the height difference between the inlet and the outlet [m]. (The energy equation takes the same form as the Bernouilli equation which is, however, a momentum equation.) Thus, if losses are neglected, the kinetic and the potential energy are conserved. If the energy losses are not negligible, the energy equation for a steady and incompressible flow is given by:

$$\left(\frac{p}{\rho g}+\frac{u^{2}}{2g}+Z\right)_{in}=\left(\frac{p}{\rho g}+\frac{u^{2}}{2g}+Z\right)_{out}+\Delta h_{tot} \qquad \textbf{Eq 1.8}$$

where the head loss Δh_{tot} is introduced. The head loss is referred to as a head since it has the dimension of length. Most of the internal flow in macrofluidic problems and some microfluidic problems can be solved with the help of Eq 1.8. In this work, diffuser-like elements are employed. The aim of the next two sections is to give a brief overview of how problems related to this particular geometry are treated in both the macroscopic and microscopic cases.

1.3.3 Flow in Diffusers and Nozzles in Macroscopic Systems

The first known diffusers were designed by the Romans (circa 100 A.D.) [44]. In this period, water was distributed to homes of the wealthy via an aqueduct system. Water flowed continuously and the cost of the water was based upon flow rate. Some enterprising Roman discovered that if he flared the outlet of the pipe, his flow rate increased without increasing his cost. Hence, from necessity, the diffuser was invented.

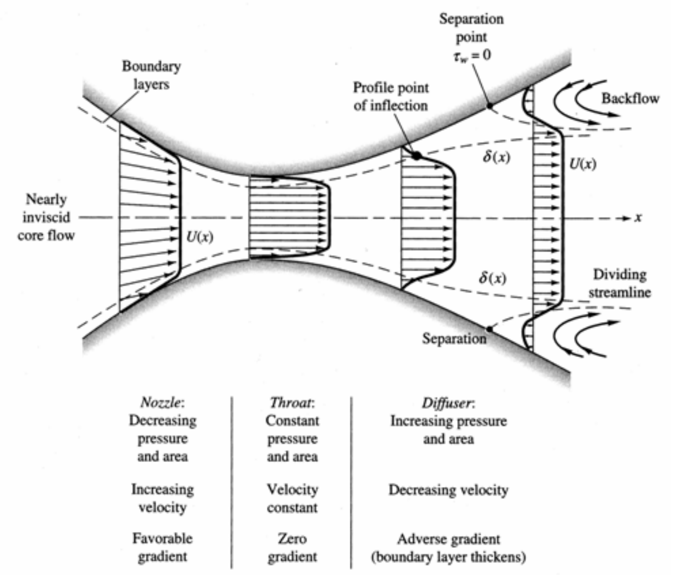

Figure 1.4
Pressure-driven flow through a nozzle and a diffuser illustrating the possible region of flow separations [44].

A diffuser is a fluidic element whose cross-section increases gradually, whereas a nozzle has a gradual contracting cross-section. Diffuser elements are used to reduce the flow velocity in order to recover the pressure head of the flow. The performance of a diffuser is evaluated by the pressure-recovery coefficient, Cp. The higher the Cp value, the better is the diffuser performance. The Cp is limited by the fact that flow can separate (stall) in a diffuser depending on the diffuser geometry. Prandtl [44] showed that flow separation is induced by excessive momentum loss near the wall in a boundary layer trying to move downstream against increasing pressure. This situation of increasing pressure is called an adverse pressure gradient. Consider a pressure-driven flow through a nozzle and a diffuser as shown in Figure 1.4. At the nozzle element, no separation is observed because the pressure gradient is favorable. The diffuser induces a decrease of the velocity and an increase of pressure, leading to an adverse pressure gradient. If the opening angle of the diffuser is too large, the adverse pressure gradient becomes too great and flow can separate from one or both walls. When flow separates, a backflow is produced, leading to an increase of pressure losses. Cp in this case is small. This situation is referred to as the stall region of the diffuser. (In this case, it is assumed that no separation is observed at the entrance of the narrower channel separating the nozzle and the diffuser. However, flow separation can also occur at the entrance of the narrow channel [43].)

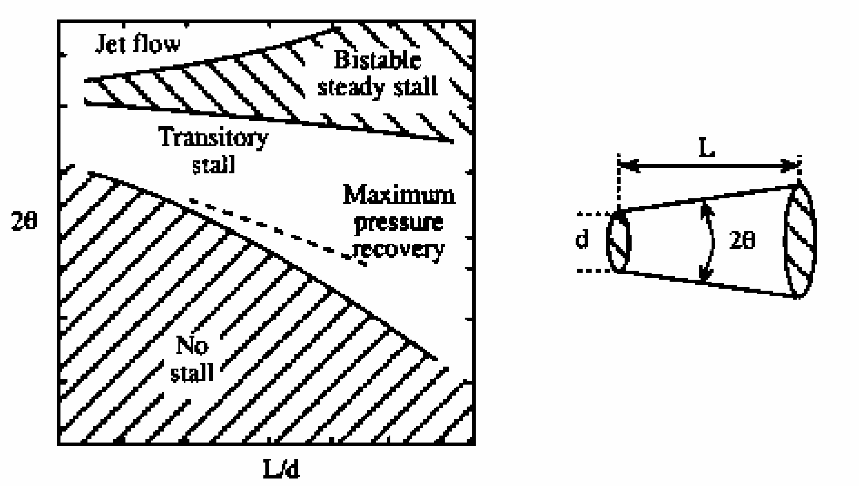

Figure 1.5
Stability map for diffuser elements [44].

In 1962, Fox and Kline [44] published a complete stability map as shown in Figure 1.5. There are basically four types of flow that can occur in a diffuser, as shown inFigure 1.5. Best performance, i.e. highest Cp, occurs in the transitory stall region where the flow is unsteady. In the no-stall region, flow is steady and viscous and no flow separation is observed. In the bistable steady-stall region, a steady bistable stall can flip-flop from one part of the diffuser wall to another, and Cp is low. In the fourth pattern, the jet flow region, the flow separates almost completely from the walls of the diffuser, and the Cp is extremely poor.

When calculating flow rate in ducts of varying cross-section, energy losses due to flow separation have to be taken into account in addition to losses due to the viscosity of the fluid. These additional losses are referred to as minor losses and are expressed by a dimensionless constant, the coefficient of loss, *K*:

$$K = \frac{h_m}{u^2 / 2g} = \frac{\Delta p}{\frac{1}{2}\rho u^2} \qquad \textbf{Eq 1.9}$$

where h_m is the head loss due to minor losses and Δp the pressure drop through the system. The pressure recovery value is related to the *K* by the relation:

$$K = 1 - \left(\frac{A_{in}}{A_{out}} \right)^2 - Cp \qquad \textbf{Eq 1.10}$$

The total head loss across a duct with a gradual expansion or contraction is then given by the sum of the head loss due to fluid friction, h_f, and to minor losses, h_m:

$$\Delta h_{tot} = h_f + h_m \qquad \textbf{Eq 1.11}$$

Generally, the values of *K* and consequently the total head loss across a system of non-uniform cross-section, have to be determined experimentally [44].

1.3.4 Minor Losses in Microfluidic Systems : Examples

In microfluidic applications, the micron-size depth of microchannels results in very small Re. Therefore, in general, creeping flows are observed in microfluidic channels, with fully attached flow even around sharp corners. An interesting example of creeping flow that exhibits no separation when encountering a cylindrical obstruction can be found in [47], where a particle image velocimetry (PIV) system is used to visualize the flow pattern. In most μTAS applications, the Re is below 1 and rarely above 100. However, under certain specific flow conditions, flow separation, inducing eddies or vortices, can occur in microchannels. One of the first flow separations inducing Moffatt's eddy [48], visualized with the help of 0.9-μm fluorescent beads in microfluidic devices, at relatively low Re ($12 < \mathrm{Re} < 50$) was performed by Pfahler [42].

Another example where flow separation in microfluidic devices is observed at relatively low Re ($1 < Re < 500$) are the valveless micropumps which consist of channels with direction-dependent flow resistances (diffuser and nozzle elements) [13, 43]. As for macroscopic fluidic systems, the design of diffuser/nozzle microchannel elements is challenging, since no general diffuser theory exists due to the complicated flow behaviour. During the last years, a growing interest for valveless micropumps, using diffuser and nozzle elements as directing flow elements, has driven researchers to investigate and to elaborate some theory for these types of microfluidic systems. In general, the approach to develop a theoretical model for these types of microfluidic devices is to use common laws for macroscopic systems, taking into account that the Re_t is not the same as for macroscopic systems (see section 1.3.1). Semi-empirical analytical expressions incorporating the loss coefficient, *K*, have been presented for these types of devices. In these cases, the flow losses are integrated over the length with varying cross-section [43, 49]. However, even if these theoretical models fit well with experimental data, they are generally over simplified to be useful for design optimization; CAD tools are thus considered as a possible alternative [43]. Simulations and experimental results reported in these studies demonstrated that minor losses had to be taken into account in order to estimate the possible flow-directing capability and the performance of the diffuser/nozzle elements. In particular, simulations performed by Olsson et al. showed that gross flow separation can be induced for $Re = 460$ in the case of nozzle elements [43]. However, in these valveless micropump systems, the Re are larger than 1, and turbulent flows are often obtained and even preferred to laminar flows, which could induce stall with subsequent low Cp.

An example where gas flow separation may occur at $Re \cong 0.05$ was reported by Li et al. [50]. They observed that a flow of nitrogen gas passing through a constriction inserted into the fluid stream could induce the generation of micro vortex motions upstream and downstream of the obstruction.

There is a category of microfluidic devices, working at low Re, that tries to benefit from the generation of eddies and vortex motion, namely the microfluidic mixers. Micromixer devices are used in microfluidic applications for the rapid homogenisation of solutions of reagents in chemical reactions, for example [37]. Indeed, since low Re are the norm in microfluidic devices for biochemical applications, the mixing is accomplished by diffusion. The mixing time can be decreased by using special designs, or by the use of external pumps or internal moving parts which, however, render the system more complicated and bulky [37]. Another way of improving the mixing time was suggested by Stroock et al., who use a chaotic mixer at low Re ($0 < Re < 100$). In their approach, circulatory flows are generated due to the presence of bas-relief structures (ridges) on the floor of the microchannel [15]. Concerning EOF in microchannels, Yang et al. showed that separation can occur at a 90° bend at $Re \cong 5.2$ [30] and Santiago showed the generation of vorticity in EOF [51].

1.4 Bead-based Analysis and DNA Extraction: State-of-the-art

In this work, new approaches for doing bead-based assay on-chip and DNA preconcentration and extraction will be introduced. Sections 1.4.1 and 1.4.2 give a brief overview of the state-of-the-art for these two topics.

1.4.1 On-Chip Bead-Based Material for Heterogeneous Assay

Micron-size polystyrene beads have been used in medical diagnostics in so-called agglutination tests since the middle of twentieth century [52]. Since then, bead technology has progressed to the point that it has become attractive for many biomedical applications [53]. Microfluidic platforms for heterogeneous analysis, in which biospecific molecules are immobilized on a surface to capture the analyte of interest in solution, are still rare. This is due in part to the added development work involved if microchannel surfaces are to be reproducibly and effectively modified [54-57]. The use of bead-based materials could be a viable alternative, as they are ideal reagent delivery vehicles providing large reactive surface areas and have become omnipresent in biomedical applications like immunoassay [58]. One of the reasons that also makes beads attractive is that a large variety of beads are available on the market, and most manufacturers can provide beads designed for highly specific uses [58]. Beads can be found on the micron and submicron-size (they are made by emulsion polymerization [52]) and present therefore large reactive surface areas. However, beads have not often been employed in flow systems, conventional or integrated, for heterogeneous assay [59-63]. This is especially true in microfluidic structures because of the difficulties associated with packing and handling beads in etched channels, despite possible benefits related to facilitated fluid handling and accelerated analysis. To date, the approach generally adopted for on-chip, bead-based chemistry has been to fabricate a retaining feature or “weir” in the microchannel to confine beads to a specific location within the microfluidic network [63-69]. The resulting structures must fulfil the dual purpose of holding back particles while at the same time allowing solution to be delivered from a separate, particle-free compartment on the chip. Other approaches consist of using ultrasonic standing waves or magnetic fields to trap beads, but these require the integration of a transducer for wave- or magnetic-field generation [70-73].

1.4.2 On-chip DNA Analysis

Developments in microfluidics have opened up the possibility to investigate on-chip DNA analysis with the purpose of developing fast, cost-effective, high-throughput separation methods. Obtaining DNA information involves extraction and purification of the DNA from whole blood, amplification by the polymerase chain reaction (PCR), and DNA separation [74]. Efforts to integrate these three fundamental steps into a single microfluidic platform are ongoing. Efforts are mainly focused on DNA amplification by PCR [18, 75-78] and separation [21, 23, 24], with successful results [79]. The integration of both PCR and DNA separation on a single microchip was also successfully demonstrated [19, 79-81]. Interestingly, DNA purification has received less attention. DNA purification on the macroscale (precipitation in organic solvents, centrifugation [82]) still requires several hours, making irrelevant fast DNA separation on an electrophoretic microfluidic device (< 100 s). The surrounding matrix of DNA can consist of a complex mixture of cell wall, proteins, peptides, and lipids. The purification of DNA is thus required before performing PCR because efficient and reliable amplification of target DNA sequences is dependent on the presence of a sufficient amount of relatively pure template DNA. DNA purification (including desalting) is also needed prior to separation. Practically, a miniaturized DNA protocol must accomplish extraction and purification in as few steps as possible and should minimize dilution effects and contamination [83]. Recently, methods based on micro solid-phase extraction (μSPE) exploiting DNA adsorption on silica beads from different matrices [83, 84] showed promising results. In these systems, beads need to be packed in a localized region within the microfluidic device. In their approach, Wolf et al. combined sol-gel with silica beads to pack the beads in a selected region of their microchip. They also investigated the “weir” approach [69] to pack the silica beads. However, they observed that bead packing caused several problems like back-pressure, unsteady flow patterns or eventual destruction of the devices. In the same approach, Ceriotti et al. showed better results by improving the geometry of the device but still reported problems of back-pressure [85]. In this specific case, platinum electrodes were also integrated in order to preconcentrate the eluted DNA, with the aim of avoiding sample dilution [85-87]. Other approaches for bead packing methods for DNA purification are under investigation. Most of these approaches used the bead-trapping methods introduced in the previous section [88]. Note that in the literature, there is one example of total DNA analysis on-chip [89]

1.5 Outline of the Thesis

The objectives of this thesis focus on the development of a bioanalytical microfluidic device dedicated to particle handling using fluid flows only. The microfluidic platform should permit the selective trapping and the (pre-)concentration of freely moving particles of various types such as micro latex beads, DNA molecules and smaller biomelecules.

This thesis begins with the introduction of the different chip layout geometries used and dimensions of these microfluidic platforms. In the same chapter, instrumentation and chemical methods are presented.

The second part of the present study investigates the consequences on the average flow velocity and fluid flow patterns when an EOF is opposed to a pressure-driven flow (PF). A simple theoretical model, based on classical fluid mechanics and on the assumption that minor losses can be neglected, is first developed for determining the average velocity when EOF and PF co-exist in opposite directions. Current monitoring, consisting of measuring the variation of the resistivity of the buffer across the channel as a function of time, flow visualization with micro beads (Chapter 3) and Computational Fluid Dynamics (CFD) tools (Chapter 4) are used to investigate flows under these conditions. In Chapter 3, current monitoring results are compared with theory for devices with uniform cross-section or containing gradual or sudden expansion and contraction elements. A significant discrepancy in the average linear velocities is observed for the latter, due to the generation of steady and fully developed recircualting flows at the diverging and converging elements at very low Re ($Re < 0.1$). This result is confirmed by streamline visualization with beads. Moreover, in the same chapter, it is demonstrated that the recirculating flow of beads can be precisely tuned by controlling one (or both) of the two transport components. The development of a simple model that takes into account the minor losses induced by these recirculating flows and to predict them is developed in this chapter. The mechanism and the conditions necessary for the generation of the controlled recirculating flows, elaborated in Chapter 3, are confirmed and developed in Chapter 4 with the help of simulation tools.

The third part of this study focuses on the biochemical applications employing controlled recirculating flows. Chapter 5 shows the potential of recirculating flows inmicrofluidic devices by performing a heterogeneous reaction involving streptavidin-coated beads of 2 μm as reagent and fluorescein-labeled biotin as analyte. It is demonstrated that the freely moving beads can be trapped and preconcentrated while being continuously perfused by different solutions (buffer and analyte). Dose-response and calibration curves are constructed, and a kinetic study of the dynamic binding of the streptavidin and biotin is performed. The forward rate constant of the streptavidin-coated beads is extracted using a 1st-order binding model. The forward constant values obtained are in good agreement with the literature for the heterogeneous binding of streptavidin with biotin.

Chapter 6 describes experiments carried out with DNA molecules and fluorescein-labelled biotin using recirculating-flows in microfluidic devices. It is demonstrated that the DNA can be trapped, preconcentrated and released without any issues of clogging. This flexibility and the conditions under which the DNA trapping is performed (similar to those for beads) make this potentially interesting for on-chip DNA extraction and concentration. In the same chapter, preliminary experiments of small-biomolecule preconcentration using recirculating flows are presented.

1.6 References

[1] A. Manz, N. Graber, and H. M. Widmer, "Miniaturized total chemical-analysis systems - a novel concept for chemical sensing," *Sensors and Actuators B-Chemical*, vol. 1, pp. 244-248, 1990.

[2] S. C. Jakeway, A. J. de Mello, and E. L. Russell, "Miniaturized total analysis systems for biological analysis," *Fresenius Journal of Analytical Chemistry*, vol. 366, pp. 525-539, 2000.

[3] D. Figeys and D. Pinto, "Lab-on-a-chip: A revolution in biological and medical sciences," *Analytical Chemistry*, vol. 72, pp. 330A-335A, 2000.

[4] G. J. M. Bruin, "Recent developments in electrokinetically driven analysis on microfabricated devices," *Electrophoresis*, vol. 21, pp. 3931-3951, 2000.

[5] A. Manz, D. J. Harrison, E. Verpoorte, J. C. Fettinger, A. Paulus, H. Ludi, and H. M. Widmer, "Planar chips technology for miniaturization and integration of separation techniques into monitoring systems - Capillary electrophoresis on a chip," *Journal of Chromatography*, vol. 593, pp. 253-258, 1992.

[6] D. J. Harrison, K. Seiler, A. Manz, and Z. Fan, "Chemical Analysis and Electrophoresis Systems Integrated on Glass and Silicon Chips," presented at IEEE Solid-State Sensor and Actuator Workshop, Hilton Head Island, South Carolina, 1992.

[7] D. J. Harrison, A. Manz, Z. H. Fan, H. Ludi, and H. M. Widmer, "Capillary electrophoresis and sample injection systems integrated on a planar glass chip," *Analytical Chemistry*, vol. 64, pp. 1926-1932, 1992.

[8] E. M. J. Verpoorte, B. H. Van der Schoot, S. Jeanneret, A. Manz, H. M. Widmer, and N. F. de Rooij, "A Three Dimentional Micro Flow System for a Multistep Chemical Analysis," presented at Transducers'93, 1993.

[9] S. C. Jacobson, R. Hergenroder, A. W. Moore, and J. M. Ramsey, "Precolumn Reactions With Electrophoretic Analysis Integrated On a Microchip," *Analytical Chemistry*, vol. 66, pp. 4127-4132, 1994.

[10] W. K. Schomburg, J. Fahrenberg, D. Maas, and R. Rapp, "Active valves and pumps for microfluidics," *Journal of Micromechanics and Microengineering*, vol. 3, pp. 216-218, 1993.

[11] M. Elwenspoek, T. S. J. Lammerink, R. Miyake, and J. H. J. Fluitman, "Towards integrated microliquid handling systems," *Journal of Micromechanics and Microengineering*, vol. 4, pp. 227-245, 1994.

[12] S. Shoji and M. Esashi, "Microflow devices and systems," *Journal of Micromechanics and Microengineering*, vol. 4, pp. 157-171, 1994.

[13] A. Olsson, P. Enoksson, G. Stemme, and E. Stemme, "A valve-less planar pump isotropically etched in silicon," *Journal of Micromechanics and Microengineering*, vol. 6, pp. 87-91, 1996.

[14] V. Gass, B. H. v. d. Schoot, S. Jeanneret, and N. F. d. Rooij, "Micro liquid handling using a flow-regulated silicon pump," *Journal of Micromechanics and Microengineering*, vol. 3, pp. 214-215, 1993.

[15] A. D. Stroock, S. K. W. Dertinger, A. A., M. I., S. H. A., and G. M. Whitesides, "Chaotic mixer for microchannels," *Science*, vol. 295, pp. 647-651, 2002.

[16] A. Manz, C. S. Effenhauser, N. Burggraf, D. J. Harrison, K. Seiler, and K. Fluri, "Electroosmotic pumping and electrophoretic separation for miniaturised chemical analysis systems," *J. Micromech. Microeng.*, vol. 4, pp. 257-265, 1994.

[17] U. D. Larsen, J. Branebjerg, and G. Blankenstein, "Fast mixing by parallel multilayer lamination," *Analytical Methods & Instrumentation*, vol. Special Issue uTAS '96, pp. 228-230, 1996.

[18] R. P. Oda, M. A. Strausbauch, A. F. R. Huhmer, N. Borson, S. R. Jurrens, J. Craighead, P. J. Wettstein, B. Eckloff, B. Kline, and J. P. Landers, "Infrared-mediated thermocycling for ultrafast polymerase chain reaction amplification of DNA," *Analytical Chemistry*, pp. 4361-4368, 1998.

[19] J. Khandurina, T. E. McKnight, S. C. Jacobson, L. C. Waters, R. S. Foote, and J. M. Ramsey, "Integrated system for rapid PCR-based DNA analysis in microfluidic devices," *Analytical Chemistry*, vol. 72, pp. 2995-3000, 2000.

[20] C. S. Effenhauser, A. Paulus, A. Manz, and H. M. Widmer, "High-speed separation of antisense oligonucleotides on a micromachined capillary electrophoresis device," *Analytical Chemistry*, vol. 66, pp. 2949-2953, 1994.

[21] Y. N. Shi, P. C. Simpson, J. R. Scherer, D. Wexler, C. Skibola, M. T. Smith, and R. A. Mathies, "Radial capillary array electrophoresis microplate and scanner for high-performance nucleic acid analysis," *Analytical Chemistry*, vol. 71, pp. 5354-5361, 1999.

[22] G. W. Slater, S. Guillouzic, M. G. Gauthier, J. F. Mercier, M. Kenward, L. C. McCormick, and F. Tessier, "Theory of DNA electrophoresis," *Electrophoresis*, vol. 23, pp. 3791-3816, 2002.

[23] J. Han and H. G. Craighead, "Characterization and optimization of an entropic trap for DNA separation," *Anal. Chem.*, vol. 74, pp. 394-401, 2002.

[24] J. Han and H. G. Craighead, "Separation of long DNA molecules in a microfabricated entropic trap array," *Science*, vol. 288, pp. 1026-1029, 2000.

[25] P. C. H. Li and D. J. Harrison, "Transport, manipulation, and reaction of biological cells on- chip using electrokinetic effects," *Analytical Chemistry*, vol. 69, pp. 1564-1568, 1997.

[26] D. J. Harrison, K. Fluri, K. Seiler, Z. H. Fan, C. S. Effenhauser, and A. Manz, "Micromachining a miniaturized capillary electrophoresis-based chemical analysis system on a chip," *Science*, vol. 261, pp. 895-897, 1993.

[27] C. S. Effenhauser, A. Manz, and H. M. Widmer, "Glass chips for high-speed capillary electrophoresis separations with submicrometer plate heights," *Analytical Chemistry*, vol. 65, pp. 2637-2642, 1993.

[28] S. C. Jacobson, R. Hergenroder, L. B. Koutny, and J. M. Ramsey, "High-speed separations on a microchip," *Analytical Chemistry*, vol. 66, pp. 1114-1118, 1994.

[29] J. T. G. Overbeek, E. J. W. Verwey, and K. van Nes, "Electrokinetic Phenomena," in *Theory of the stability of lyophobic colloids; the interaction of sol particles having an electric double layer.*: Elsevier Pub. Co., 1948, pp. 195-213.

[30] R.-J. Yang, L.-M. Fu, and Y. C. Lin, "Electroosmotic flow in microchannels," *Journal of Colloid and Interface Science*, vol. 239, pp. 98-105, 2001.

[31] R.-L. Chien and J. W. Parce, "Multiport flow-control system for lab-on-a-chip microfluidic devices," *Fresenius Journal of Analytical Chemistry*, vol. 371, pp. 106-11, 2001.

[32] S. C. Terry, J. H. Jerman, and J. B. Angel, "A gas chromatographic air analyzer fabricated on a silicon wafer," *IEEE Trans. Electron. Devices*, vol. 26, pp. 1880-1886, 1979.

[33] E. Bassous, H. H. Taub, and L. Kuhn, "Ink jet printing nozzle arrays etched in silicon," *Applied Physics Letters*, vol. 31, pp. 135-137, 1977.

[34] F. P. Man, C. H. Mastrangelo, M. A. Burns, and D. T. Burke, "Microfabricated plastic capillary systems with photo-definable hydrophilic and hydrophobic regions," presented at Transducers Conference 1999, Sendai, Japan, 1999.

[35] T. Gerlach, "Microdiffusers as dynamic passive valves for micropump applications," *Sensors and Actuators A*, vol. 69, pp. 181-191, 1998.

[36] D. Maillefer, H. van Lintel, G. Rey-Mermet, and R. Hirschi, "A high-performance silicon micropump for an implantable drug delivery system," presented at MEMS '99, Orlando, Fl., USA, 1999.

[37] C. Erbacher, F. G. Bessoth, M. Busch, E. Verpoorte, and A. Manz, "Towards integrated continuous-flow chemical reactors," *Mikrochimica Acta*, vol. 131, pp. 19-24, 1999.

[38] F. G. Bessoth, A. J. deMello, and A. Manz, "Microstructure for efficient continuous flow mixing," *Analytical Communications*, vol. 36, pp. 213-215, 1999.

[39] C. D. Meinhart and H. Zhang, "The flow structure inside a microfabricated inkjet printhead," *Journal of Microelectromechanical Systems*, vol. 9, pp. 67-75, 2000.

[40] M. Boillat, B. van der Schoot, P. Arquint, and N. F. de Rooij, "Controlled Liquid Dosing in Micro-Instruments," presented at SPIE Conference on "Microfluidic Devices and Systems II", Santa Clara, California, 1999.

[41] P. Gravesen, J. Branebjerg, and O. S. Jenson, "Microfluidics - A Review," *Journal of Micromechanics and Microengineering*, vol. 3, pp. 168-182, 1993.

[42] J. N. Pfahler, "Thesis: Luiquid transport in micron and submicron size channels," in *Mechanical Engineering and Applied Mechanics*. Pennsylvania: University of Pennsylvania, 1992.

[43] A. Olsson, G. Stemme, and E. Stemme, "Numerical and experimental studies of flat-walled diffuser elements for valve-less micropumps," *Sensors and Actuators A*, vol. 84, pp. 165-175, 2000.

[44] F. M. White, *Fluid Mechanics*, 4th ed. New York: McGraw-Hill, 1999.

[45] M. Van Dyke, *An album of fluid motion*, 5th Edition ed. California, USA: The parabolic press, 1997.

[46] M. C. Potter and D. C. Wiggert, *Mechanics of Fluids*, 1997.

[47] J. G. Santiago, S. T. Wereley, C. D. Meinhart, D. J. Beebe, and R. J. Adrian, "A particle image velocimetry system for microfluidics," *Experiments in Fluids*, vol. 25, pp. 316-319, 1998.

[48] H. K. Moffatt, "Viscous and resistive eddies near a sharp corner," *Fluid Mech.*, vol. 18, pp. 1-18, 1963.

[49] M. Heschel, M. Müllenborn, and S. Bouwstra, "Fabrication and characterization of truly 3-D diffuser/nozzle microstructures in silicon," *Jounal of Microelectromechanical Systems*, vol. 6, pp. 41-47, 1997.

[50] X. D. Li, W. Y. Lee, M. Wong, and Y. Zohar, "Gas flow in constriction microdevices," *Sensors and Actuators A*, vol. 83, pp. 277-283, 2000.

[51] J. G. Santiago, "Electroosmotic flows in microchannels with finite inertial and pressure forces," *Analytical Chemistry*, vol. 73, pp. 2353-2365, 2001.

[52] S. Slomkowski, T. Basinka, and B. Miska, "New types of microspheres and microspheres-related materials for medical diagnostics," *Polymer for advanced technologies*, vol. 13, pp. 906-918, 2002.

[53] S. P. Radko and A. Chrambach, "Separation and characterization of sub-µm- and µm-sized particles by capillary zone electrophoresis," *Electrophoresis*, vol. 23, pp. 1957-1972, 2002.

[54] A. Dodge, K. Fluri, E. Verpoorte, and N. F. de Rooij, "Electrokinetically driven microfluidic chips with surface modified chambers for heterogeneous immunoassays," *Analytical Chemistry*, vol. 73, pp. 3400-3409, 2001.

[55] E. Eteshola and D. Leckband, "Development and characterization of an ELISA assay in PDMS microfluidic channels," *Sensors and Actuators B-Chemical*, vol. 72, pp. 129-133, 2001.

[56] T. Yang, S.-y. Jung, H. Mao, and P. S. Cremer, "Fabrication of phospholipid bilayer-coated microchannels for on-chip immunoassays," *Analytical Chemistry*, vol. 73, pp. 165-169, 2001.

[57] V. Linder, E. M. J. Verpoorte, W. Thormann, N. F. de Rooij, and H. Sigrist, "Surface biopassivation of replicated poly(dimethylsiloxane) microfluidic channels and application to heterogeneous immunoreaction with on-chip fluorescence detection," *Analytical Chemistry*, vol. 73, pp. 4181-4189, 2001.

[58] M. B. Meza, "Bead-based HTS applications in drug discovery," *Drug Discovery Today*, vol. 1, pp. 38-41, 2000.

[59] C. H. Pollema and J. Ruzicka, "Flow-injection renewable surface immunoassay - a new approach to immunoanalysis with fluorescence detection," *Analytical Chemistry*, vol. 66, pp. 1825-1831, 1994.

[60] M. Mayer and J. Ruzicka, "Flow injection based renewable electrochemical sensor system," *Analytical Chemistry*, vol. 68, pp. 3808-3814, 1996.

[61] J. Ruzicka, "Bioligand interaction assay by flow injection absorptiometry using a renewable biosensor system enhanced by spectral resolution," *Analyst*, pp. 1617-1623, 1998.

[62] B. Willumsen, G. D. Christian, and J. Ruzicka, "Flow injection renewable surface immunoassay for real time monitoring of biospecific interactions," *Analytical Chemistry*, vol. 69, pp. 3482-3489, 1997.

[63] K. Sato, M. Tokeshi, T. Odake, H. Kimura, T. Ooi, M. Nakao, and T. Kitamori, "Integration of an immunosorbent assay system: analysis of secretory human immunoglobulin A on polystyrene beads in a microchip," *Analytical Chemistry*, vol. 72, pp. 1144-1147, 2000.

[64] C. Wang, R. Oleschuk, F. Ouchen, J. Li, P. Thibault, and D. J. Harrison, "Integration of immobilized trypsin bead beds for protein digestion within a microfluidic chip incorporating capillary electrophoresis separations and an electrospray mass spectrometry interface," *Rapid Communications in Mass Spectrometry*, vol. 14, pp. 1377-83, 2000.

[65] A. B. Jemere, R. Oleschuk, J. Taylor, and D. J. Harrison, "Microchip-based selective preconcentration using protein A immunoaffinity chromatography," presented at µTAS 2001, Monterey, California, 2001.

[66] H. Andersson, W. van der Wijngaart, and G. Stemme, "Micromachined filter-chamber array with passive valves for biochemical assays on beads," *Electrophoresis*, vol. 22, pp. 249-257, 2001.

[67] A. B. Jemere, R. Oleschuk, F. Ouchen, F. Fajuyigbe, and D. J. Harrison, "An integrated solid-phase extraction system for sub-picomolar detection," *Electrophoresis*, vol. 23, pp. 3537-3544, 2002.

[68] H. Andersson, W. van der Wijngaart, P. Enoksson, and G. Stemme, "Micromachined flow-through filter-chamber for chemical reactions on beads," *Sensors and Actuators B*, vol. 67, pp. 203-208, 2000.

[69] R. D. Oleschuk, L. L. Shultz-Lockyear, Y. Ning, and D. J. Harrison, "Trapping of bead-based reagents within microfluidic systems: On-chip solid-phase extraction and electrochromatography," *Analytical Chemistry*, vol. 72, pp. 585-590, 2000.

[70] K. Yasuda, "Non-destructive, non-contact handling method for biomaterials in micro-chamber by ultrasound," *Sensors and Actuators B*, vol. 64, pp. 128-135, 2000.

[71] J.-W. Choi, K. W. Oh, A. Han, C. A. Wijayawardhana, C. Lannes, S. Bhansali, K. T. Schlueter, W. R. Heineman, H. B. Halsall, J. H. Nevin, A. J. Helmicki, H. T. Henderson, and C. H. Ahn, "Development and characterization of microfluidic devices and systems for magnetic bead-based biochemical detection," *Biomedical Microdevices*, vol. 3, pp. 191-200, 2001.

[72] Z. H. Fan, S. Mangru, R. Granzow, P. Heaney, W. Ho, Q. Dong, and R. Kumar, "Dynamic DNA hybridization on a chip using paramagnetic beads," *Analytical Chemistry*, vol. 71, pp. 4851-4859, 1999.

[73] G. Jiang and D. J. Harrison, "mRNA isolation in a microfluidic device for eventual integration of cDNA library construction," *Analyst*, vol. 125, pp. 2176-2179, 2000.

[74] I. Kheterpal and R. A. Mathies, "Capillary array electrophoresis DNA sequencing," *Analytical Chemistry*, vol. 71, pp. 31A-37A, 1999.

[75] M. U. Kopp, A. J. de Mello, and A. Manz, "Chemical amplification: Continuous-flow PCR on a chip," *Science*, vol. 280, pp. 1046-1048, 1998.

[76] M. A. Northrup, B. Benett, D. Hadley, P. Landre, S. Lehew, J. Richards, and P. Stratton, "A miniature analytical instrument for nucleic acids based on micromachined silicon reaction chambers," *Analytical Chemistry*, vol. 70, pp. 918-922, 1998.

[77] P. K. Yuen, L. J. Kricka, P. Fortina, N. J. Panaro, T. Sakazume, and W. Peter, "Microchip module for blood sample preparation and nucleic acid amplification reactions," *Genome Research*, vol. 11, pp. 405-412, 2001.

[78] P. Wilding, M. A. Shoffner, and L. J. Kricka, "PCR in a silicon microstructure," *Clinical Chemistry*, vol. 40, pp. 1815-1818, 1994.

[79] E. Verpoorte, "Microfluidic chips for clinical and forensic analysis," *Electrophoresis*, vol. 23, pp. 677-712, 2002.

[80] M. A. Burns, B. N. Johnson, S. N. Brahmasandra, K. Handique, J. R. Webster, M. Krishnan, T. S. Sammarco, P. M. Man, D. Jones, D. Heldsinger, C. H. Mastrangelo, and D. T. Burke, "An integrated nanoliter DNA analysis device," *Science*, vol. 282, pp. 484-487, 1998.

[81] E. T. Lagally, P. C. Simpson, and R. A. Mathies, "Monolithic integrated microfluidic DNA amplification and capillary electrophoresis analysis system," *Sensors and Actuators B-Chemical*, vol. 63, pp. 138-146, 2000.

[82] J.-C. Kaplan and M. Delpech, *Biologie moléculaire et médecine*. Paris: Flammarion, Médecine-Sciences, 1989.

[83] H. Tian, A. F. R. Hühmer, and J. P. Landers, "Evaluation of silica resins for direct and efficient extraction of DNA from complex biological matrices in a miniaturized format," *Analytical Biochemistry*, vol. 283, pp. 175-191, 2000.

[84] K. A. Wolfe, M. C. Breadmore, J. Ferrance, M. E. Power, J. F. Conroy, P. M. Norris, and J. P. Landers, "Toward a microchip-based solid phase extraction method for isolation of nucleic acids," *Electrophoresis*, vol. 23, pp. 727-733, 2002.

[85] L. Ceriotti, J. Lichtenberg, A. Dodge, N. F. De Rooij, and E. Verpoorte, "Combined nucleic acid extraction and enrichment in bead-packed plastic beds," presented at Micro Total Analysis Systems 2002, Kyoto, Japan, 2002.

[86] Y.-C. Lin, H.-C. Ho, C.-K. Tseng, and S.-Q. Hou, "A poly-methylmethacrylate electrophoresis microchip with sample preconentrator," *Journal of Micromechanics and Microengineering*, vol. 11, pp. 189–194, 2001.

[87] M. Stelze, M. Dürr, M. Cieplik, and W. Nisch, "On-chip electrophoretic accumulation of DNA oligomers and streptavidin," *Fresenius Journal of Analytical Chemistry*, vol. 371, pp. 112-119, 2001.

[88] L.-S. Jang, D. R. Meldrum, and M. Holl, "An active mixer for microscale purification and sequencing reaction clean-up," presented at Micro Total Analysis Systems 2002, Kyoto, Japan, 2002.

[89] R. C. Anderson, X. Su, G. J. Bogdan, and J. Fenton, "A miniature integrated device for automated multistep genetic assays," *Nucleic Acids Research*, vol. 28, pp. e60, 2000.

2 Experimentals and Device Layouts

2.1 Microchip Fabrication

The microfluidic devices were fabricated in 5-inch glass wafers (525 μm thick) at the IMT using standard photolithography process [1-4]. Figure shows two scanning electron microscopy (SEM) pictures of planar diverging and converging microchannel elements on a glass substrate.

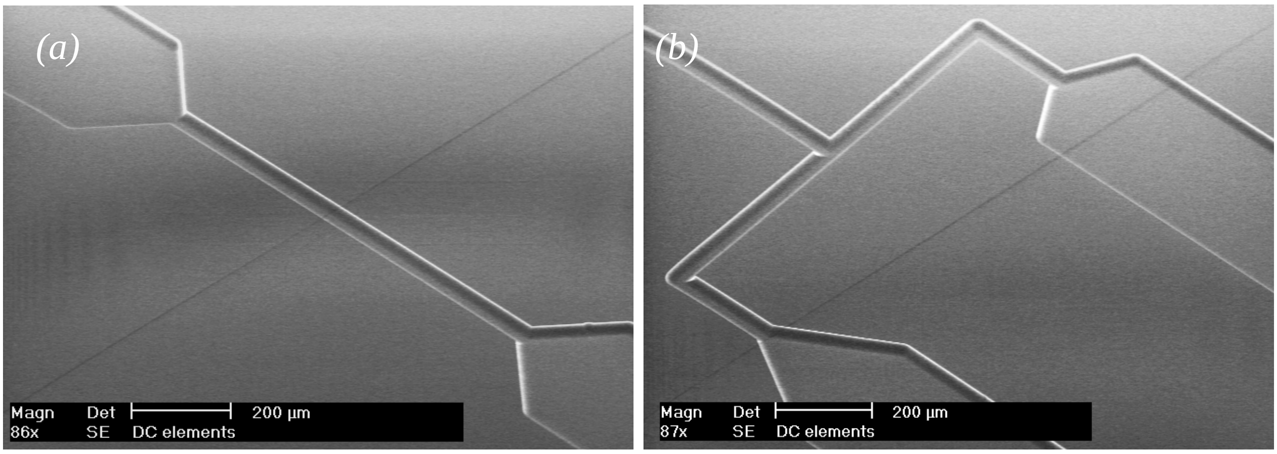

Figure 2.1
SEM pictures of micro diverging and converging elements (a) in series (b) in parallel.

The fabrication starts by a low-pressure chemical vapor-deposition (LPCVD) at 565° of a poly-silicon (400 nm) layer on both wafer sides. A positive photoresist (AZ 1518, Clariant GmbH, Wiesbaden, Switzerland) is then spin-coated on one side of the wafer. The wafer is aligned with respect to the mask in an optical lithographic step and the resist is exposed to UV light. The exposed resist is dissolved in a developer solution (AZ 351 developer: DI water, 1:4). After development, reactive-ion etching (RIE), a dry selective etching (photoresist ideally not etched) of exposed poly-silicon is performed to transfer the pattern obtained by photolithography to the poly-silicon layer. The dry etching is followed by a wet etching of the exposed glass with either 50 % hydrofluoric acid (50 % HF) or 20 % HF to transfer the pattern to the glass substrate. The glass is isotropically etched with a rate of about 9 µm/min in 50 % HF and a rate of 1.3 µm/min in 20 % HF. After removing the remaining poly-silicon layer using a 40 % KOH bath at 60°C for 10 min, the microstructured wafer is bonded to a coverplate with pre-drilled holes (Sensors Prep Services) using fusion bonding (650°C for 6 hours).

2.2 Experimental Set-up

A computer-controlled power supply system made in-house (HV 10kV Elstar Electronik, CH) with high-voltage relays (Reedrelais 14kV, Günther GmbH, CH) was used for voltage control. Figure 2.2 shows the apparatus used for chip operations. The chip was mounted onto an X-Y-Z translation stage. An argon-ion laser (488 nm, Ion Laser Technology, UT, USA) was used to achieve the detection of the labelled biotin by laser-induced fluorescence (LIF) made in-house [5]. The laser light was reflected by a dichroic filter (488 nm, ILEE, Urdorf, Switzerland) and focused in the channel by means of a microscope objective (25 X; N.A.= 0.35; Leica AG, Glattbrugg, Switzerland). The spot size is about 25 µm diameter. The fluorescence signal collected by the microscope objective, was passed through the dichroic filter and a 1 mm pinhole before being detected with a photomultiplier tube (PMT) (Hamamatsu Photonics K.K., Schüpfen, Switzerland). For visual inspection the PMT was replaced with a CCD camera (Digital ½ inch CCD, JVC).

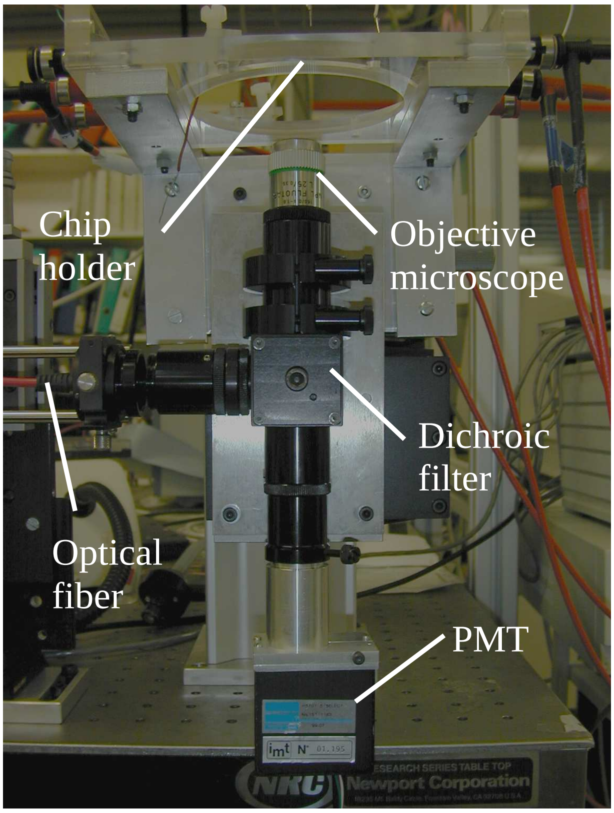

Figure 2.2
Picture of the set up for LIF.

2.3 Preparation of Reagents, Solutions and Samples

25 mM carbonate (pH 9) buffer and 10 mM sodium tetraborate buffer (pH 9) were made from anhydrous sodium carbonate and sodium hydrogen carbonate powders (Merck AG, Dietikon, Switzerland) and borate (Fluka Chemicals, Buchs, Switzerland), respectively, and DI water. 1 M filtered HPCE grade NaOH, used for microchannel conditioning, was obtained from Fluka. Fluorescein-labeled biotin (FLB and B4F, λ_{ex} = 490 nM, λ_{em} = 520 nM), obtained from Molecular Probes, was diluted in sodium tetraborate buffer. All previously unfiltered solutions were filtered with 0.2-µm aqueous filters (Semadeni, Ostermundingen, Switzerland) before being introduced into the chip.

Polystyrene beads ranging from 0.5 µm to 6 µm were from Polysciences (Germany), except the 2.5-µm Alignflow beads (Molecular Probes). Before use, the original bead buffer (100 µL) is replaced by 10 mM sodium tetraborate buffer by centrifugation (3x 1 min at 1500 rpm at 4°C). Beads are vortexed and sonicated in an ultrasonic bath (1 min) prior to use.

The purified 48-kbp double-stranded λ DNA was from Invitrogen (Basel, Switzerland). An aliquot of the initial 500 µg/mL λ DNA sample was diluted to 2 µg/mL and 1 µg/mL in 10 mM sodium tetraborate buffer (pH = 9) containing 1 mM EDTA (Fluka) prior to use. The λ DNA was stained with YOYO 1 (Molecular Probes, λ_{ex} = 491 nm, λ_{em} = 509 nm)

2.4 Device Layout

Two types of layouts have been used to investigate the consequences of opposing EOF to PF in microfluidic devices: microchannels with uniform cross-section and microchannels featuring diverging and converging elements.

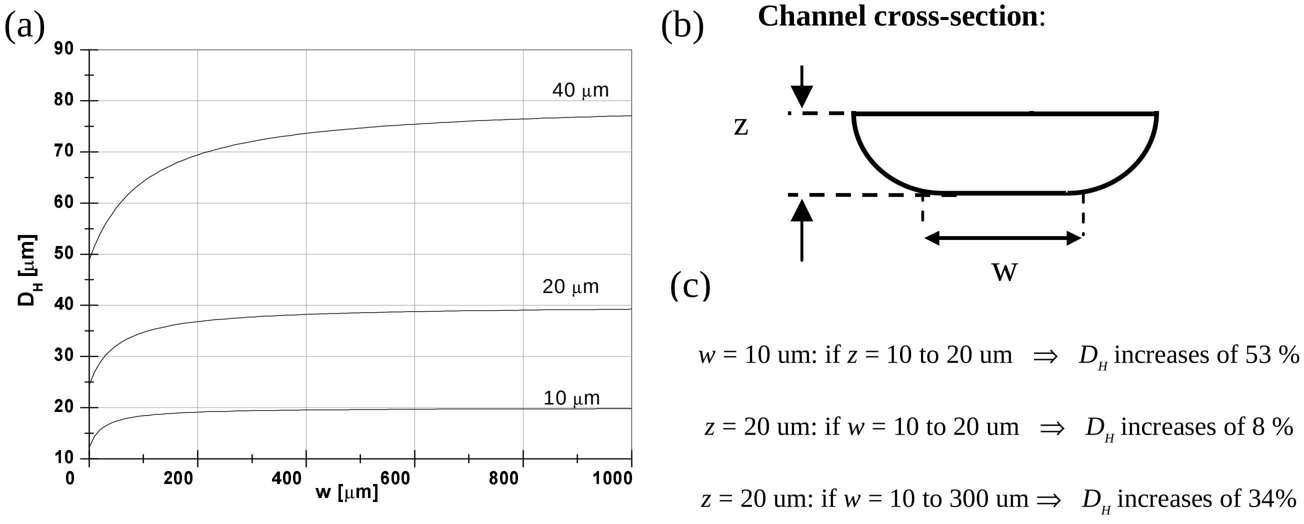

w = 10 um: if *z* = 10 to 20 um ⇒ D_H increases of 53 %

z = 20 um: if *w* = 10 to 20 um ⇒ D_H increases of 8 %

z = 20 um: if *w* = 10 to 300 um ⇒ D_H increases of 34%

Figure 2.2

(a) Hydraulic diameter versus mask line width (w) for two channel depths z. (b) Sketch of the 90°-rotated-D-shaped cross-section. (c) Examples of the evolution of D_H when channel depth or mask line width increase.

The microfluidic devices were etched in Pyrex 7740 glass wafers or borosilicate glass wafers. These devices are characterized by their channel length, L, and their hydraulic diameter, D_H. The D_H for 90°-rotated-D-shaped cross-sections, produced by isotropic etching of Pyrex with hydrofluoric acid, is given by 4 x (channel area (A) /wetted perimeter, (P)):

$$D_H = 4\left(\frac{A}{\mathrm{P}}\right) = 4\left(\frac{wz + \frac{\pi z^2}{2}}{2(w+z)+\pi z}\right) \qquad \textbf{Eq 2.1}$$

where w is the width of the channels on the mask [μm] and z the channel depth [μm]. The D_H will often be used in this work. Figure 2.2 illustrates the behaviour of D_H as a function of w for z = 10 μm and 20 μm. The larger w for a given channel depth, the larger D_H becomes. For instance, D_H increases about 50% when w goes from 10 μm to 300 μm.

2.4.1 Microchannels with Uniform Cross-Section

Figure 2.3 illustrates the layouts of the devices used in this work, with dimensions and device name presented in Table 2.1. The applied potentials, V, the difference in reservoir height, Δh, between the reservoirs 1 (R_1) and R_3, and the buffer concentrations indicated in Figure 2.3 correspond to the experimental parameters used in Chapter 3 and Chapter 4. The direction of the EOF and PF are also indicated.

Device G8 is a microchannel with a serpentine structure featuring 15 right-angle corners (same channel cross-section, 1.5 mm between corners). G2, G3 and G4 have the same layout, four reservoirs and a double-T intersection (200 μm long), but with different lengths L. G7 is a straight microchannel with only one inlet and one outlet. The length L of the straight microchannels ranges from 3.3 cm to 8 cm while the microchannel depth ranges from 20 μm to 27 μm. The channel depths were measured in the cleanroom with a surface profilometer (alpha-step, Tencor, CA) before the prebonding step.

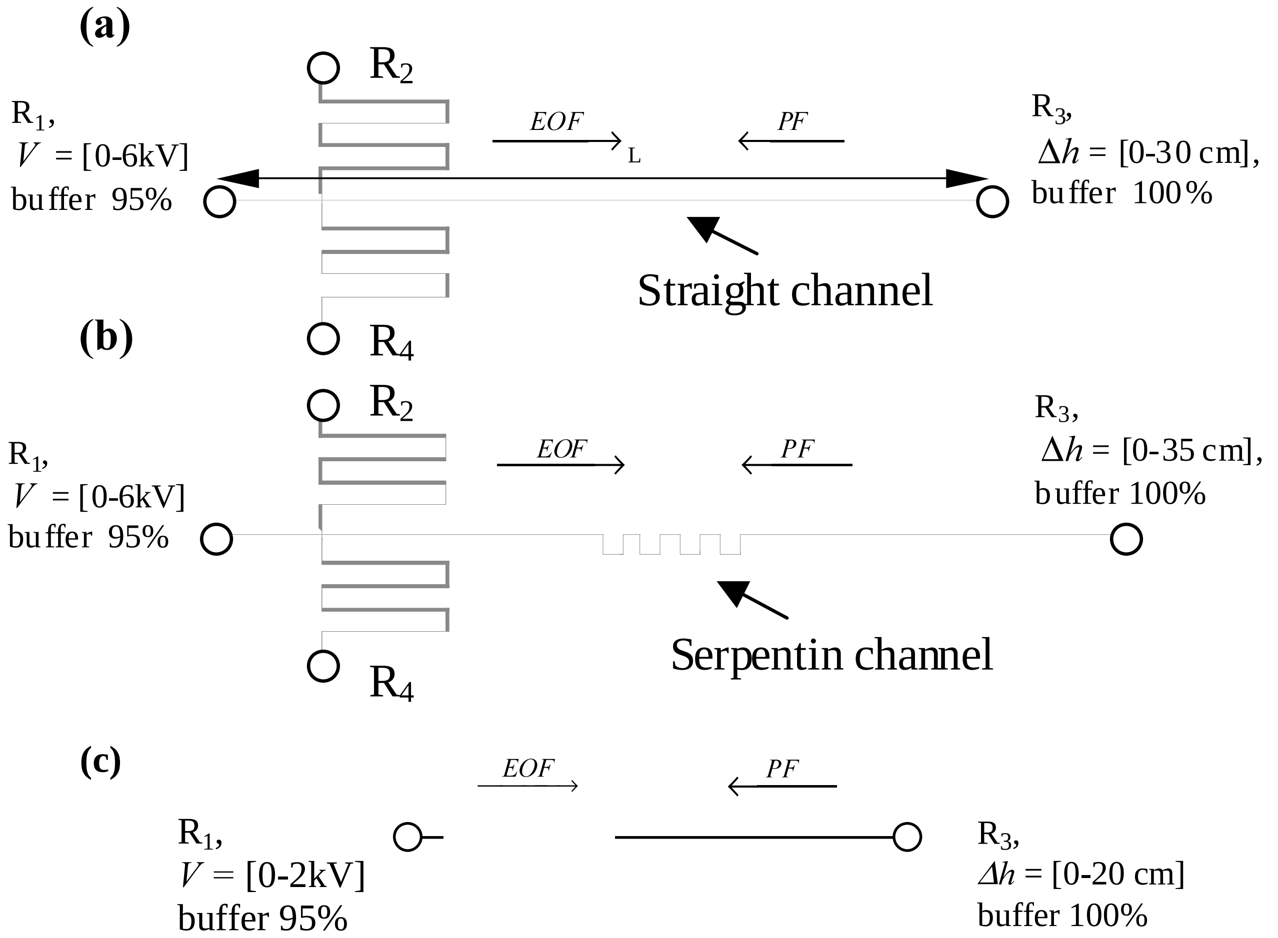

Figure 2.3
Layout of microfluidic devices used for the study of the bi-directional flow in Chapter 3 and Chapter 4. (a) G2,G3 and G4 (b) G8 (c) G7

Device name	**G2**	**G3**	**G4**	**G7**	**G8**
w [μm]	10	10	10	14	10
z [μm]	22	20	20	27	22
D_H [μm]	30	27	27	37	30
L [cm]	6	5	8	3.3	8
D_H^2/L [μm]	0.015	0.02	0.013	0.04	0.011

Table 2.1
Geometric parameters for five straight microchannels of constant cross-section area.

2.4.2 Microchannels with Diverging and Converging Elements (1)

The microfluidic devices used to investigate the generation of controlled, steady recirculating flows consist of planar diverging and converging elements. These elements are incorporated into the network by including two wider segments along the longer channel. These microfluidic devices are used in Chapter 3 and Chapter 4. “Diverging channel” refers to a channel segment of expanding cross-section, whereas “converging channel” refers to a contracting cross-section. These elements are defined in this work in terms of the direction of the pressure-driven flow. The first channel expansion encountered by PF is then defined as the 1st diverging microchannel element and so on.

Figure 2.4 shows the three layouts used to study the effect of the EOF and the PF on the flow rate in Chapter 3. Figure (c) shows an expanded view of the diverging and converging elements where recirculating flows are produced.

The devices shown in Figure 2.4 are divided in i = 5 segments of length $L_i = L_1, \ldots L_5$. The segments i = 1, 3 and 5 are narrow microchannels of uniform cross-section. These segments were generally 50 to 70 μm wide across the top, for depth of 20 to 30 μm, respectively. The other two segments are wider and are connected to the narrow microchannels through converging and diverging elements. Diverging and converging channel elements are characterised by opening angles θ_{div} and θ_{con}, respectively. The ratios between the cross-sections are A_2/A_1 and A_4/A_1, where A_1 is the cross-sectional area of the segments L_1, L_3 and L_5 and A_2 and A_4 correspond to cross-sectional areas of the wide channel elements with length L_2 and L_4. The dimensions of the three devices are summarized in Table 2.2. The width of the wide channels (that is, A_2 and A_4) never exceeds 400 μm and $A_2 \geq A_4$. The lengths L_2 and L_4 of the segments of cross-sectional area A_2 and A_4, respectively, are equal to the length of the narrow channel L_3 . In the devices of Figure 2.4, for i = 2, 3, 4, L_i = 3000 μm.

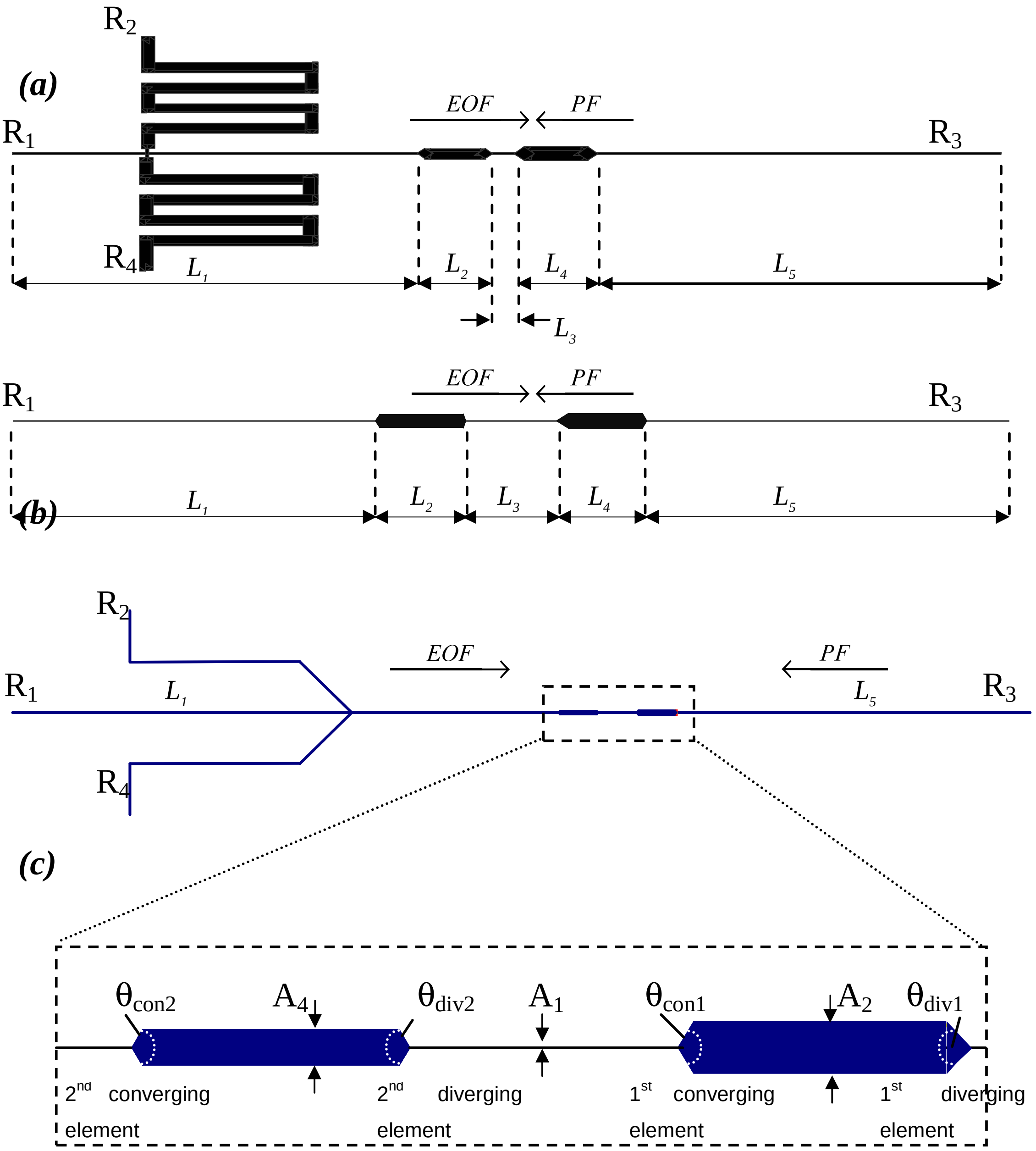

Figure 2.4

The three microfluidic device layouts with gradual channel expansion (divergent channel) and contraction (convergent channel) elements inserted into the fluid stream. These elements change the local streamwise area. (a) DC3 (b) DC1 and (c) DC2. Blow up: details of the diverging and converging elements where flow division and separation, respectively, are observed (Chapter 3). $A_2/A_1 \cong 6$, $A_4/A_1 \cong 5$, $L_2 = L_3 = L_4 = 3000\ \mu m$.

The devices called DC1, DC2 and DC3 were used to investigate the recirculating flows. However, other microfluidic devices were used, in addition to those shown in

Figure 2.4. Their layouts are almost identical as DC1, DC2 and DC3. In general, only the opening angles are varied between 60° to 270° while the ratios $A_{2,4}/A_1$ and the lengths $L_{i=2,3,4}$ are kept constant. The purpose of the side channels of DC2 and DC3 is introduced in the next section, and was specific to the applications developed in Chapter 5.

Device's name	z [μm]	L_1 [μm]	$L_{2,3,4}$ [μm]	L_5 [μm]	$A_{1,3,5}$ [m^2]	A_2 [m^2]	A_4 [m^2]
DC3	33	25500	3000	25500	2 x 10^{-9}	1.2 x 10^{-8}	8.6 x 10^{-9}
DC2	18	27100	3000	41900	8 x 10^{-10}	4.6 x 10^{-9}	6.3 x 10^{-9}
DC1	27	12000	3000	12000	1.48 x 10^{-9}	9.1 x 10^{-9}	7.8 x 10^{-9}

Device's name	θ_{div1} [°]*	θ_{con1} [°]*	θ_{div2} [°]*	θ_{con2} [°]*	α^{-1} [μm]
DC3	90	90	90	90	2.5 x 10^{-8}
DC2	90	120	120	120	6.8 x 10^{-9}
DC1	120	90	60	90	2.86 x 10^{-8}

* *The opening angles are not fixed values*

Table 2.2
Names and geometric parameters of the microfluidic devices used in Chapter 3 and Chapter 4. The definition of α can be found in section 3.2 of Chapter 3.

2.4.3 Microchannels with Diverging and Converging Elements (2)

The microfluidic devices SB1, SB2, SB3 and DNA1 used in Chapter 5 and Chapter 6 for bead-based assay and DNA and sample preconcentrations have a similar layout as those introduced in the previous section. They feature two diverging and converging elements. For these applications, the side microchannels are used for loading samples, reagents or beads. The layouts of these microfluidic devices are shown in Figure 2.5 and Figure 2.6. The layout of SB2 was not included in Figure 2.5 since it has the same layout as DC2 except that the length L_3 = 4000 μm. The dimensions of these microfluidic devices are given in Table 2.3.

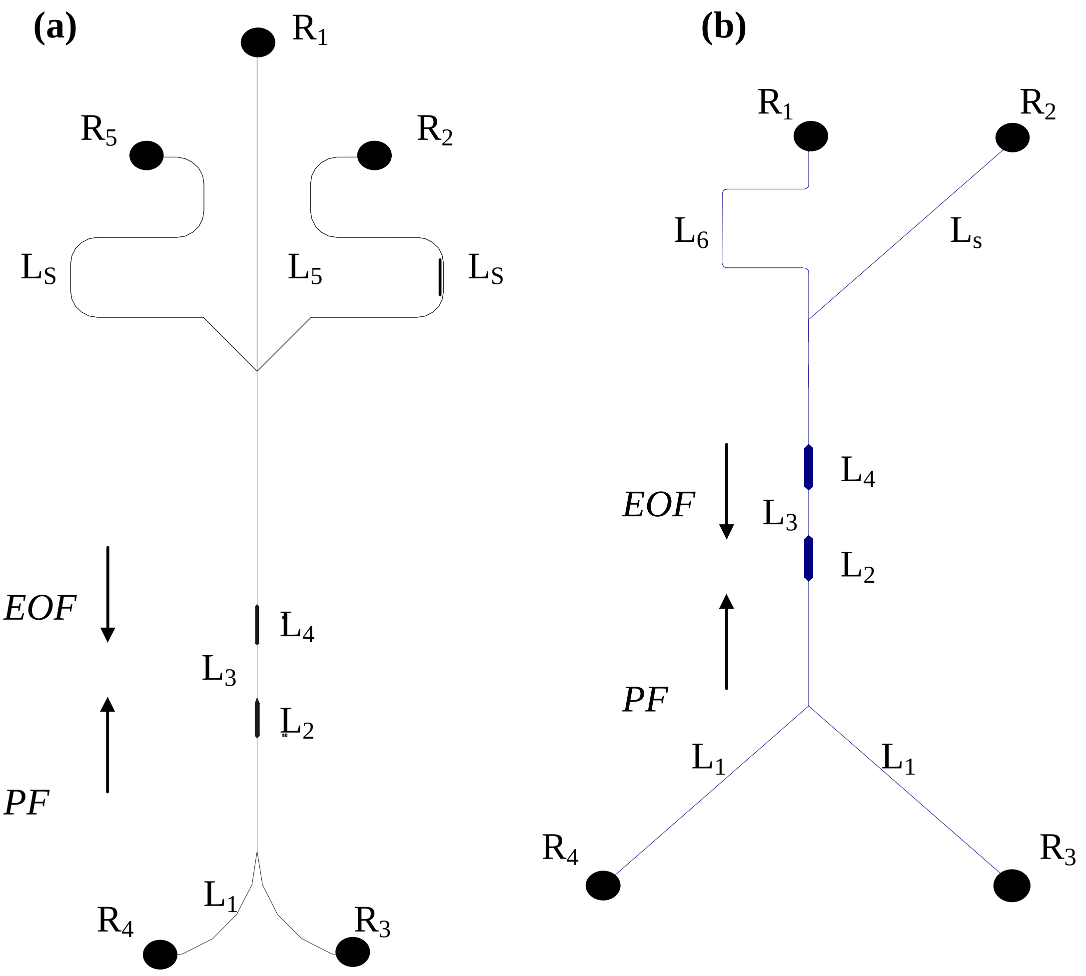

Figure 2.5
Layouts of SB3 (a) and SB1 (b). The layout of SB2 is the same as DC2 except that $L_3 = 4000\ \mu m$.

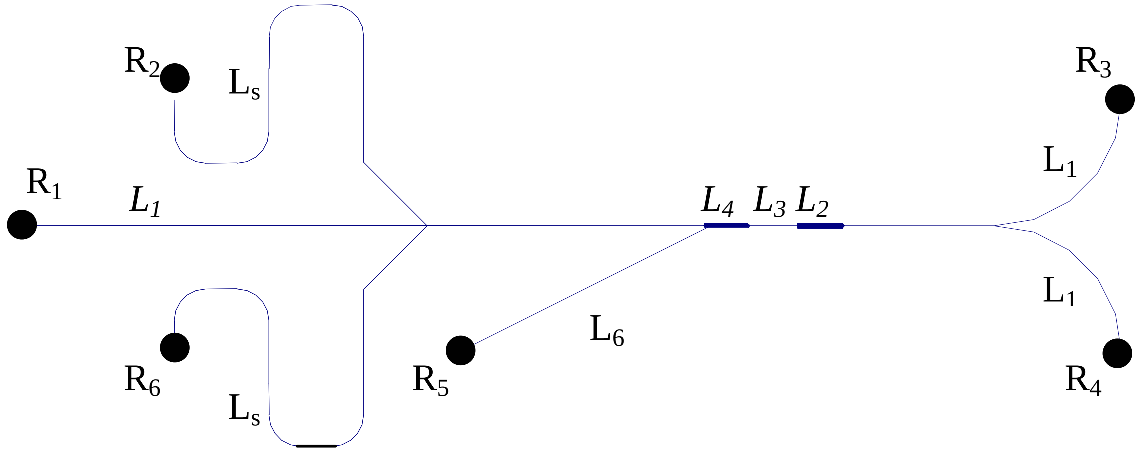

Figure 2.6
Layout of the microfluidic device used forλ-DNA preconcentration in Chapter 6. An additional side channel of length L_6 was added to the system to load the sample.

Device's name	***z* [μm]**	**L_1 [μm]**	**$L_{2,4}$ [μm]**	**L_3 [μm]**	**L_5 [μm]**	**L_6 [μm]**	**L_s [μm]**
SB3	20	22100	3000	4000	40000	-	37800
SB2	20	27100	3000	4000	41900	-	22700
SB1	23	16000	3000	3000	5500	14000	10500
DNA1	23	22100	3000	3000	40000	17600	37800

Device's name	θ_{div1} **[°]***	θ_{con1} **[°]***	θ_{div2} **[°]***	θ_{con2} **[°]***	**$A_{1,3,5,6,s}$ [m^2]**	**A_2 [m^2]**	**A_4 [m^2]**
SB3	90	60	120	90	9.1×10^{-10}	7×10^{-9}	5.1×10^{-9}
SB2	90	120	120	120	9.1×10^{-10}	7×10^{-9}	5.1×10^{-9}
SB1	90	90	90	90	1.15×10^{-9}	9.1×10^{-9}	7.8×10^{-9}
DNA1	90	180	120	90	1.15×10^{-9}	8.2×10^{-9}	6×10^{-9}

* *The opening angles are not fixed values*

Table 2.3
Names and geometric parameters of the microfluidic devices used in Chapter 5 and Chapter 6.

2.5 References

[1] S. M. Sze, Semiconductor Devices. Physics and Technology, 1 ed: *John Wiley & Sons*, 1985.

[2] M. Madou, Fundamentals of microfabrication, first ed. Boca Raton, Florida: CRC Press, 1997.

[3] A. Dodge, K. Fluri, E. Verpoorte, and N. F. de Rooij, "Electrokinetically driven microfluidic chips with surface modified chambers for heterogeneous immunoassays," *Analytical Chemistry*, vol. 73, pp. 3400-3409, 2001.

[4] J. Lichtenberg, E. Verpoorte, and N. F. de Rooij, "Sample preconcentration by field amplification stacking for microchip-based capillary electrophoresis," *Electrophoresis*, vol. 22, pp. 258-271, 2001.

[5] G. Ocvirk, T. Tang, and D. J. Harrison, "Optimization of confocal epifluorescence microscopy for microchip-based miniaturized total analysis systems," *Analyst*, vol. 123, pp. 1429-1434, 1998.

3 On-Chip Recirculating Flows Analysis

3.1 Introduction

Flow separation and reattachment in macroscopic pipe systems is a widely studied phenomenon because of its importance in many engineering applications. When flow separation occurs, minor losses have to be included into the models for the flow rate calculation. Flow separation in macroscopic systems occur at relatively large Reynolds number (~2300), whereas this is not the case in microfluidic systems [1]. As introduced in Chapter 1, only a few studies report flow separation in microfluidic systems at low Reynolds number (<1). In some of these reports, flow separation occurred in the microscale [2]. In the case of [3, 4], gas flow separation at an orifice-like constriction could unfortunately not be observed, although their reported data suggested this. It was assumed in these studies that a micro vortex of gas flow, on the order of 10 μm in size, can develop downstream and upstream of the constriction. In this chapter, the formation of controlled, fully developed and steady recirculating flows at diverging and converging microchannels elements, at $Re < 0.02$, is experimentally and numerically reported.

To demonstrate that these recirculating flows take place, it is first demonstrated that a mismatch exists between theory and experiment if minor losses are not taken into account (section 3.3). Section 3.2 introduces a model, based on [5-7], to calculate the average flow rates under conditions where a bi-directional flow is present in a microfluidic device with uniform cross-section. In the same section, the model is extended to microfluidic devices featuring diverging and converging elements assuming that no minor losses are induced for Re < 0.1. Section 3.3 compares the theoretical model and the experimental results for microchannels with both uniform and non-uniform cross-sections using the current monitoring method. In the same section, a method using beads for flow visualisation is introduced in order to have detailed information on the flow pattern when a bi-directional flow is generated under the effect of EOF and PF. This method is also used to investigate the flow pattern when a bi-directional flow is present in microfluidic devices featuring diverging and converging elements.

In section 3.4, a theoretical model taking into account the minor losses for the calculation of flow rate is introduced. The originality of this model is that the value corresponding to the conventional loss coefficient is a function of the PF, the EOF and the geometry of the microfluidic device. It is also shown that recirculating flows can be predicted for a particular geometry.

This chapter ends with some examples of recirculating flow control using beads, illustrating the potential benefits of handling beads with fluid flows only.

3.2 Model for Bi-directional Flow in Microfluidic Systems

3.2.1 Steady-Flow Energy Equation for Pressure-driven Flows in Microchannels

To relate the pressure to the velocity of a fluid in a microchannel, taking into account the geometry of the device, Eq 1.8, the steady-flow energy equation for low flow rates in a microchannel with one inlet and one outlet, can be used [8]. Since microfluidic devices are planar, there is no height difference along the microchannel and $Z_{in} = Z_{out}$. Eq 1.8 then becomes:

$$\left(\frac{p}{\rho g}+\frac{u^2}{2g}\right)_{in}=\left(\frac{p}{\rho g}+\frac{u^2}{2g}\right)_{out}+\Delta h_{tot} \qquad \textbf{Eq 3.1}$$

For microchannels composed of different segments *i* with different cross-sections, the Δh_{tot} is given by the sum of frictional losses and minor losses across the system:

$$\Delta h_{tot}=\sum_i (h_{fi}+h_{mi})=\sum_i \frac{u_{p_i}^2}{2g}\left(\frac{f_i L_i}{D_{Hi}}+K_i\right) \qquad \textbf{Eq 3.2}$$

where h_f is the head loss that results from the wall shear in a developed flow, h_m the minor loss due to the fitting of the flow to non-uniform cross-sections, u_p the average pressure-induced linear velocity[*], f the fanning friction factor, L the channel length and D_H the hydraulic diameter (see Chapter 2). K is the loss coefficient corresponding to the minor loss [8, 9].

Liquids propelled by a pressure-driven flow in a microfluidic device usually have flow rates which are of the order of nL/s; hence their Reynold's number are very low ($Re < 1$, regime of creeping flow). Under this condition, independent of the geometry of the microchannel, the flow is laminar and no minor losses are expected. Therefore h_m can be neglected ($K = 0$) and Eq 3.2 reduces to:

$$\Delta h_{tot}=\sum_i h_{fi}=\sum_i \frac{u_{p_i}^2}{2g}\frac{f_i L_i}{D_{Hi}} \qquad \textbf{Eq 3.3}$$

The total head loss is proportional to the square of the velocity and to the ratio of the length and to hydraulic diameter.

---

[*] We assumed that the length of the divergent and convergent elements are negligible compared to the length of the microchannel segments.

3.2.2 Consequences of Opposing EOF and PF in Microchannels

Electro-osmotic flow (EOF) is a bulk flow of fluid which results when motion, generated in the diffuse double-layer at microchannel walls through application of an axial electric field, is transferred to adjacent fluid layers by viscous forces. Theory states that the plug profile of EOF and the parabolic profile of Poiseuille flow are independent of each other and can be combined to give rise to bi-directional flow when the overall net volume flow approaches zero [5]. Thus, whenever electro-osmosis and pressure-driven counter flow co-exist in etched glass capillaries, the average velocity can be expressed as the sum of the average electrokinetic linear velocity, u_{ek}, and the average pressure-induced linear velocity, u_p:

$$u_{ave} = \sum_i (u_{ek_i} - u_{p_i}) = \sum_i ((\mu_{EOF} E_i - u_{p_i}) \qquad \textbf{Eq 3.4}$$

where μ_{EOF} is the electroosmotic mobility ([cm^2/Vs]), and E the electric field obtained by applying a potential V over a channel of length L.

When a bi-directional flow is present in a straight microchannel of uniform cross-section, two well-defined regions of laminar flow are generated in opposite directions as the average velocity, u_{ave}, approaches 0. In the core of the microchannel, PF is dominant. Close to channel walls, EOF is dominant and determines the direction of flow. The left sketch of Figure 3.1 shows the velocity flow profiles induced by EOF and PF. The sketch at the bottom of the figure gives an idea of the velocity flow profile obtained when a bi-directional flow is fully developed in a straight microchannel [5-7].

In this work, two types of microfluidic devices are considered: a) microchannels with uniform cross-section b) devices with 2 diverging and 2 converging elements inserted into the fluid stream. All the geometrical parameters as well as the names of these devices are reported in Chapter 2.

The theory of bi-directional flow in microfluidic channels with constant cross-section, as shown in Figure 3.1, will be discussed in the next section. Section 3.2.2.2 will deal with the theory concerning microchannels with diverging and converging elements.

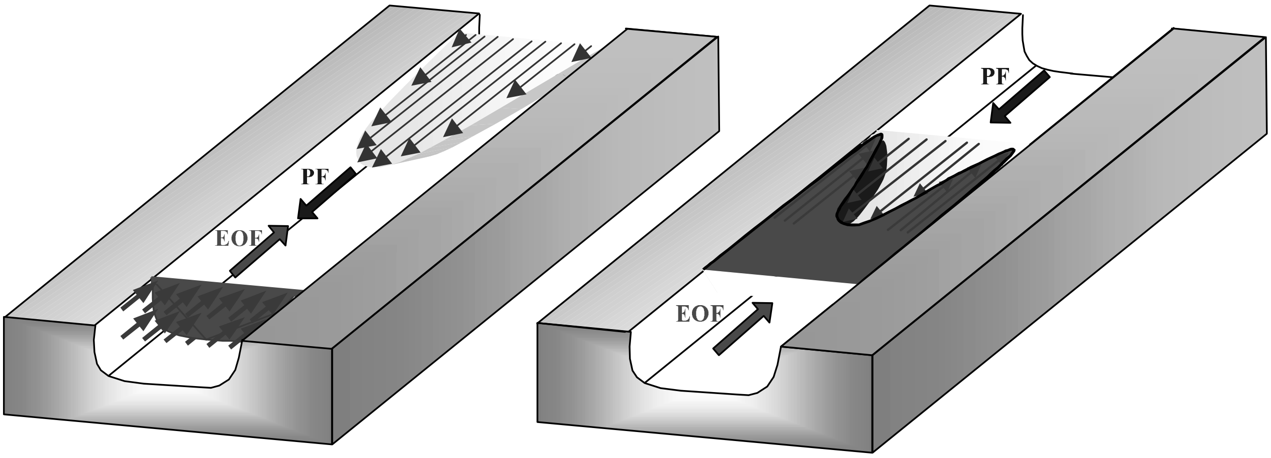

Figure 3.1
Schematic of a microchannel showing the velocity profiles of electro-osmotic flow and pressure-driven flow (top) The velocity flow profile of EOF is ideally flat in contrast with the parabolic velocity flow profile induced by pressure. Velocity vectors are additive and can be combined to give rise to a bi-directional flow (bottom).

3.2.2.1 Viscous FlowAnalysis for Microchannels with Uniform Cross-section

The pressure drop across a planar microchannel of constant cross-section can be calculated using Eq 3.1 and Eq 3.3. For a microchannel of uniform cross-section (i=1), Eq 3.1 becomes:

$$\frac{p_1 - p_2}{\rho g} = \frac{\Delta p}{\rho g} = \frac{u_p^2}{2g}\,\frac{fL}{D_H} = h_f \qquad \textbf{Eq 3.5}$$

To calculate the head loss, h_f, the fanning friction factor, f, needs to be known. For laminar flow, $f = 64/Re_{D_H}$ where $Re_{D_H} = u_p D_H \rho/\eta$ (see Chapter 1). The hydraulic diameter D_H for 90°-rotated-D-shaped cross-sections, produced by isotropic etching of Pyrex with hydrofluoric acid, is given by Eq 2.1 (see Chapter 2). By substituting f and Re_{D_H} in Eq 3.5, the head loss becomes:

$$h_f = \frac{32\eta}{\rho g}\frac{L}{D_H^2}u_p \qquad \textbf{Eq 3.6}$$

Thus, the channel-head loss is proportional to the average velocity, the length of the channel L, and inversely proportional to the square of the hydraulic diameter. Knowing that velocities induced by pressure and electro-osmosis are additive and using Eq 3.4 and Eq 3.6, the average velocity is given by:

$$u_{ave} = \mu_{EOF}\frac{V}{L} - \frac{1}{32\eta}\frac{D_H^2}{L}\Delta p \qquad \textbf{Eq 3.7}$$

Theory predicts that in a microchannel of uniform cross-section, when EOF and PF coexist in opposite directions, the average velocity decreases linearly as a function of the pressure. u_{ave} strongly depends on the hydraulic diameter. For wide and deep microchannels, this effect is more significant than for shallow and narrow microchannels.

3.2.2.2 Microchannel Device with Diverging and Converging Elements

The continuity equation dictates that the flow rate is the same in all the segments i of the microchannels shown in Figure 2.5 (Chapter 2):

$$Q_1 = Q_2 = Q_3 = Q_4 = Q_5 = const. \qquad \textbf{Eq 3.8}$$

Eq 3.8 can be rewritten, using the flow rate $Q_i = u_{pi}A_i$:

$$u_{p1}A_1 = u_{p2}A_2 = u_{p3}A_3 = u_{p4}A_4 = u_{p5}A_5 \qquad \textbf{Eq 3.9}$$

where A_i is the cross-sectional area of microchannel segment i and u_{pi} is the average pressure-induced velocity in this element. Hence, $A_1 = A_3 = A_5$ implies that $u_{p1} = u_{p3} = u_{p5}$. Eq 3.9 can be used to express u_{p2} and u_{p4} as a function of u_{p1}:

$$u_{p2} = \frac{A_1}{A_2} u_{p1} \text{ and } u_{p4} = \frac{A_1}{A_4} u_{p1} \qquad \textbf{Eq 3.10}$$

Eq 3.2 and 3.4 can be used to find an expression for the average velocity when a bi-directional flow is present in a microfluidic device with divergent and convergent channel elements. The total head loss of the system is equal to the sum of the head loss in each microchannel segment. Assuming that, in the absence of counter EOF, the fluid stream does not separate from the walls at the divergent and the convergent elements and, consequently, that minor losses are equal to zero, the total head loss is given by:

$$\Delta h_{tot} = \sum_{i=1}^{5} h_{fi} = \sum_{i=1}^{5} \frac{u_{pi}^2}{2g} \frac{f_i L_i}{D_{Hi}}$$

$$= \frac{u_{p1}^2}{2g} \frac{f_1 L_1}{D_{H1}} + \frac{u_{p2}^2}{2g} \frac{f_2 L_2}{D_{H2}} + \frac{u_{p3}^2}{2g} \frac{f_3 L_3}{D_{H3}} + \frac{u_{p4}^2}{2g} \frac{f_4 L_4}{D_{H4}} + \frac{u_{p5}^2}{2g} \frac{f_5 L_5}{D_{H5}} \qquad \textbf{Eq 3.11}$$

As stated in section 3.2.2.1, f_i can be expressed as a function of u_p using the Reynolds number

$$f_i = \frac{1}{u_{pi}} \frac{64\eta}{\rho D_{Hi}} \qquad \textbf{Eq 3.12}$$

Using Eq 3.12 and assuming $D_{H1} = D_{H3} = D_{H5}$, Eq 3.11 can be developed to give:

$$\Delta h_{tot} = \frac{32\eta}{\rho g} \left(\frac{L_1 + L_3 + L_5}{D_{H1}^2} + \frac{A_2}{A_1} \frac{L_2}{D_{H2}^2} + \frac{A_4}{A_1} \frac{L_4}{D_{H4}^2} \right) u_{p1}$$

or $$\Delta h_{tot} = \frac{32\eta\alpha}{\rho g} u_{p1} \qquad \textbf{Eq 3.13}$$

with $$\alpha = \frac{L_1 + L_3 + L_5}{D_{H1}^2} + \frac{A_2}{A_1} \frac{L_2}{D_{H2}^2} + \frac{A_4}{A_1} \frac{L_4}{D_{H4}^2} \qquad \textbf{Eq 3.14}$$

The value of α [μm^{-1}] depends on the geometry of the device. Combining Eq 3.13, Eq 3.14 and Eq 3.4, the average linear velocity is given by:

$$u_{ave} = \mu_{EOF} E - \frac{1}{32\eta}\frac{1}{\alpha}\Delta p \qquad \textbf{Eq 3.15}$$

The average velocity in a microfluidic device incorporating elements of varying cross-sections is of the same form as for a channel of constant cross-section when EOF is opposed to PF (e.g. in Eq 3.7). The difference is that D_H^2/L is replaced by the coefficient α. It is important here to stress that Eq 3.15 gives an estimate of the average velocity of the flow when no minor losses are generated.

From an analytical point of view, Eq 3.7 and Eq 3.15 provide qualitative information about the average linear velocity as a function of the hydrostatic pressure and the EOF. From a practical point of view, these equations are useful for standard microfluidic operation systems where EOF (or CZE) is involved and small hydrostatic pressure effects (< 0.5 Pa) have to be avoided or need to be estimated (for design improvements for example). The next sections will discuss the accuracy of Eq 3.7 and Eq 3.15. Experimental results validating Eq 3.7 are introduced. It will be shown that Eq 3.15 ceases to be accurate especially when counter PF becomes significant (> 1 Pa) for microchannels with non-uniform cross-sections.

3.3 Results and Discussion

In the previous section, it was shown that opposing EOF to PF can lead to a bi-directional flow. Two methods will be introduced that allow this effect to be studied. The first is based on the current monitoring method discussed in section 3.3.1 The second, introduced in section 3.3.2, is based on flow visualization with beads.

3.3.1 Current Monitoring Method

To validate Eq 3.7 and Eq 3.15, the effect of EOF and PF on u_{ave} was determined for:

1) straight narrow microchannels etched in Pyrex 7740 glass wafers or borosilicate glass wafers.

2) microchannels with a serpentine layout.

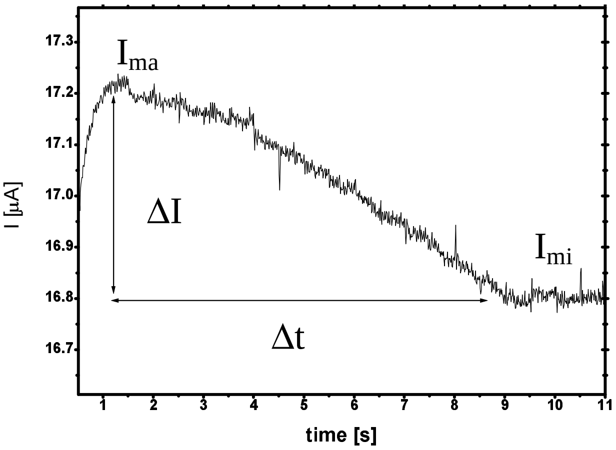

Figure 3.2
Measured current versus time when 9.5 mM sodium tetraborate buffer replaces 10 mM sodium tetraborate buffer at E = 760 V/cm. The current decreases by about 2%.

The names, layouts and dimensions of these devices are described in Chapter 2. A pressure head ranging from 0 to 35 cm (0 to 3.5 kPa) of buffer was typically applied on reservoir 3 (R_3), and a potential ranging from 0 to 6 kV between R_1 and R_3. Current monitoring was used to measure the average velocity when EOF and PF are opposed, due to its simplicity compared with other methods. These include methods based on the periodic photobleaching of a neutral fluorophore or on weighing the mass of the transferred electrolyte [10, 11], both of which are more difficult to perform from an instrumental point of view. Current monitoring, originally developed for use in capillaries [12], consists of measuring the current versus time when a buffer of lower concentration (95%) replaces a buffer (100%) in the channel. As the buffer of lower concentration progresses inside the microchannel driven by EOF, the current decreases linearly as function of time. The current drop continues until the entire microchannel is filled with buffer of lower concentration, at which point the current stabilizes again. Flow measurements made with the current monitoring method are common for quantitative studies of EOF in microfluidic devices [13-15]. However, this method proved only to be accurate for measuring the μ_{EOF} when the difference between buffer concentrations does not exceed 5%. Several studies demonstrated that the use of buffers having concentrations differing more than 5% creates a discontinuous buffer system, leading to misleading μ_{EOF} measurements [16-20].

The graphic of Figure 3.2 illustrates the evolution of the current as a function of time for a 9.5 mM sodium tetraborate (pH 9) buffer replacing a 10 mM sodium tetraborate buffer (pH 9) in a 3.3-cm-long straight channel with a uniform cross-section. The electroosmotic velocity, $u_{EOF,}$ is given by $L/\Delta t$, where L is the length of the microchannel and Δt the time necessary for the buffer of lower concentration to travel from the inlet to the outlet. This time corresponds to the time that is required to go from a maximum current I_{max} (100% buffer) to a minimum current I_{min} (95% buffer).

In the present experiments, the 100% concentrated buffer is used to provide the hydrostatic pressure to the system, while the diluted buffer is introduced within the microchannel by electroosmotic pumping. A hydrostatic pressure is obtained by applying a column of buffer at the microchannel inlet. Two buffer systems have been used in these experiments. The first is the sodium tetraborate buffer (10 mM at 100%, pH 9). The second is a carbonate buffer (30 mM at 100%, pH 9). The electro-osmotic mobility, μ_{EOF}, can be calculated from Figure 3.2 by

$$\mu_{EOF} = \frac{u_{EOF}}{E} = \frac{L^2}{V\Delta t} \qquad \textbf{Eq 3.16}$$

The μ_{EOF} was measured using the current monitoring method each time a new experiment was performed with one of the devices shown in Chapter 2. It was observed that the μ_{EOF} for the the two buffers used was:

- 10 mM sodium tetraborate buffer (pH 9): $\mu_{EOF} = 5.7 \pm 0.3\ cm^2/Vs$
- 30 mM carbonate buffer (pH 9): $\mu_{EOF} = 4.2 \pm 0.3\ cm^2/Vs$

3.3.1.1 Results for microchannels of constant cross-sections

The average linear velocity was measured as a function of the hydrostatic pressure at different electrical field strengths. The data in Figure 3.3 *(a)* were obtained for G7, at E = 150 V/cm, 300 V/cm and 600 V/cm. G7 consisted of a simple microchannel 3.3 cm long. Results obtained with three straight channels of uniform cross-section, but with different hydraulic diameters and lengths are shown in Figure 3.3 *(b)*. The dimensions of the device are summarized in Table 2.1 of Chapter 2. The solid curves represent the theoretical velocity as calculated with Eq 3.7.

As Figure 3.3 shows, the measured average velocity, u_{mea}, decreases linearly with the Δp, which is in agreement with Eq 3.7. The theoretical curves calculated from Eq 3.7 have also been included in the figure (solid lines). Since the average velocity is only due to the EOF at Δp = 0, the y-intercept varies as a function of applied potential.

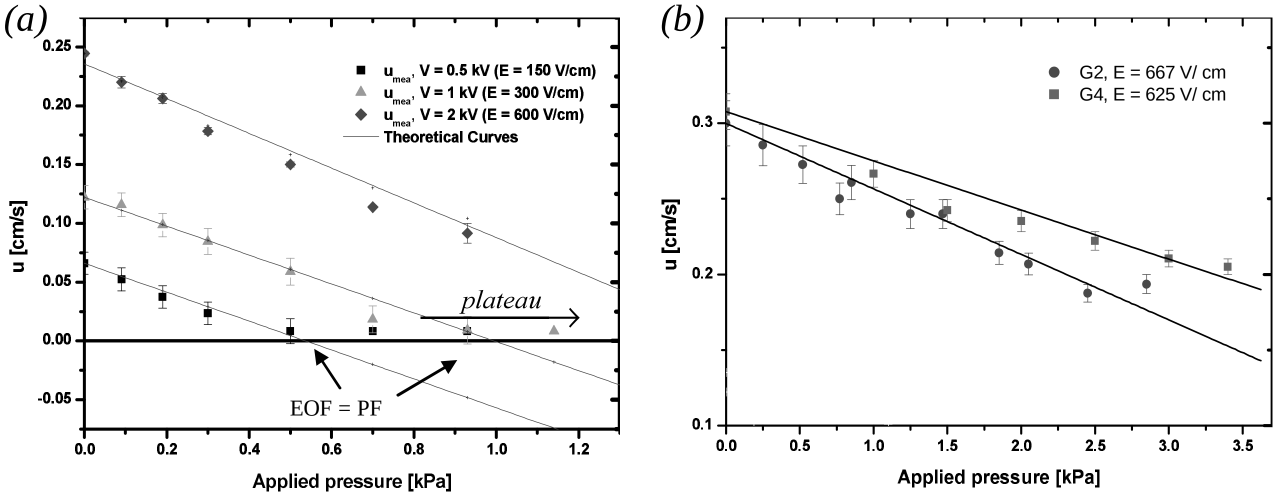

Figure 3.3
Measured average velocity as a function of the applied counter pressure along with the theoretical curves calculated from Eq 3.7. (a) Microchannel of uniform cross-section. The measured data were obtained through the current monitoring method using 10 and 9.5 mM sodium tetraborate buffer. (b) Three microchannels of uniform cross-section but with different dimensions. In this case, 25 mM and 23.8 mM carbonate buffer was used

Note that the observed u_{mea} at the intercepts, that is at $\Delta p = 0$, corresponds with Eq 3.7 which states that u_{mea} should be proportional to E. In Figure 3.3 *(a)*, the u_{mea} values converge to a minimum value at about 0.5 kPa and 0.95 kPa at $E = 150$ V/cm and 300 V/cm, respectively. This corresponds to a minimum $u_{mea} \leq 8 \times 10^{-3}$ cm/s. At that point, counter PF almost equals the EOF, and the average linear velocity is close to zero. Only a small current variation can be observed under these EOF and PF conditions. This current variation is probably not due to the EOF, but rather to diffusion of the 95 % concentrated buffer from R_3 into the microchannel, filled with 100% concentrated buffer. The EOF component becomes weaker at higher Δp until PF equals the EOF. At that point, the buffer of lower concentration, driven by EOF, never reaches R_1, where hydrostatic pressure is applied. However, the current continues to drop, indicating that the flow is bi-directional. Note that the current monitoring method does not allow direct determination of this point. Therefore, it is assumed that at higher Δp, when no current drop is observed, PF overcomes EOF and that the net flow is determined by PF (plateau region). For E = 600 V/cm, zero net flow was not reached.

E [V/cm]	**150**	**300**	**600**
Δp_{mea} [kPa]	*0.5*	*0.93*	-
Δp_{th} [kPa]	*0.54*	*1*	*2*
$\sigma_{\Delta p}$ [%]	*8*	*8*	-

Table 3.1
Theoretical set of applied pressures and electrical field strenghts required for zero net flow compared with experimental values and relative errors, $\sigma_{\Delta p}$, between Δp_{mea} and Δp_{th}.

The relative difference, σ_u ($\sigma_u = | u_{mea} - u_{th} | / u_{mea}$), between u_{mea} of Figure 3.3 *(a)* and the corresponding theoretical velocity calculated from Eq 3.7, u_{th}, is on average 17 % at E = 150 V/cm and 4 % at 300 V/cm for values above the theoretical zero net flow.

At E = 600 V/cm, σ_u = 2%. Thus, the higher the electric field, the more accurate Eq 3.7 is. Concerning the data of Figure 3.3 *(b)*, σ_u never exceeds 3 %.

Table 3.1 compares the theoretical applied pressures, Δp_{th}, calculated from Eq 3.7 and the corresponding experimental pressures, Δp_{mea}, required for having zero net flow for the three electrical field strengths used in Figure 3.3 *(a)*. Table 3.1 also shows the relative error, $\sigma_{\Delta p} = |\Delta p_{mea} - \Delta p_{th}|/\Delta p_{mea}$ between Δp_{mea} and Δp_{th}. The data in Table 3.1 show that Eq 3.7 gives a good approximation of the Δp_{mea}. The $\sigma_{\Delta p}$ between Δp_{mea} and Δp_{th} for zero net flow at E = 150 V/cm and 300 V/cm is about 8%.

It is important to realize that the ratio between the two geometric parameters *L* and D_H has a significant effect on the slope of these curves. For example, if *L* is constant, *w* = 10 µm and the microchannel depth is reduced from 20 µm to 10 µm, the slope decreases by 30 % and hence, hydrostatic pressure effects drop with the same percentage. If now *w* = 300 µm, with the same reduction in depth, the slope diminishes by 4 %. On the other hand, an increase of L by a factor 2 with *w* and *z* kept constant leads to a decrease of the slope by 50 % regardless of depth and the mask path.

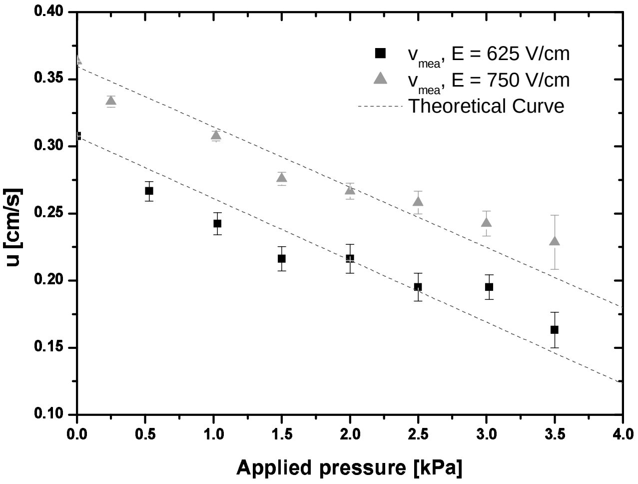

Figure 3.4
Linear velocity, u_{mea}, as a function of the Δp for two serpentine microchannels of uniform cross-section operated at E = 625 V/cm and 750 V/cm. The theoretical fits have also been included in this figure (dashed line).

The experimental and theoretical linear velocity of the device with serpentine layout, G8, is presented in Figure 3.4. The effect of hydrostatic counter pressure and the EOF on the average linear velocity is the same for the serpentine and the straight channels. The σ_u do not exceed 15 %. In spite of the relatively large values of Δp, the plateau region was not reached. From Eq 3.7, the Δp predicted by theory for zero net flow is about 8 kPa and 6.7 kPa at E = 750 V/cm and 625 V/cm, respectively.

The results that were obtained with straight and serpentine microchannels of uniform cross-section demonstrate the validity of Eq 3.7. This equation can therefore be used to estimate the consequence of possible differences in reservoir height on EOF at the channel reservoirs. For example:

- for G7 (L = 3.3 cm, z = 27 μm, w = 14 μm) a difference in height of 1 mm causes a 2 % decrease of the average velocity at 150 V/cm. The average velocity decreases to 0.5 % at 600 V/cm.
- for G3 (L = 5 cm, z = 20 μm, w = 10 μm) a difference in height of 1 mm causes a 0.009 % decrease in the linear velocity at E = 300 V/cm.

It follows from these examples that, depending on the chip design, even small changes in height between the microchannel inlet and outlet could adversely affect the reproducibility of the experiments, as observed for example on-chip CZE separations.

3.3.1.2 Devices with Diverging andCconverging Channel Elements

It was shown in the previous section that for straight channels of uniform cross-sections, the σ_u never exceeds 20 % for linear average velocities larger than zero. However, for microfluidic devices with diverging and converging elements, the u_{th} values calculated from Eq 3.15 deviate from the u_{mea} values above zero net flows. Furthermore, the relation between u_{meas} and the Δp for a given E seems to become non-linear. This is illustrated by Figure 3.5, where the u_{mea} values for DC2 and DC3, measured with the current monitoring method, are plotted as a function of the applied pressure for several fixed E.

Experimental results obtained for DC2 at 385 V/cm and 577 V/cm fit well with the theoretical curves with a maximum σ_u of 10 % and 5 %, respectively. However, at 256 V/cm, the maximum σ_u is about 50 % at pressures over 1.2 kPa. The difference between theoretical and measured velocities is more pronounced for DC1, which is shorter and deeper than DC2. The σ_u at 334 V/cm reaches a maximum of 130 % at 1.5 kPa. For 667 V/cm, the maximum σ_u is about 190 % at 2.5 kPa. According to these data, Eq 3.15 ceased to be accurate as the average linear velocity approached zero. Assuming that current monitoring is reliable for the values of the velocities above zero, the deviation between theory and experiment can be explained by the generation of minor losses. These additional losses could be due to a flow separation at the convergent and divergent channels in the presence of a bi-directional flow. To validate whether this hypothesis is true, three questions need to be answered:

1) Is the flow really separating and therefore inducing eddies or vortices responsible for minor losses?
2) Why is the flow somehow separating although the Reynolds number is < 1 in the microfluidic devices investigated?
3) How does the flow separate, if it separates at all?

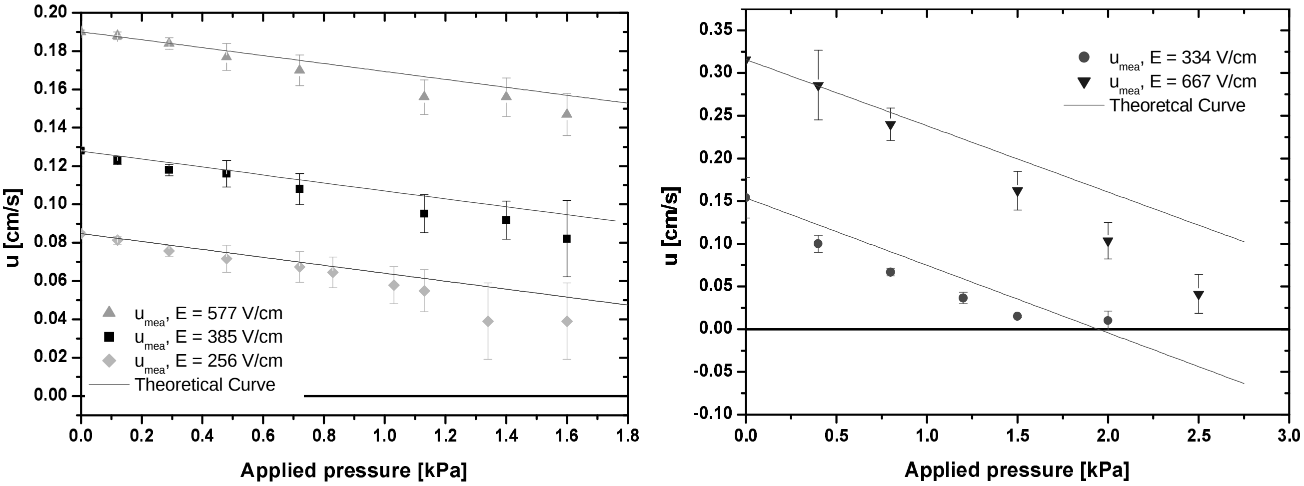

Figure 3.5
Linear velocity measured as a function of Δp for different E. Curves are calculated from Eq 3.15. Left hand side: data for DC2 ($\alpha^{-1} = 6.8x10^{-9}$ μm). Right hand side: data for DC1 ($\alpha^{-1} = 2.5x10^{-8}$ μm).

To answer these questions, a detailed study of the fluid motion in the microfluidic devices is required. Two different technologies are used for this study: 1) streamline visualisation with polystyrene micro-beads and 2) streamline modelling using CAD tools. These two methods are treated in section 3.2.2 and Chapter 4, respectively.

3.3.2 Flow Visualization with Polystyrene Beads

In section 3.3.1 it has been shown with the current monitoring method that when EOF and PF coexist in opposite directions, a zero net flow regime can be observed. However, current monitoring is limited at zero net flow. This method does not allow the investigation of region where pronounced bi-directional flow is formed. To study the flow in more detail around zero net flow and to check whether a bi-directional flow is generated at zero net flow according to Eq 3.7, visualisation of the streamlines is required. It was decided to use polystyrene latex beads to determine the region of applied pressure where flow becomes bi-directional at a given potential. Different types of beads (fluorescently and non- fluorescently labelled beads, ranging in diameter from 1 μm to 6 μm) and chips were used successfully to investigate flow pattern under conditions where EOF and PF are opposed.

3.3.2.1 Beads in Microchannels of Uniform Cross-section

Video imaging of 2-μm polystyrene beads (Polysciences, Germany) was used to observe flow patterns in the microchannels. The original bead buffer was replaced by the 10 mM sodium tetraborate buffer (pH 9) by centrifugation prior to use (see Chapter 2).

The 2-μm beads were introduced within the microchannels by electro-osmotic pumping without a counter pressure, verifying that beads follow the EOF profile. The schematic of Figure 3.6 illustrates the evolution of the velocity flow profile, according to observations with beads.

The flow of beads is homogeneous (weak dispersion) and laminar under the influence of the EOF. The beads follow the flat flow profile of the EOF, which is typical for electro-osmotic transport (Figure 3.6 (a)). As observed by Pfahler [21] and Santiago [22] for PF at low Reynolds number, the beads describe a creeping flow. It was observed that for a given pressure, a bi-directional flow is obtained over a range of *E*. In fact, video imaging shows that the equilibrium between the two opposed laminar flows changes gradually as a function of the potential (Figure 3.6 (b) and (c)). When beads are merely transported by PF, the flow is laminar (creeping flow), and the beads describe a parabolic flow profile (Figure 3.6 (d)).

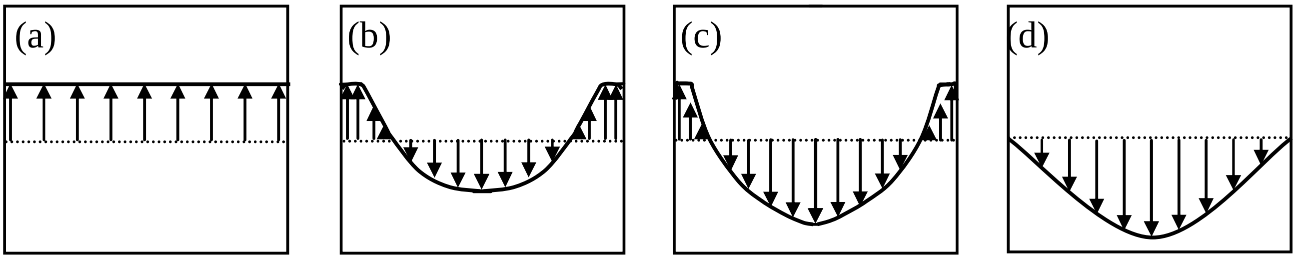

Figure 3.6
Diagrams of the 2-μm beads velocity distribution at different sest of E and Δp in a straight microchannel. (a)Δp = 0 kPa, E > 0V. The velocity profile is flat. (b) The PF and the EOF are in equilibrium: the bi-directional flow of beads is fully developed ($u_{EOF} = u_P$). (c) PF starts to overcome the EOF. (d))Δp > 0 kPa, E > 0V but the PF overcomes the EOF. A fully developed laminar flow of beads induced by hydrostatic pressure is established across the microchannel. Note that when bi-directional flow of beads is fully developed, the average bead velocity is close to zero (see next sections). At the same time, however, video imaging shows that beads are continuously in movement under these conditions.

The data plotted in Figure 3.7 delineate the region of E and Δp where the beads describe a bi-directional flow for G7. For Δp = 0.19 kPa, a bi-directional flow of 2-µm beads is observed between 120 V/cm and 360 V/cm. At 0.19 kPa and 120 V/cm, most of the beads are driven by PF and only beads present along the walls, in a thin layer of about 5 µm, are driven by EOF. As the electrical field strength is increased from 120 V/cm to 240 V/cm, the core of the microchannel, where PF is predominant, gradually contracts while effects of EOF becomes more visible in the microchannel, e.g. the velocity of the beads present around the core becomes larger. The layer thickness where beads are driven by EOF is then increased from 3 µm to about 8 µm.

At 240 V/cm, movement of beads indicates that the bi-directional flow is fully developed and the average linear velocity should be zero (Figure 3.6 (b)). The results obtained with the beads show that: 1) two well-defined regions of laminar flow (creeping flow) are generated in opposite directions (Figure 3.6 (b)). The beads present in the core region, where the PF dominates, occupies a little bit more than half of the microchannel width (~ 45 µm) whereas the EOF dominates the rest of the microchannel width 2) the average velocity of the beads in the core, driven by PF, is roughly equal to the velocity of the beads along the walls, driven by EOF. As the *E* continues to go up, the region where beads are driven by EOF widens until the EOF overcomes the PF, leading to the movement of the beads in one direction, which is determined by the EOF (*E* > 360 V/cm, Figure 3.6 (a)).

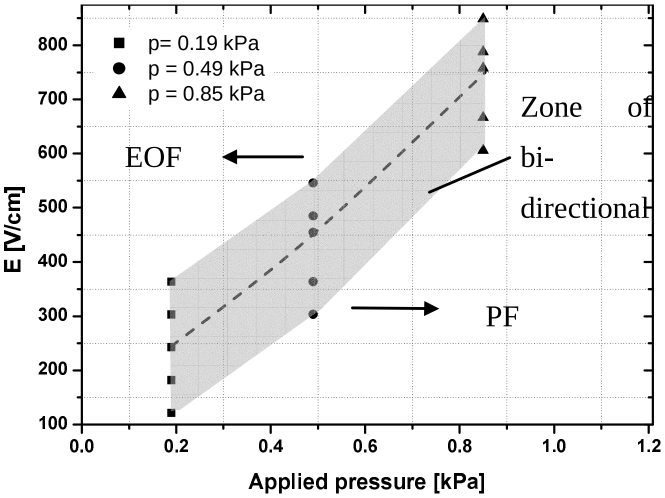

Figure 3.7
Boundary conditions for bi-directional flow of 2-µm polystyrene beads for G7. 2-µm polystyrene beads (Polysciences) are used to visualize the flow in a straight microchannel of uniform cross-section. The dashed curve indicates the boundary conditions under which bi-directional flow of the 2-µm beads is fully developed for the device G7 as determined experimentally with video imaging.

The use of beads ranging between 1 μm and 6 μm confirmed these observations. These observations indicate that the flow profile of the beads is in agreement with the flow profile predicted by theory when EOF and PF are opposed in a microchannel of uniform cross-section [5-7].

3.3.2.2 Beads in Diverging and Converging Elements

It was assumed in section 3.3.1.2, that additional losses were generated when bi-directional flow is employed in a microfluidic device with gradual contraction and expansion elements. These additional losses are generally associated with minor losses in conventional macroscopic systems that materialize when flow separates from the channel walls. Flow separation gives rise to uncontrolled eddies or uncontrolled vortex motion. However, flow separation generally does not occur at low Reynolds number, which is the norm in most microfluidic applications. In section 3.3.1.2, some significant mismatches were observed between the theoretical values of the velocity calculated from Eq 3.15 and the measured average linear velocity when bi-directional flow was present in the microfluidic devices with non-uniform cross-section. In these experiments, flow rates rarely exceeded 0.1 nL/s and the Re never exceeded 0.2. One method to understand if flow separates is to use beads with the purpose of inspecting the flow pattern at the diverging and converging elements. The experiments with beads consisted of three steps:

<u>Bead loading:</u> Beads are introduced within the device by application of a hydrostatic pressure on R_3 (of DC1, DC2 or DC3). Video imaging shows that beads never separate from microchannel walls when they pass through the diverging elements, even for flow rates of about 1 nL/s.

<u>Recirculating flow generation:</u>

As soon as the beads reach the 2nd converging microchannel element, a potential is applied between R_1 and R_3 so that a counter EOF is induced. The electric field is tuned with respect to PF in order to generate rotational flows at the diverging elements, as confirmed by the formation of (re-)circulating bead clusters as shown in Figure 3.8.

Bead flushing:

When EOF overcomes PF, beads are pushed back towards R_3 without separating from microchannels walls.

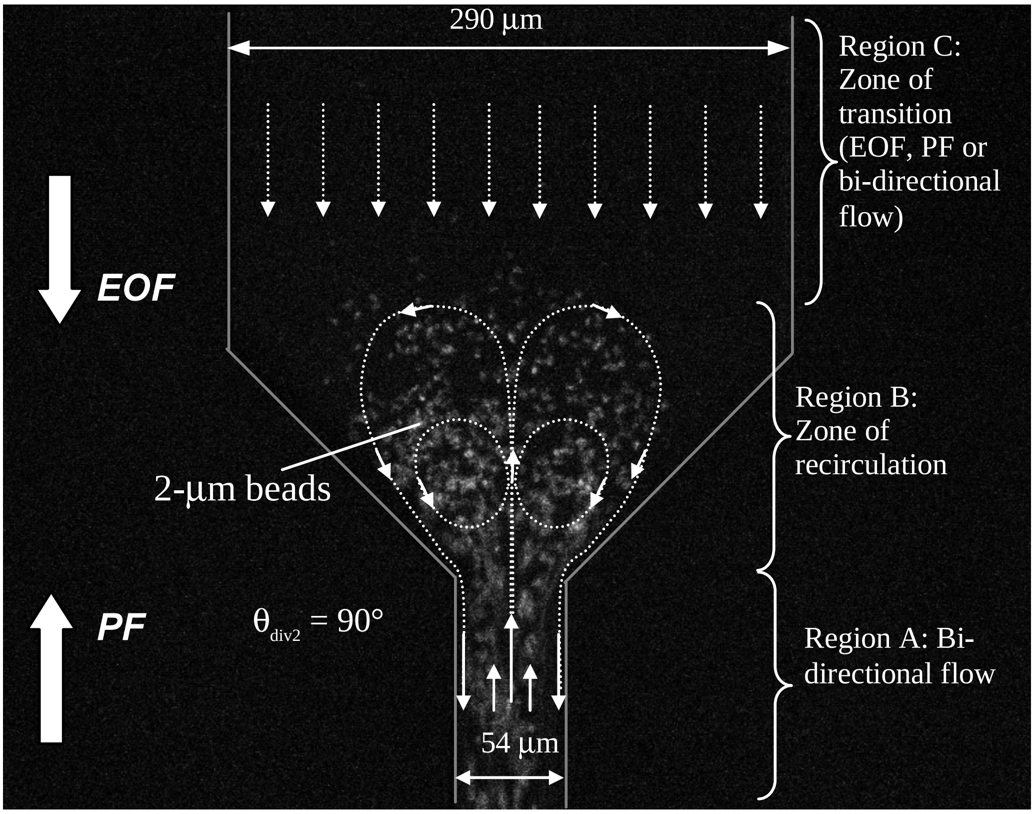

Figure 3.8
Steady circulatory flow patterns, visualized by the cluster of freely moving beads, under the influence of EOF and PF (E = 150 V/cm, Δp= 0.5 kPa) at the 2^{nd} diverging microchannel element.

The picture in Figure 3.8 was taken with a fluorescent microscope that used a video imaging system. It shows (re-)circulation of 2-µm fluorescent beads (λ_{ex} = 490 nm, λ_{em} = 524 nm) at the 2^{nd} diverging microchannel element. In this case, Δp = 0.5 kPa and E = 150 V/cm, θ_{div2} = 90° and A_4/A_1 = 5.4. The solid arrows designate the direction of EOF and PF, whereas the dashed arrows indicate the movement of the beads under these particular conditions. Three regimes of flow can be distinguished in Figure 3.8.

Region A:

The flow of beads in Region A is bi-directional. Beads are flowing along the walls of the narrow microchannel situated before the gradual expansion (divergent element entrance), driven by EOF, while beads present in the core are driven by PF. It is exactly the same kind of flow observed in section 3.3.2.1 and schematically presented in Figure 3.6 (b) and (c). The visualisation with beads confirmed that a fully developed bi-directional flow of beads forms under conditions close to zero net flow in these devices too. Experiments showed that the bi-directional flow of beads is present in the narrow segments every time that recirculating flows are generated at diverging and converging elements.

Region B:

Video imaging showed the formation of recirculating flows between regions A and C, that is between the expansion of the narrow microchannel and the end of the diverging element. Beads coming from the core of the bi-directional flow in Region A, driven by PF, are suddenly deflected towards the walls as they enter the diverging microchannel element. Once beads come in the proximity of the diverging element walls, they undergo the influence of electro-osmosis. Thus, most of the beads return into the narrow channel, in region A, driven by EOF, describing the recirculating trajectory sketched (dashed arrows) in Figure 3.8. Video imaging also show that some beads are caught in a sort of vortex motion pattern (see Figure 3.9) where they are caught for a given time. In this case, beads do not always immediately reach region A. Once generated, the global bead recirculation at the diverging microchannel element is very stable and reproducible. It is also fascinating to notice that beads delineate globally a pair of symmetrical recirculating areas of flow around an axis located at the centre of the device. This is more visible in Figure 3.9 *(a)*, which shows the integration of 19 images of recirculating beads over 4 s.

Region C:

In this region, under the specific boundary conditions used in this experiment, beads are deflected by EOF towards the diverging microchannel element. Beads can then not go further than the diverging microchannel element (no loss of beads): the recirculating flows of beads is fully developed (Figure 3.8 and Figure 3.9 *(a)*). For comparison, Figure 3.9 *(b)* shows the situation where flow is bi-directional in Region C while recirculating flows are generated in Region B. In this case, the recirculating flows are stable but not fully developed.

It is important to stress that the recirculating flows visualized described by the beads only occur for a specific range of *E* at a fixed Δp. As *E* increases, EOF determines more and more the net flow in Region C while beads are still recirculating in region B. This continues until the *E* becomes so high that EOF overcomes completely PF. Then, the bi-directional flow and the recirculation of the beads cease simultaneously and beads are carried away by the EOF. The effects of tuning *E* for a given pressure and details about boundary conditions for recirculating flows of beads will be discussed in Section 3.5.

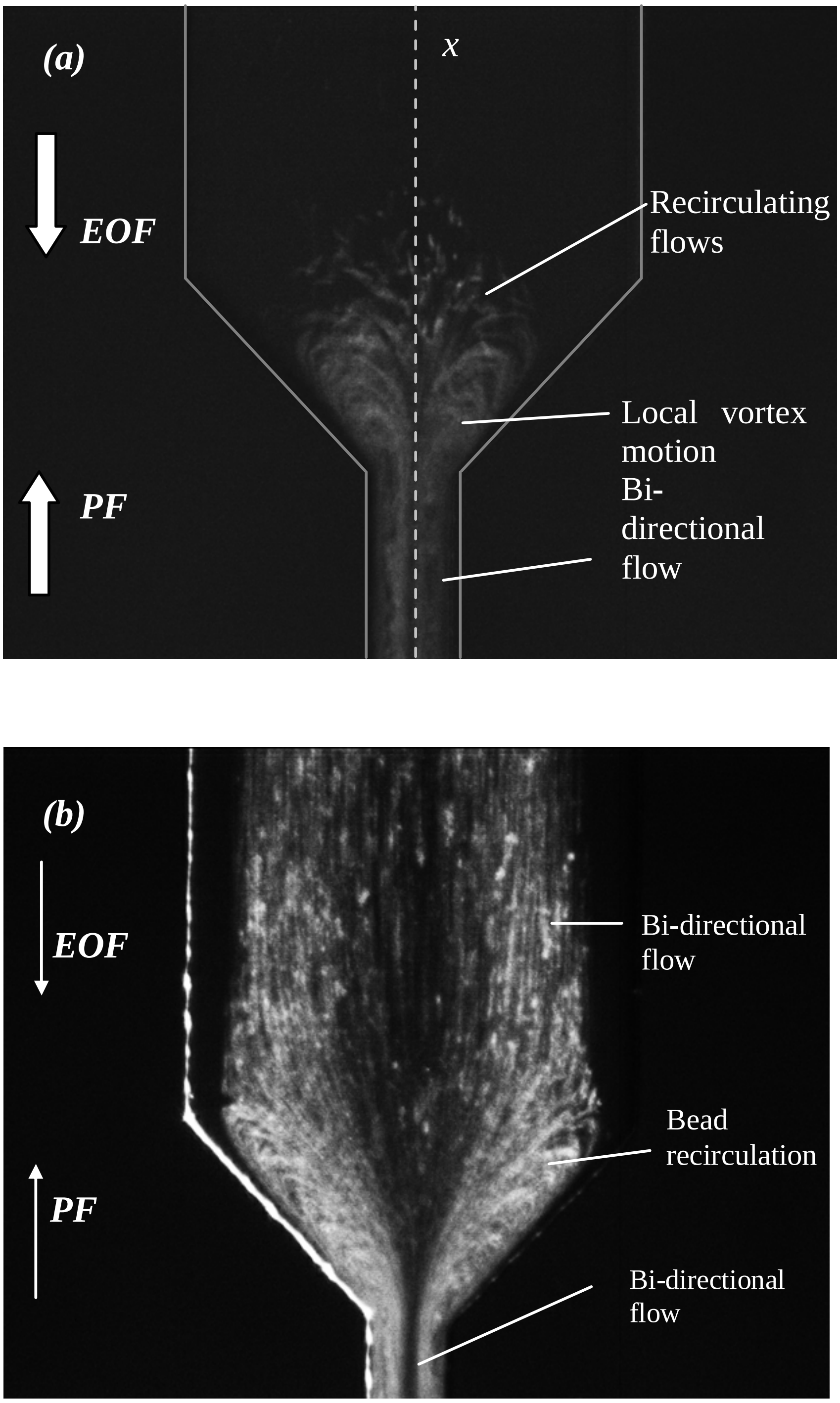

Figure 3.9
Streaklines of the recirculating flows at the 2nd diverging microchannel element obtained by integrating frames over time (5 frames/s). The pictures help to visualize the recirculating flows. (a) Fully developed recirculating flows ($E = 150$ V/cm, $\Delta p = 0.5$ kPa). A certain symmetry can be observed around the x axis (dashed line). (b) The recirculating flow of beads is not fully developed ($E = 130$ V/cm, $\Delta P = 0.5$ kPa).

Figure 3.10 shows the resulting bead recirculation at the 1st converging microchannel element. These recirculating flows are generated at the same time as the recirculating flows at the diverging elements. Like at the diverging element, three regions of different flow patterns can be distinguished. In all these regions, the flow behaviour shows similarities as observed for the diverging microchannel elements, that is, a bi-directional flow of beads, a zone of bead recirculation and a transition zone, respectively. There are, however, some differences which are observed in Region B and C:

- Beads coming from the narrow microchannel, driven by EOF along the walls, separate from the walls and reverse direction towards the core of the narrow microchannel.

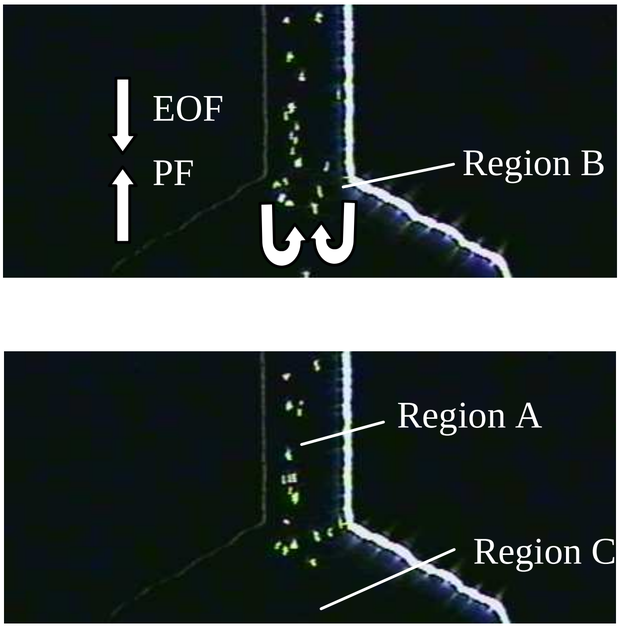

Figure 3.10
Snap shots of bead recirculation at the convergent microchannel element at E = 150 V/cm and Δp = 0.5 kPa.

- The bead flow behaviour in Region C is more intriguing than for diverging channel elements because the recirculating flow of beads is hardly fully developed. The net flow is never dominated by PF when recirculating flows are generated. In Region C, flow is either bi-directional or dominated by EOF. Interestingly, even when EOF seems to be predominant in this region, beads continue to describe recirculating flows (this situation will be explained in Chapter 4).

According to the dimensions of the devices considered in this study, $L/D_H \cong 3$ when L is the length of the diverging or converging element and D_H, the hydraulic diameter of the narrow segment. Alternatively, $L/D_H \cong 70$ when L is the length of the wide segments and D_H, the hydraulic diameter of the narrow segment. Using Eq 1.6 (Chapter 1, section 1.3.1) for linear velocities ≅ 0.3 cm/s, $\mathrm{Re}_t \cong 100$ in the former case and $\mathrm{Re}_t \cong 2300$ for the latter. For comparison, using the same linear velocity and D_H, $\mathrm{Re} \cong 0.12$. Therefore, regardless of the fact that recirculating flows happen when the average linear velocity approaches zero, recirculating flows are definitively not obtained in a turbulent flow regime.

3.3.2.3 Apparent Electrokinetic Mobility of the Beads

Beads seem to follow accurately the streamlines induced by opposing the EOF to the PF. Moreover, initial experiments with negatively charged, fluorescent, 2.5-μm polystyrene beads (Alignflow, Molecular Probes), whose mobility opposes the EOF, seem to indicate that bi-directional flow of beads forms under conditions close to the point of zero net flow in the microchannel at E and Δp, as predicted by Eq 3.7. However, video imaging indicates that flow considerations do not always reveal the whole story with respect to bead behaviour. The electrokinetic mobility of the beads (μ_{beads}) themselves has also proven to play a significant role in determining under which electric field and pressure conditions bi-directional flow of beads is formed experimentally. This becomes increasingly true for beads with high, well-defined surface charge densities.

The influence of μ_{beads} on the E and the Δp under which a bi-directional flow is formed follows from Eq 3.4 and Eq 3.7:

$$u_{beads} = (\mu_{EOF} \pm \mu_{beads})E - \frac{\Delta p}{32\eta}\frac{D_H^2}{L} \qquad \textbf{Eq 3.17}$$

where u_{beads} is the average velocity of the beads. For beads with a mobility in the same direction as the EOF, μ_{beads} is positive. For those whose mobility is against the EOF, μ_{beads} is negative (this is true for negatively charged beads). The same buffer and type of beads are used to measure μ_{beads} for the visualization of the streamlines, since μ_{beads} depends on buffer pH [23]. The beads used for flow visualisation are negatively charged. When no counter pressure is applied, they follow the EOF. The buffer used is a 10 mM sodium tetraborate buffer (pH = 9, $\mu_{EOF} = 5.7\times 10^{-4} \pm 0.3$ cm^2/Vs). Hence, since the beads follow the EOF, $|\mu_{beads}| < \mu_{EOF}$. To estimate μ_{beads} in this buffer, the displacement times of beads driven by EOF, t_{beads}, were measured over a determined distance, L_{beads} at different E and at $\Delta p = 0$. Measurements of t_{beads} were performed using video imaging in a straight microchannel of uniform cross-section. Using Eq 3.17 at $\Delta p = 0$ gives for the apparent mobility μ_{app}:

$$\mu_{app} = \mu_{EOF} - \mu_{beads} = \frac{L_{beads}^2}{Vt_{beads}} \qquad \textbf{Eq 3.18}$$

The electrokinetic mobility of 2-µm polystyrene beads was estimated to be: $\mu_{beads} = -(4 \pm 0.4)\times 10^{-4}$ *cm*^{2}*/Vs*. For the 2.5-µm beads, discussed at the beginning of this section, the electrokinetic mobility was estimated to be: $\mu_{beads} = -(1.3 \pm 0.4)\times 10^{-4}$ *cm*^{2}*/Vs*. The maximum electric field in these experiments was 850 V/cm. At higher electric field, polystyrene beads cease to behave independently from each other but tend to form straight chains of about 10-15 beads connected together. Even if these chains seem to follow the streamlines, the electrokinetic mobility is apparently modified (integrity of μ_{beads} is not ensured anymore). Not unexpectedly, bead size also plays a role in particle mobility, with larger particles (> 4 µm) apparently subject to higher frictional losses in the flow than smaller particles. Experiments performed with 0.5-µm and 6-µm Fluoresbrite microspheres (Polysciences) using 30 mM carbonate buffer (pH = 8.9) showed that their electrokinetic mobilities was strong enough that they flowed in an opposite direction to the EOF. Thus, it is not obvious to predict E

and Δp under which bi-directional flow could be accomplished, without additional knowledge about the electrokinetic mobility of the particles themselves.

3.3.2.4 Bidirectional flow of beads and bi-directional flow of buffer

Table 3.3 summarizes the set of E and Δp values at which the bi-directional flow of beads is fully developed from Figure 3.7 and the corresponding u_{beads} calculated from Eq 3.18 for G7. Table 3.3 also shows the average velocity of the sodium tetraborate buffer, u_{th}, calculated from Eq 3.7. The plots of Figure 3.11 illustrate the u_{beads} calculated from Eq 3.17 as a function of the pressure for the three electrical field strengths.

Δp [kPa]	0.19	0.49	0.85
E [V/cm]	240	455	758
$\bar{u}_{beads}$ [cm/s]	-5.44×10^{-3}	-2.5×10^{-3}	-8.24×10^{-3}
$\bar{u}_{buffer}$ [cm/s]	1.09×10^{-1}	1.88×10^{-1}	3.08×10^{-1}

Table 3.3
Boundary conditions for bead bi-directional flow and the resulting theoretical 2-μm polystyrene beads ($\mu_{beads} \cong 4x10^{-4}$ cm^2/Vs) and sodium tetraborate buffer average velocities.

Several important indications come out from Table 3.3 and Figure 3.12. The dashed circles in Figure 3.11 indicate the u_{beads} for which fully developed bi-directional flow of beads was observed within the microchannel of uniform cross-section. Note that u_{beads} is close to zero when bi-directional flow of beads is observed. This demonstrates that Eq 3.18 is a good approximation. (Thus, the fact that μ_{beads} of the 2.5-µm beads mentioned previously is small explains why it was thought in initial experiments using these beads that bi-directional flow of the buffer happened roughly at the same E and Δp as for the beads.)

The data of Table 3.3 indicate that the average velocity of the buffer is not equal to zero when bi-directional flow of beads is observed. Moreover, the average velocity of the buffer tends to increase as E and Δp increase. This is a direct consequence of Eq 3.18. By subtracting the μ_{beads} to μ_{EOF} it is implicitly admitted that beads behave like molecules in a buffer. It would be more adequate to say that beads behave like a "fluid into a fluid". Therefore it is important in this work to differentiate a bi-directional flow of beads from a bi-directional flow of the buffer.

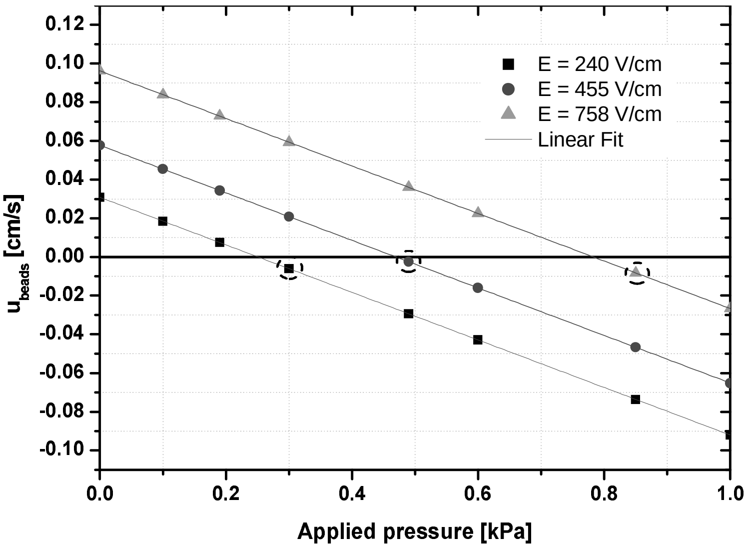

Figure 3.11
Linear velocity of the 2-μm beads calculated from Eq 3.17 as a function of the applied pressure for G7. The circles show u_{beads} for which fully developed bi-directional flow of beads was observed within the microchannel.

Since Figure 3.12 shows that bi-directional flows of beads are formed close to zero net flow, this should also happen to the buffer itself. In section 3.3.1, it was observed close to zero net flow that buffer of lower concentration was still moving towards the reservoir with the buffer of higher concentration without ever reaching it. It can be imagined that because of the presence of a bi-directional flow, the two buffers of different concentrations mix together in the straight channel. As a result, a 97.5% buffer is gradually obtained in the whole straight channel, explaining why current never reaches I_{min} but stabilized between I_{max} and I_{min}.

The results obtained in this section indicate that bi-directional flow takes place roughly at zero net flow, as predicted by theory. However, the bi-directional flow of bulk solution and bi-directional flow of beads are different, occurring under slightly different conditions due to the contribution of the electro-osmotic mobility, μ_{beads}, to bead motion. To quantitatively characterize bead flows, μ_{beads} must be known.

3.3.2.5 Consequences of Recirculating Flows: Discussion

The results obtained with beads for streamline visualization confirm the assumptions made in section 3.3.1.2, namely, that minor losses are occurring in devices of non-uniform cross-section under conditions of bi-directional flow. At the same time, some interesting phenomena were observed.

Experiments performed with beads in microchannels revealed the existence of recirculating flow patterns at diverging and converging microchannel elements under conditions close to zero net flow. Recirculating flows explain the mismatch observed in section 3.3.1.2 between the predicted values of the mean velocity calculated from Eq 3.15 and the measured velocities, since recirculating flows are responsible for additional losses.

It was assumed previously that recirculating flows should be taken into account in the theoretical model to reduce this mismatch. Additional losses were assumed to originate from separation from the microchannel walls as is the case in macrofluidic systems [8, 9]. However, experiments with beads demonstrate that this is not exactly correct. In the case of the diverging microchannel elements, bead flows are directed from the core towards the walls, where they are subject to the influence of EOF. Therefore, separation of the flow occurs from the centre of the microfluidic device in contrast to what is observed in macroscopic systems. For the converging microchannel elements, the flow pattern is more conventional, with bead flow driven by EOF separating from the converging channel walls towards the core of the narrow microchannel where PF is predominant.

Another interesting phenomenon revealed by the experiments performed with beads is that the establishment of steady recirculating flows of beads happens simultaneously at each diverging and converging microchannel element, along with bi-directional flow of beads in the narrow channels. The streamlines shown schematically in Figure 3.12, substantiated by experiments performed with beads (diameter ranging between 1 and 6 μm), gives a sort of summary of the flow pattern observed at diverging and converging channel geometries when EOF and PF are in equilibrium. Thus, the flow patterns brought to light by the beads are extraordinarily ordered, as well as reproducible, symmetric and fully controllable. The control of recirculating flows of beads, and thus indirectly, the control of recirculating flows is discussed in the Section 3.5.

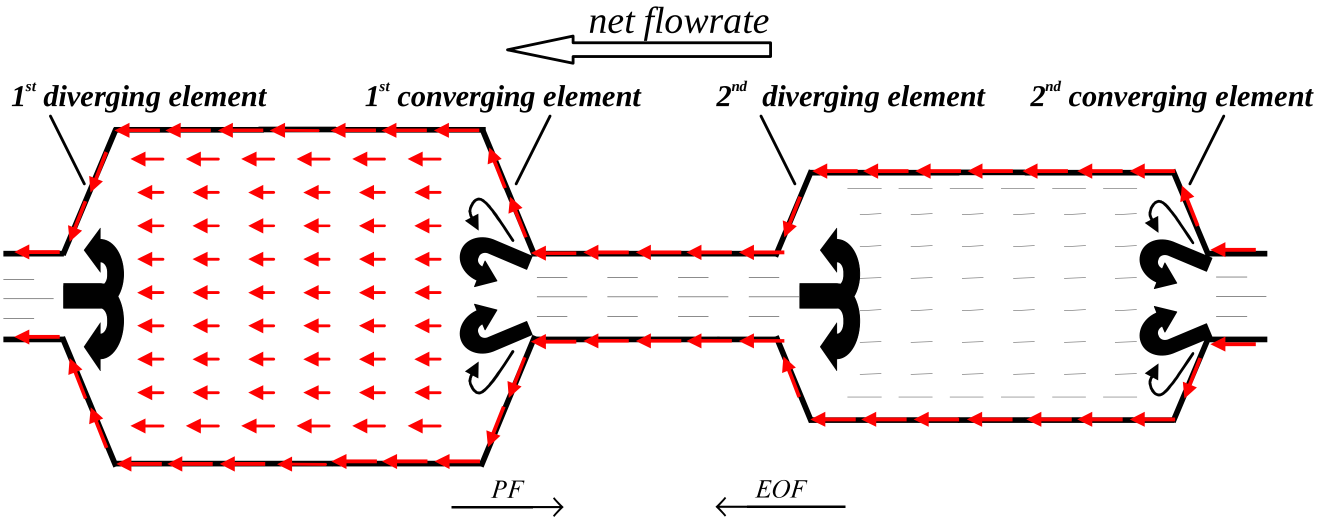

Figure 3.12
Top schematic view of the microfluidic "vortex" device. Streamlines in the plane halfway between the top and bottom of the channel (parallel to the page) are shown. EOF and PF conditions are such that the average velocity of the beads is close to zero. In the large channels, streamlines of the flow follow EOF. A pair of symmetrical vortices is generated at each end of the trapping channel, and flow recirculates between the diverging and converging channel elements through this channel.

The most interesting aspect of the fluid behaviour, revealed experimentally through the use of beads, is that the beads can be captured and preconcentrated in the narrow channel between the diverging and converging channel elements, to form clusters of freely moving beads at both these elements. This phenomenon will be the main topic of the application introduced in Chapter 5.

3.4 Model for Recirculating Flows and Bead Clusters Formation

Experiments described in section 3.3.2 proved that steady recirculating flows could be formed at diverging and converging elements although Re << 1. This implies that minor losses have to be taken into account in order to calculate the average linear velocity when EOF and PF are opposed in microfluidic devices with channel expansions or contractions elements. For macroscopic pipe systems with diffuser and nozzle elements under conditions of PF, the measured minor loss is given by the loss coefficient *K*. In this work, recirculating flows are generated by the combination of a bi-directional flow with microchannel geometry featuring diverging and converging elements. Thus, in these microsystems, the loss coefficient, K_μ , has to be related to both geometry and bi-directional flow. K_μ is an empirical value characterizing a single diverging or converging element as a function of Δp and E: $K_\mu = f\,(\theta, A_2/A_1, E, \Delta p)$. Theoretically, estimation of K_μ requires flow rate measurements of single diverging/converging elements under the effect of a bi-directional flow. The total head loss across the microfluidic system would be given then by Eq 3.2 replacing K_i by $K_{\mu i}$:

$$\Delta h_{tot} = \sum_i (h_{fi} + h_{m\mu i}) = \sum_i \frac{u_{p_i}^{\,2}}{2g}\left(\frac{f_i L_i}{D_{Hi}} + K_{\mu i}\right) \qquad \textbf{Eq 3.19}$$

where $h_{m\mu i}$ is the minor loss associated to the diverging/converging element *i* in the presence of a bi-directional flow.

3.4.1 Development of a Model for Devices with non-uniform Cross-sections

In this work, microchannel systems containing 2 pairs of diverging/converging elements were studied. The total head loss across these systems is given by Eq 3.19 when EOF is opposed to PF:

$$\Delta h_{tot} = h_f + h_{m\mu} = \frac{32\eta\alpha}{\rho g} u_{p1} + \frac{(K_{\mu 1}u_{p1}^2 + K_{\mu 2}u_{p2}^2 + K_{\mu 3}u_{p3}^2 + K_{\mu 4}u_{p4}^2 + K_{\mu 5}u_{p5}^2)}{2g} \qquad \textbf{Eq 3.20}$$

From Eq 3.10, all the velocities can be expressed as function of the linear velocity u_{p1}. Thus, Eq 3.20 becomes:

$$\frac{\Delta p}{\rho g} \cong \frac{32\eta\alpha}{\rho g} u_{p1} + \frac{k_\mu}{2g} u_{p1}^2 \qquad \textbf{Eq 3.21}$$

where k_μ is the sum of all the individual loss coefficients, $K_{\mu i}$. Development of Eq 3.21 gives for u_{p1}:

$$u_{p1\pm} \cong \frac{-64\eta\alpha \pm \sqrt{(64\eta\alpha)^2 + 8\rho k_\mu \Delta p}}{2\rho k_\mu} \qquad \textbf{Eq 3.22}$$

When no pressure is applied to the system, the velocity across the system must be zero. Therefore only u_{p1+} is valid. Since the flow rate is constant across the system, when a counter PF is opposed to EOF, the average linear velocity is given by:

$$u_{ave} = u_{EOF} - u_{p1} \cong \mu E - \frac{-64\eta\alpha + \sqrt{(64\eta\alpha)^2 + 8\rho k_\mu \Delta p}}{2\rho k_\mu} \qquad \textbf{Eq 3.23}$$

Steady recirculating flows are generated under conditions where the average linear velocity across the system is zero, that is $u_{EOF} = u_{p1}$. This condition allows the estimation of k_μ . Development of Eq 3.23 when $u_{EOF} = u_{p1}$ leads to find for k_μ:

$$k_\mu \cong \frac{2\Delta p - 64\eta\alpha\mu\ E}{\rho(\mu E)^2} \qquad \textbf{Eq 3.24}$$

This estimate of k_μ provides a link between u_{EOF} and u_1 and therefore a relation between EOF and PF. This equation is valid for E and $\Delta p > 0$ in microfluidic devices with non-uniform cross-sections. For a given E, k_μ increases linearly as a function of the applied pressure.

Comparison of u_{ave}, calculated from Eq 3.23, with u_{mea}, obtained experimentally, shows that the theoretical curves have the same behaviour as the experimental values. This is already an important improvement compared to the theoretical curves obtained using Eq 3.15. This is illustrated in Figure 3.13 *(a)*, where the data of DC2, obtained in section 3.3.1.2, are plotted along with the corresponding theoretical curves calculated from Eq 3.23 using Eq 3.24 for k_μ.

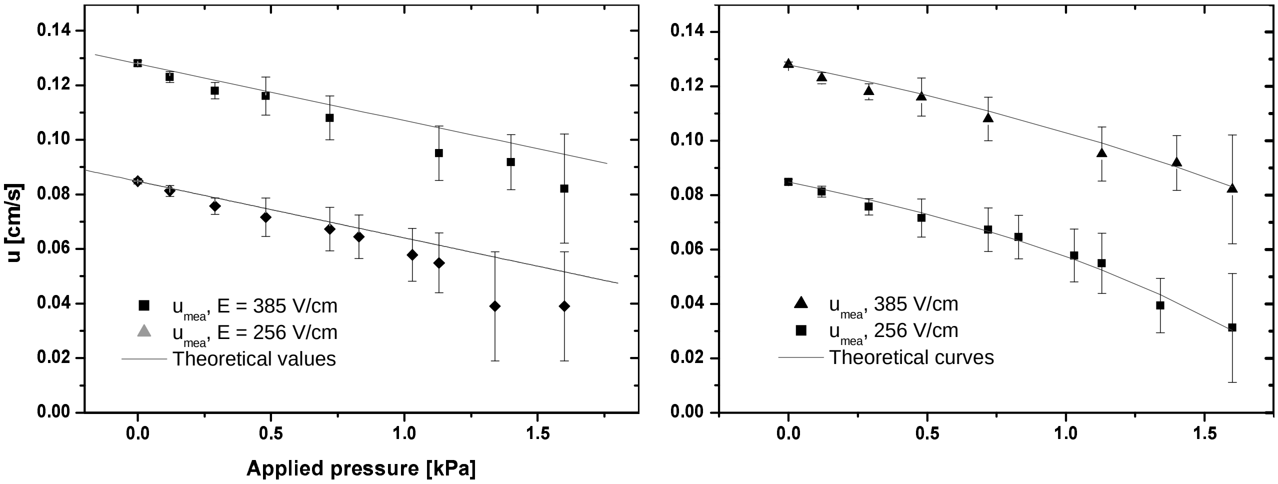

Figure 3.13

Comparison of u_{mea} and u_{ave} calculated from Eq 3.23 using Eq 3.24 for k_μ. (a) Data obtained with DC2 (b)Data obtained with DC3. In this case, it can be seen that u_{ave} drops to zero while u_{mea} tends to V_T.

On the other hand, the data obtained for DC3 (Figure 3.14) show that the theoretical values of the average velocity calculated from both Eq 3.15 and Eq 3.23 ceases to ollow accurately the u_{mea} values in the vicinity of zero net flow (this can not be seen in Figure 3.13 since the zero net flow is not reached). There are two possible explanations: either the models developed are not accurate enough or the current monitoring method becomes unreliable close the zero net flow. In the latter case, as the average linear velocity approaches zero the recirculating flows become more significant. The presence of the recirculating flows increases the mixing rate of the buffers of 95% and 100% leading to erroneous measurements. On the other hand, the higher the operating *E* and *Δp*, the faster should be the mixing rate when PF equals the EOF. Therefore, it is assumed that the current monitoring method is limited close to zero net flow. Eq 3.15, based on the independency of EOF regard to PF, is accurate when $u_{ave} >> 0$ but is limited when u_{ave} approaches zero due to the presence of recirculating flows. The use of Eq 3.23 that takes into account the dependency of EOF with PF is more accurate than Eq. 3.15 to calculate u_{ave} close to zero net flow.

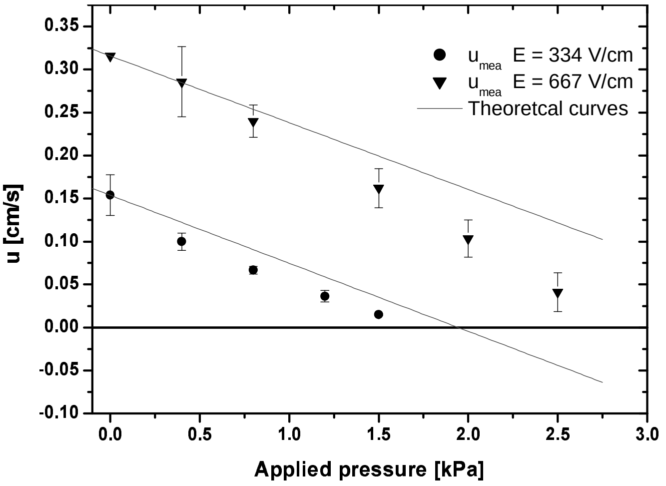

Figure 3.14
Plots of the theoretical velocity calculated from Eq 3.15 (u_{ave}) and theoretical curves calculated from Eq 3.23, using Eq 3.25 for the estimation of k_μ as a function of the applied pressure for DC3.

3.4.2 Application: Prediction of Bead Cluster Formation

From the experimental results of section 3.3.2.2, it can be concluded that fully developed recirculating flows of beads are generated under conditions where the average velocity across the system is close to zero. Eq 3.23 can then be used to predict under which *E* and *Δp*, bead clusters are formed. This is only possible if μ_{beads}

is known beforehand d for a given buffer. By replacing μ by μ_{EOF} - μ_{beads} in Eq 3.23, the E necessary to form fully developed recirculating flows (u_{ave} = 0) of beads is given by:

$$E = \frac{\Delta p}{32\eta\alpha(\mu_{EOF} - \mu_{beads})} \qquad \textbf{Eq 3.25}$$

E is proportional to the difference of applied pressure at the inlet and the outlet divided by α (that depends on geometry), and also to the difference between the electroosmotic mobility of the buffer and the apparent electrokinetic mobility of the beads.

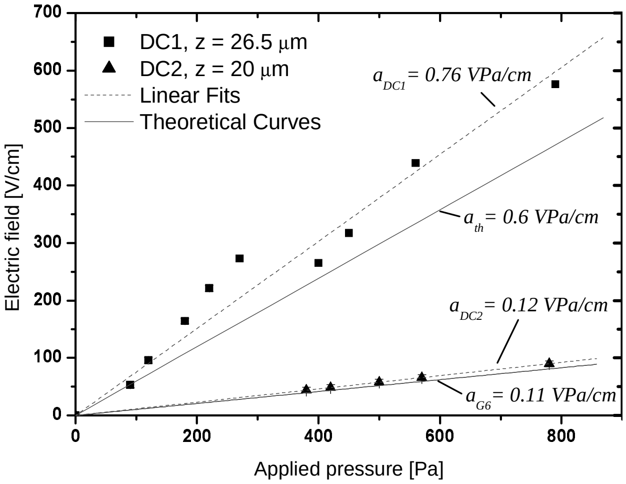

Δp **[Pa]**	**E$_{min}$ [V]**	**E$_{max}$ [V]**	**Ē [V]**
0	0	0	0
90	45	61	53
120	91	102	96
180	162	167	164
220	206	236	221
270	261	285	273

Figure 3.15
a) Operating E and Δp for which recirculating bead clusters were observed with DC1 and DC2. b) Table showing some maximum and minimum electric field values allowed for a given hydrostatic pressure to form recirculating bead cluster for DC1.

Two device layouts were used to verify Eq 3.25, DC1 and DC2. E was tuned with respect to a fixed Δp until recirculating bead clusters were observed at diverging and converging channel elements. 2-μm polystyrene beads ($\mu_{beads} \cong 4\text{x}10^{-4}$ cm^2/Vs) were used to perform the experiments. For each recirculating bead cluster formation, there is an upper and lower limit of the electric field (for a given pressure) for which the amplitude of bead clusters is maximum and minimum. This is shown in the table of Figure 3.15, which summarizes results obtained with DC1. The data obtained for DC1 show that the difference between E maximum (E$_{max}$) and minimum (E$_{min}$) amplitude of the recirculating beads, oscillates on average around 15 V/cm for a given Δp. However, the trend is that the larger the E, the larger the difference E_{max} -E_{min} becomes. The graph of Figure 3.15 illustrates the set of E and Δp for which recirculating bead clusters were obtained with the microfluidic devices DC1 and DC2. Linear fits have been included (dashed lines).

The graph of Figure 3.15 shows that the trend of the relation between E and Δp is linear, as predicted by Eq 3.25. The data of the plots give interesting information. First, it can be seen that the slope, $a_{DC1'}$, of the curve corresponding to DC1 is larger than a_{DC2}. The electric field necessary to create recirculating bead clusters for DC1 is on average 6 times higher than for DC2 for an equivalent Δp. Part of this difference is associated with the factor a. For the device DC1, a_{DC1} is about 4 times lower than a_{DC2}. The shallower and longer the channel, the lower the electric field required to generate recirculating bead clusters for a given pressure. The remaining difference between the slopes is associated with the difference between the μ_{EOF}: for the data obtained with DC2, μ_{EOF} was equal to 5.9 x 10^{-4} cm^2/Vs, while for DC1, μ_{EOF} = 5.6 x 10^{-4} cm^2/Vs. The value of the slopes found experimentally is very close to the theoretical slopes, a_{th}, calculated from Eq 3.25. Consequently, prediction of recirculating flows of beads can be estimated with Eq 3.25. On the other hand, once a E and a Δp is found for the formation of a fully developed recirculating flow of beads, whatever the type of beads, the buffer and the device employed, other sets of conditions can be extracted, since the relation between E and Δp is linear. This is an important point, since the determination of μ_{beads} is not obvious.

Eq 3.25 allows the average velocity of the buffer to be determined while beads are recirculating. In fact, although beads recirculate at the diverging and converging microchannel elements at a given E and Δp, does not necessary imply that the main stream is recirculating too. This is illustrated by the plots of Figure 3.16. A velocity presented in this figure refers to data obtained in Figure 3.15 for DC1, that is, when recirculating bead clusters were observed. Bead velocities of beads, estimated with Eq

3.25, are plotted as a function of *Δp* and compared with the velocity of the buffer calculated from Eq 3.25.

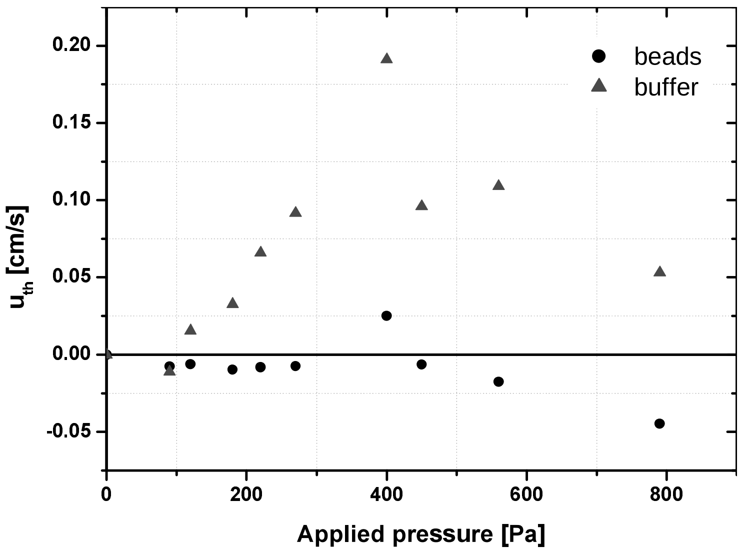

Figure 3.16
Theoretical velocity of the buffer and the recirculating beads. Between 90 and 600 Pa, $u_{beads} \cong 10^{-3}$ *cm/s on average, while* u_{ave} *of the buffer is about* 10^{-1} *cm/s on average.*

The data of Figure 3.16 shows that the beads have velocities < 0.01 cm/s on average. However, beads are driven by EOF only, for *E* ranging from 100 V/cm to 500 V/cm, their speed ≥ 0.01 cm/s. Comparison of bead and buffer velocity for the same set of *E* and *Δp* shows that the beads always have lower velocities than the surrounding buffer under conditions of recirculating flows. For instance, at *Δp* = 400 Pa and *E* = 265 V/cm, beads are recirculating at the diverging and converging elements with a average speed of about 0.01 cm/s, while buffer is driven by EOF at a speed of about 0.18 cm/s. This proves again that μ_{beads} plays an important role in the formation of recirculating bead clusters.

3.5 Examples of Recirculating Flow Control

In the next three sections, examples of the control of the recirculating flow of beads control are shown. These examples demonstrate the significant potential of this technology for bead handling in microdevices. This skill to manipulate precisely the beads is the key to the bead-based assay presented in Chapter 5.

3.5.1 Size and Velocity Distribution Control of Recirculating Flows

The clusters of freely moving beads formed at diverging and converging channel element can be described by the size, a, and velocity distribution of the recirculating flows at these locations. Tuning the potential at a given pressure allows the size and velocity distribution of the recirculating flows to be varied. Figure 3.17 shows an example for a diverging channel element of θ_{div} = 120°. Recirculating flows are confined to the vicinity of the entrance of the diverging element by applying an electric field of 230 V/cm at Δp = 0.7 kPa. Beads describe a rapid, circular trajectory from the core of the mouth of the diverging element towards the walls, giving rise to a sort of symmetrical vortex motion. In this case, the beads are caught in the recirculating flows and are confined to within an estimated distance, a_{beads}, of 25 µm from the mouth of the diffuser. The value a_{beads} can be considered as the amplitude of the bead cluster when recirculating at diverging or converging elements. Note that even if their amplitude is small and the space between them is reduced, beads generally do not stick to each other. A decrease of E from 230 V/cm to 190 V/cm results in an increase of a_{beads} from 25 µm to 90 µm. Consequently, video imaging shows that as the velocity of the beads drops, the space between them widens and they describe larger circular trajectories. As the picture of Figure 3.17 (b) shows, some beads manage to escape from the recirculating flow region toward the transition region.

Thus, experiments demonstrate that when the electric field is modulated, the amplitude and the speed of the bead recirculation is modulated too.

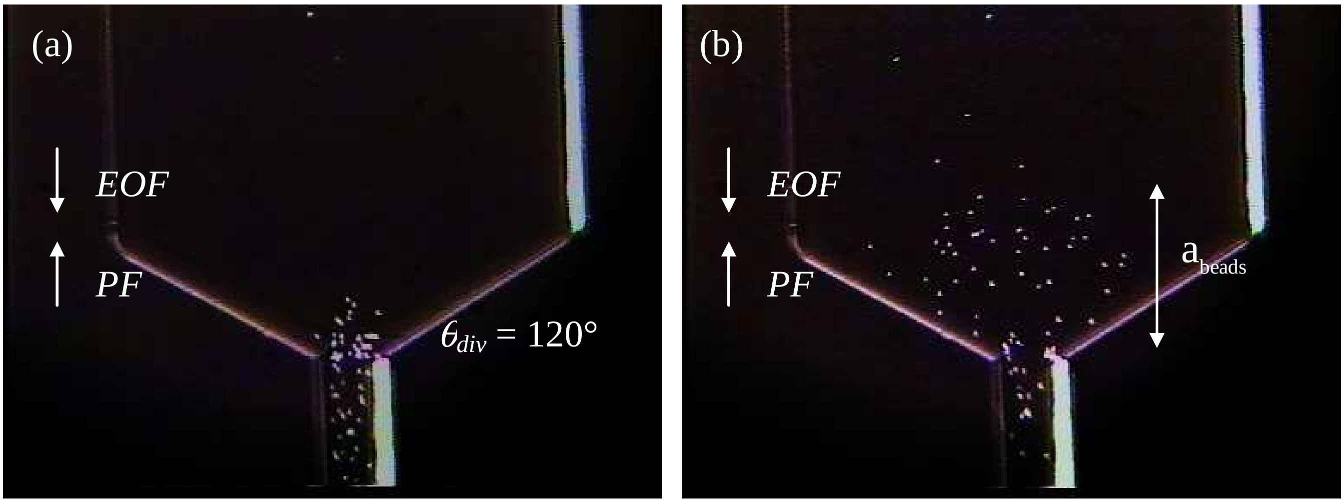

Figure 3.17
The size and velocity distribution of the recirculating flow patterns can be varied by simply tuning the applied potential at a given pressure or vice versa. In this case, E is varied at a constant Δp of 0.7 kPa. (a) E = 230 V/cm (b) 190 V/cm.

3.5.2 Controlled Movement of Bead Cluster

The six video frames in Figure 3.18 illustrate the controlled movement of clusters of 2.5-μm latex beads from one diverging element to the next in DC1. At t = 0 s, beads are recirculating at the first diverging channel. When the potential is turned off, the beads are transported towards the second diverging channel by hydrostatically induced pressure flow. At t = 6 and 12 s, the beads delineated the parabolic flow profile typical of Poiseuille flow, before passing through the 1st converging and the 2nd diverging microchannel element (34 s < t < 61 s). Velocity is higher at the core of the stream whereas close to the microchannel walls, the velocity is lower (slip condition). It should also be noted that the local concentration of beads plug changes as a function of time. When recirculating at the 1st diverging element at t = 0, the space between the beads seems to be reduced to a minimum. The concentration of beads in the diverging element is estimated from video imaging roughly to be 10^{11} beads/mL, whereas when the beads arrive at the 1st converging element (t = 34 s), the concentration reduces to roughly 10^{8} beads/mL. Once the beads have reached the 2nd diverging element, the potential is turned on again. Beads present in the transition region and flowing toward the 2nd converging element reverse direction instantaneously and are brought back to the 2nd diverging element. About 30 s is required for the beads to be recaptured in the recirculating flow patterns and the clusters to reform. Beads that were still located in the narrow channel separating the 1st converging and 2nd diverging channel element, will be immediately captured in a bi-directional flow and in recirculating flows at the converging and diverging microchannel elements. Thus, by simply turning off the electric field and hence removing the EOF component of the flow, the bead cluster can be transported as a plug to the next diverging channel. Once there, re-application of the electric field leads to the immediate re-establishment of rotating flows with consequent reformation of the clusters. This experiment illustrates a certain flexibility in bead handling which is not possible with more conventional microfluidic systems.

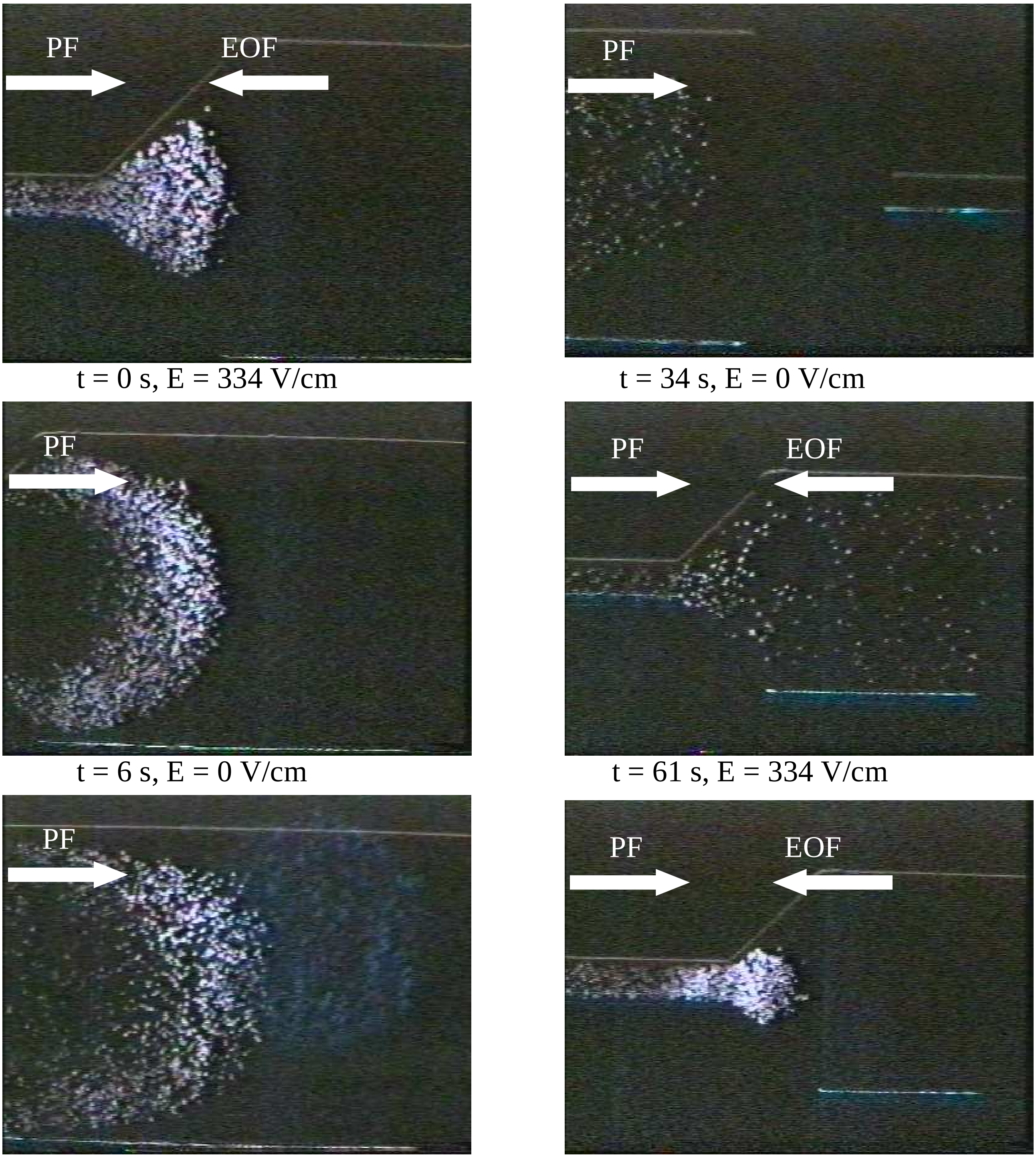

t = 0 s, E = 334 V/cm

t = 34 s, E = 0 V/cm

t = 6 s, E = 0 V/cm

t = 61 s, E = 334 V/cm

t = 12 s, E = 0 V/cm

t = 70 s, E = 334 V/cm

Figure 3.18

Experiments illustrating the controlled transport of 2.5-μm latex beads from one diverging channel to another in DC3. The applied pressure was 10 mbar throughout the experiment. Beads are sensitive to any modifications of the electric field or hydrostatic pressure. As soon as one of the two components, EOF or PF, is turned off, beads stop recirculating and start to flow in the device in the direction of the remaining component. When the electric field is turned on again, recirculating flows are instantaneously re-established (Video from A. Dodge).

3.5.3 Parallel Recirculating Flows and Influence of the Geometry

Experiments performed with diverging and converging channel elements, having the layout illustrated in Figure 3.19, show that recirculating flows of beads can be generated in parallel. This is an interesting capability that could be employed for high throughput screening, for instance. With these microfluidic devices, the effect of diverging microchannel element geometry on the recirculating flow of beads can also be observed. All the lengths and widths are the same for the segments of the microfluidic devices (see Figure 3.19). Only the opening angles are varied. Due to the configuration of the layout, boundary conditions are the same for both parallel diverging and converging microchannel elements.

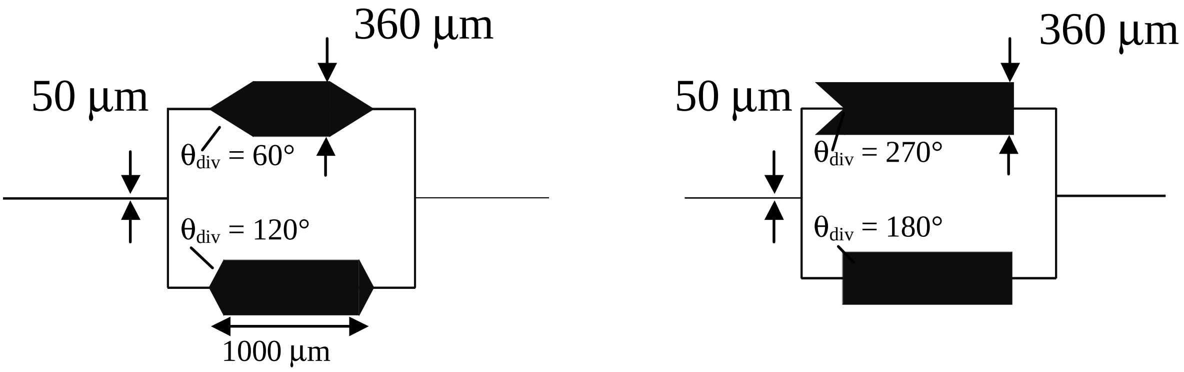

Figure 3.19
Layout of the microfluidic devices used for recirculating flow generation in parallel diverging elements having different geometries.

Figure 3.20 shows snapshots comparing the recirculating bead clusters that are formed upon addition of 1 µm Protein-A fluorescent beads to the system for four diverging microchannels with different θ_{div} when E = 425 V/cm and Δp = 4.2 kPa. Figure 20 *(a)* shows that for the same E and Δp, beads are confined in the recirculating flows for θ_{div} = 120° ($a_{120°} \cong$ 130 µm) while for θ_{div} = 60°, beads continue to progress into the wider segment. In Figure 20 *(b)*, $a_{270°} = a_{180°} \cong$ 130 µm. Video imaging shows also that recirculating bead velocities are higher for θ_{div} = 120°, 180° and 270° than for 60°. If E is increased by about 20 V/cm, beads will cease escaping the 60° diverging microchannel element. On the other hand, for the same increase of *E*, the amplitude of the recirculating bead cluster of the other diverging elements would be further reduced and bead velocities increased. Comparison of the four snapshots illustrates that the shape of the recirculating flows is also influenced by the geometry of the diverging element.

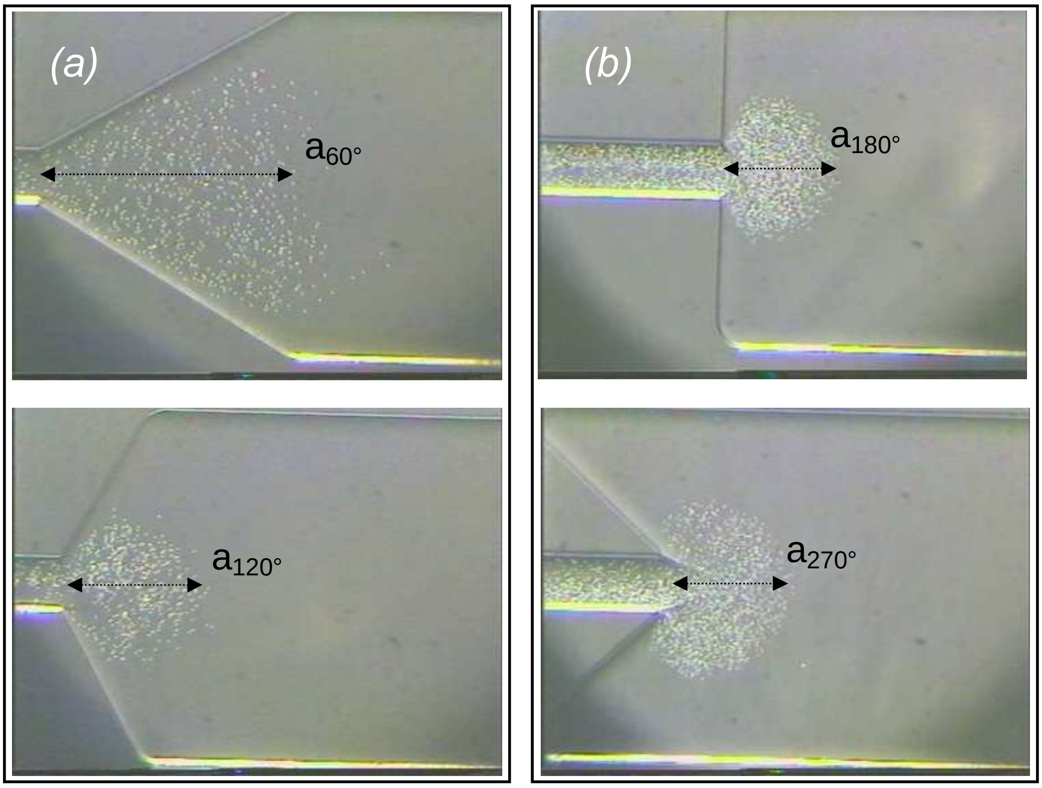

Figure 3.20
The amplitude of the recirculating beads, $a_{120°}$*, is estimated to be about 150* μ*m. Moreover,* $a_{120°}$ *remains stable: no beads escape from the diverging element, and the recirculating flow of beads is fully developed. For* θ_{div} *= 60°,* $a_{60°} \cong 280$ μ*m but continues gradually to increase: beads manage to escape from the recirculating zone to enter the wider segments.*

Hence, modulation of bead cluster size and shape can also be accomplished by controlling geometric and/or pumping parameters. On the other hand, beads provide useful and qualitative information on the velocity distribution, the size or amplitude of the recirculating flows, and the influence of the geometry on the shape of the recirculating flows.

Section 3.5.1, 3.5.2 and 3.5.3 demonstrated that beads can be captured in recirculating flow patterns at diverging and converging elements and can easily be transferred to other segments. Applications of this phenomenon will be discussed in Chapter 5.

3.6 Conclusion

This Chapter demonstrated that controlled, steady recirculating flows can be generated at Re << 1 in microfluidic devices featuring diverging and converging elements under conditions where EOF and PF are opposed. In the presence of a bi-directional flow, measurement made using the current monitoring method showed that the theoretical model introduced in section 3.2 for calculating the average linear velocity was accurate for microchannels of uniform cross-sections. This is no longer the case for devices with diverging and converging elements. In fact, it was demonstrated for these devices that the relationship between the EOF and the PF becomes non-linear as the average linear velocity approaches zero. This is due to energy losses induced by the generation of recirculating flows at the diverging and converging elements. These energy losses were associated with minor losses. Consequently, a theoretical model that takes into account EOF, PF and minor losses was developed and demonstrated to be in good agreement with experimental results obtained with the current monitoring method. The loss coefficient, used in this model to take into account minor losses, correlates the EOF, PF and the geometry of the device.

The recirculating flows, responsible for the minor losses were visualized with the help of negatively charged beads ranging from 1 μm to 6 μm. Visualisation of streamlines with beads proved to be a good means for providing information about the flow pattern when a bi-directional flow is present in the microfluidic devices. However, a substantial knowledge of the electrokinetic characteristics of the beads is necessary. It was observed that the beads used in this study behave like solid spherical charged particles characterized by an electrophoretic mobility. As a result, bead motion is distinct from the buffer flow. The apparent electrokinetic mobility of the beads was determined for a given buffer. Using the new theoretical model developed in section 3.4.1 and including the electrokinetic mobility of the beads, it was showed that bi-directional flow and recirculating flows are generated close to zero net flow. Visualisation of the streamlines with beads proved also to be a good substitute to the current monitoring method since the accuracy of latter is limited at zero net flow.

Last, it was observed that the recirculating flows of beads can be fully controlled by tuning the electric field for a given pressure, for example. Moreover, the beads can be totally confined in the recirculating flow patterns. This situation was called fully developed recirculating flows, characterized therefore by the confinement of the beads in the recirculating flow patterns and by a net flow determined by EOF. This phenomenon is the basis of the application introduced in Chapter 5 and Chapter 6.

3.7 References

[1] P. Gravesen, J. Branebjerg, and O. S. Jenson, "Microfluidics - A Review," *Journal of Micromechanics and Microengineering*, vol. 3, pp. 168-182, 1993.

[2] J. G. Santiago, "Electroosmotic flows in microchannels with finite inertial and pressure forces," *Analytical Chemistry*, vol. 73, pp. 2353-2365, 2001.

[3] W. Y. Lee and M. Wong, "Pressure loss in constriction microchannels," *Journal of Microelectromechanical Systems*, vol. 3, pp. 236-244, 2002.

[4] X. D. Li, W. Y. Lee, M. Wong, and Y. Zohar, "Gas flow in constriction microdevices," *Sensors and Actuators A*, vol. 83, pp. 277-283, 2000.

[5] C. L. Rice and R. Whitehead, "Electrokinetic flow in a narrow cylindrical capillary," *Journal of Physical Chemistry*, vol. 69, pp. 4017-4024, 1965.

[6] R. Datta and V. R. Kotamarthi, "Electrokinetic dispersion in capillary electrophoresis," *AIChE J*, vol. 36, pp. 916-26, 1990.

[7] H. Li and R. J. Gale, "Hydraulic and electroosmotic flow through silica capillaries," *Langmuir*, vol. 9, pp. 1150-1155, 1993.

[8] F. M. White, *Fluid Mechanics*, 4th ed. New York: McGraw-Hill, 1999.

[9] M. C. Potter and D. C. Wiggert, *Mechanics of Fluids*, 1997.

[10] R. S. Martin, A. J. Gawron, S. M. Lunte, and C. S. Henry, "Dual-electrode electrochemical detection for poly(dimethylsiloxane)-fabricated capillary electrophoresis microchips," *Analytical Chemistry*, vol. 72, pp. 3196-3202, 2000.

[11] Y. Walbroehl and J. W. Jorgenson, "Capillary zone electrophoresis for the determination of electrophoretic mobilities and diffusion coefficients of proteins," *Journal of Microcolumn Separations*, vol. 1, pp. 41-45, 1989.

[12] X. H. Huang, M. J. Gordon, and R. N. Zare, "Current-monitoring method for measuring the electroosmotic flow rate in capillary zone electrophoresis," *Analytical Chemistry*, vol. 60, pp. 1837-1838, 1988.

[13] L. E. Locascio, C. E. Perso, and C. S. Lee, "Measurement of electroosmotic flow in plastic imprinted microfluid devices and the effect of protein adsorption on flow rate," *Journal of Chromatography*, vol. 857, pp. 275-284, 1999.

[14] S. L. R. Barker, M. J. Tarlov, H. Canavan, J. J. Hickman, and L. E. Locascio, "Plastic microfluidic devices modified with polyelectrolyte multilayers," *Analytical Chemistry*, vol. 72, pp. 4899-4903, 2000.

[15] S. C. Wang, C. E. Perso, and M. D. Morris, "Effects of alkaline hydrolysis and dynamic coating on the electroosmotic flow in polymeric microfabricated channels," *Analytical Chemistry*, vol. 72, pp. 1704-1706, 2000.

[16] W. Thormann, C. X. Zhang, J. Caslavska, P. Gebauer, and R. A. Mosher, "Modeling of the impact of ionic strength on the electroosmotic flow in capillary electrophoresis with uniform and discontinuous buffer systems," *Analytical Chemistry*, vol. 70, pp. 549-562, 1998.

[17] R. L. Chien and D. S. Burgi, "On-column sample concentration using field amplification in CZE," *Analytical Chemistry*, vol. 64, pp. A489-A496, 1992.

[18] R. L. Chien and J. C. Helmer, "Electroosmotic properties and peak broadening in field- amplified capillary electrophoresis," *Analytical Chemistry*, vol. 63, pp. 1354-1361, 1991.

[19] J. L. Pittman, C. S. Henry, and S. D. Gilman, "Experimental studies of electroosmotic flow dynamics in microfabricated devices during current monitoring experiments," *Anal. Chem.*, vol. 75, pp. 362-370, 2003.

[20] A. Dodge, K. Fluri, E. Verpoorte, and N. F. de Rooij, "Electrokinetically driven microfluidic chips with surface modified chambers for heterogeneous immunoassays," *Analytical Chemistry*, vol. 73, pp. 3400-3409, 2001.

[21] J. N. Pfahler, "Thesis: Luiquid transport in micron and submicron size channels," in *Mechanical Engineering and Applied Mechanics*. Pennsylvania: University of Pennsylvania, 1992.

[22] J. G. Santiago, S. T. Wereley, C. D. Meinhart, D. J. Beebe, and R. J. Adrian, "A particle image velocimetry system for microfluidics," *Experiments in Fluids*, vol. 25, pp. 316-319, 1998.

[23] S. P. Radko and A. Chrambach, "Separation and characterization of sub-μm- and μm-sized particles by capillary zone electrophoresis," *Electrophoresis*, vol. 23, pp. 1957-1972, 2002.

4 Numerical Analysis of On-Chip Recirculating Flows

4.1 Introduction

Electrokinetic microfluidic microsystems are powerful analytical tools for applications such as DNA analysis, enzyme assays and immunoassays. The basic operations in these systems are sample injection, mixing, chemical reaction, separation and detection. A complex relationship exists between the microchannel geometries and the behaviour of the component fluids transported in these channels. Computer-assisted design (CAD) tools can be a valuable aid in the design of microfluidic systems. They can help researchers to avoid costly mistakes in chip design [1, 2]. Simulations of electrokinetic flows have been reported in the literature for both electrophoretic and electro-osmotic flows [3-6] [1, 2, 7] as well as for PF in diffuser and nozzle microchannel elements [8].

Computational fluid dynamics (CFD) has as its objective the numerical solution of fluid-flow equations. The calculus problem of solving a coupled system of non-linear partial differential equations for the variables of interest (e.g., velocity, pressure, and temperature) is transformed into an algebra problem of solving a large system of simultaneous linear equations for discrete unknowns that represent the state of a thermal-fluidic system. The latter is amenable to numerical solution on a computer [9]. This is the basic concept of the finite element method (FEM). The practice of CFD began with the advent of computers; indeed, the first computer was developed, in part, to solve fluid-flow equations (ENIAC). Initially, most numerical solutions were limited to flows that could be approximated as spatially one-or two dimensional. The time required to perform three-dimensional (3-D) calculations remained prohibitive even if most real flows are 3-D. With the advent of more powerful computers over the last 15 years, 3-D flow CFD calculations have become more common. On the other hand, improvement of numerical methods has helped to the development of CFD tools for 3-D flow problems. Improvement of finite-element methods that better accommodate the complex geometrical boundaries that characterize flows, have enabled 3-D CFD for microfluidic problems.

In this work, the modelling of electrokinetic and hydrodynamic transport-based microsystems are performed with FlumeCAD (Coventorware). FlumeCAD is an integrated design environment consisting of 3-D design, modelling and simulation software tools. The process to perform the simulation of a microfluidic device is briefly introduced in the next section.

Simulations of bi-directional flow in microchannels of uniform and non-uniform cross-section are introduced in sections 4.3 and 4.4, respectively. A calibration of the simulations is performed for both types of microchannels, using the experimental results obtained with the current monitoring method presented in Chapter 3. Results of simulations of the bi-directional flow in microchannels of uniform cross-section are discussed in section 4.3.2. In section 4.4.2, it is demonstrated using FlumeCAD that recirculating flows are generated at diverging and converging elements when EOF and PF are opposed, supporting the flow visualisation with beads reported in Chapter 3. It is also shown that the beads used in Chapter 3 delineate the same streamlines simulated with FlumeCAD. Moreover, simulation tool allows 3-D viewing of the recirculating flows (4.4.2.2). It also helps to understand the mechanisms of the recirculating flows (4.4.2.3 and 4.4.2.4) and, consequently, to predict the recirculatng flows. In section 4.5, examples of simulated recirculating-flow control are reported, illustrating that the simulation tool makes it possible to take into account both the influence of micro-diffuser-like channel geometry and different mechanisms of fluid transport. Simulations can then be used to predict the strength and the size of recirculating flows for the different diverging and converging microchannel elements. In section 4.6, simulations of a buffer having the electrokinetic properties of the beads used in Chapter 3 are reported. It is shown that prediction of bead clusters and bead motion is possible, if their electrokinetic mobility is known.

4.2 FlumeCAD

In this section a CFD tool, FlumeCAD (Coventorware, MA, USA), tool is introduced. The process to perform simulations with FlumeCAD is briefly introduced. Commonly used to optimise microfluidic systems, FlumeCAD is used in this work to support experimental observations. Netflow, a solver of FlumeCAD that solves the full Navier-Stokes equations, is used to prove that recirculating flows are formed at low Reynolds numbers as observed in Chapter 3.

4.2.1 Simulation Process with FlumeCAD

Modeling of microfluidic devices with FlumeCAD is divided into 3 main steps: device design, modelling and simulation with a specific module. The process to perform the simulation of a microfluidic device is illustrated in Figure 4.1.

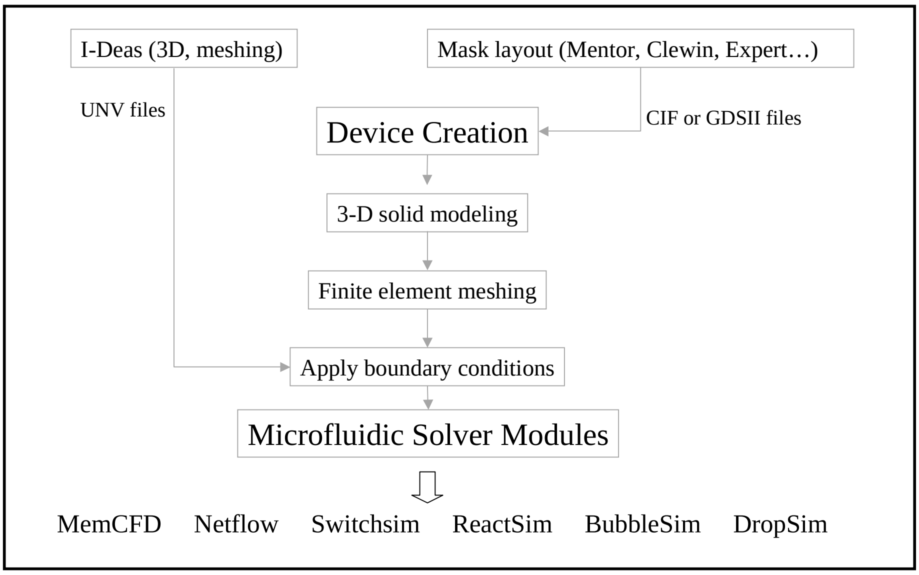

Figure 4.1
Schematic of the simulation steps with FlumeCAD and its different solvers.

4.2.1.1 Device Creation

The first step prior to the modeling of a microfluidic system consists of designing the device. Solvers of FlumeCAD, based on FEM, require that devices are designed in 3-D. FlumeCAD offers basically three possibilities:

1. The first possibility is to use *Catapult*, a 2-D layout editor supplied with FlumeCAD similar to standard mask layout editors like Clewin or Expert. Once the layout is designed, the software renders it in 3-D, with a module named *Membuilder*, in order to be compatible with the solvers. However, this module is not able to automatically create the 90°-rotated-D-shaped cross-sections produced by isotropic etching of Pyrex with hydrofluoric acid. This is the main disadvantage of *Catapult*. On the other hand, the main advantage of *Catapult* is that mask layouts created with other mask layout editors can directly be imported. The only constraint is that the formats have to be either .CIF or .GDSII.
2. Another possibility to design microfluidic devices in 3-D is to use pre-meshed fluidic components provided in a standard library (*Mesh Generator*) with FlumeCAD. In this case, the 90°-rotated-D-shaped cross-sections is available, as are the rectangular and triangular cross-sections. However, the user is limited by the library. For example, diverging and converging microchannel components are not available in version 2001.3 of *Coventor*.
3. The last possibility is to use *I-DEAS,* a CAD tool provided by EDS (Switzerland) compatible with *Coventor*, (but not supplied with Coventor). With *I-DEAS* the device is directly designed in 3-D (UNV files). For instance, diverging and converging elements can be designed with the 90°-rotated-D-shaped cross-sections. In this work, all the modeled microfluidic devices are designed with *I-DEAS*.

4.2.1.2 Grid Generation for FE analysis

The next step in the design step is the meshing (Figure 4.2). This step prepares the device for the finite element analysis. The idea is to divide the system into a number of smaller elements connected together by nodes. Each node is associated with a differential equation that is solved numerically. This is the most important step. The meshing has to be accurately chosen in order that solvers converge to a solution, while at the same time calculation times are reduced. Therefore, in finite element analysis, it is suitable to reduce the device to sub-devices and therefore, to decompose the simulation of the system.

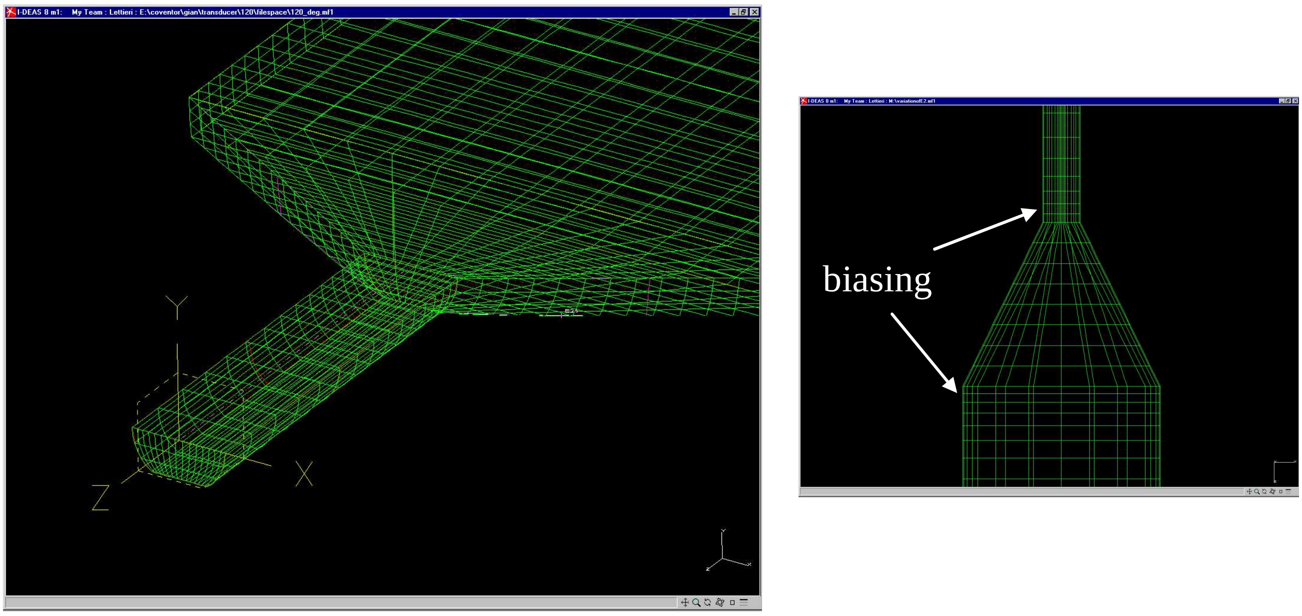

Figure 4.2
Details of the diverging/converging element meshed and designed with I-DEAS. Local mesh refinement (biasing) is used in the regions where the geometry gradually changes

4.2.1.3 Netflow: Microfluidic Solver Module

FlumeCAD has several 3-D finite element-based solvers (MemCFD, Netflow, etc…) as shown in Figure. Netflow can be applied to model PF, EOF, diffusion and electrophoresis, either individually or in combination. In this work, the Netflow module is used to simulate bi-directional flow generated by opposing EOF to PF in microfluidic systems. The equations used to model the flow are the Navier-Stokes equations, coupled with the mass equation for the species motion and the Poisson equation for the electric field:

$$\frac{D(\rho\mu E)}{Dt} = -\nabla p + \nabla \cdot \eta \nabla \mu E + \rho_e E \qquad \text{Navier-Stokes equation}$$

$$\nabla^2 = \frac{2n_0 ze}{\varepsilon\varepsilon_0} \sinh\left(\frac{ze}{k_B T} \zeta \right) \qquad \text{Poisson-Boltzmann}$$

$$\frac{\partial c_i}{\partial t} + \mu E \nabla c_i = D \nabla^2 c_i \qquad \text{Species mass equation}$$

EOF is modelled through the specification of the μ_{EOF} coefficient for the walls. For more details on these equations, please refer to the manual supplied with FlumeCAD.

The simulations were done using a Dell computer (Dell Precision 410, PIII). All the simulations were performed using 3-D dimensional models (3-D simulations). The number of elements for the grid meshing never exceeded 4000. For substructures up to 9000 μm long and 25 μm deep, with and without diverging/converging elements, no differences in solutions were observed between 1000 elements and 3000 elements. The longest structure simulated was 33 mm long (27 μm deep) and required 3700 elements. No problems with respect to solver convergence were observed. The input solver parameters used in the simulations are summarized in Table 4.1.

Input Parameters	Value
Density [kg/m^3]	1000
Thermal Conductivity [W/mK]	0.585
Specific Heat [J/kgK]	4.18x10^3
Viscosity [Pa·s]	0.001
Potential [V]	variable
Applied Pressure [Pa]	variable
Mobility ($\mu = \mu_{EOF}$-μ_{beads}) [cm^2/Vs]	variable

Table 4.1
Material properties of the buffer and variable parameter inputs required by the solver.

4.3 Simulation Results for Uniform Microchannels

In its application to practical design problems, CAD tools require knowledge of material and physical parameters that are generally not known [10]. In this work, EOF is opposed to PF in microchannels either with a uniform cross-sectional area or with non-uniform cross-section. The simulation in microchannels of EOF or PF individually can be very accurate if material properties are well known [μ_{EOF}, dynamic viscosity etc...]. However, bi-directional flow in special geometries is less standard and experimental data have to be considered in conjunction with simulations. The idea is to extract experimental information like the electric field (E_{exp}) and the applied pressure (Δp_{exp}) for cases where bi-directional flow is generated in microchannels of both uniform and non-uniform cross-section, in order to adequately replicate the experiment with FlumeCAD. It is a sort of calibration of the simulations allowing the electric field (E_{sim}) and the applied pressure (Δp_{sim}) values for the simulations corresponding to E_{exp} and Δp_{exp} to be found ($E_{sim} = \gamma_{\mathrm{E}} E_{exp}$, $\Delta p_{sim} = \gamma_{\Delta \mathrm{p}} \Delta p_{exp}$ where γ_{E} and $\gamma_{\Delta \mathrm{p}}$ are the conversion factors extracted from the experiments). FlumeCAD allows the flow rate across these systems to be calculated while experiments performed with the current monitoring method yield an estimation of the average linear velocity. To calibrate simulations with experimental data, the experimental and theoretical flow rate values (Q_{mea} and Q_{sim}, respectively) were compared.

4.3.1 Calibration of Simulations using Experimental Data

Figure 4.3 compares the Q_{mea} with the simulated value, Q_{sim}, for G7, a straight microchannel of uniform cross-section, as a function of the applied pressure. The experimental parameters required by the solver to perform this simulation are summarized in Table 4.1. The layout and the dimensions of G7 are reported in

Chapter 2. The data of were obtained for 10 mM sodium tetraborate buffer (pH = 9, μ_{EOF} = 5.45 x 10^{-4} cm^2/Vs) at $E_{exp} = E_{sim}$ = 150 V/cm. Q_{mea} is used as a reference.

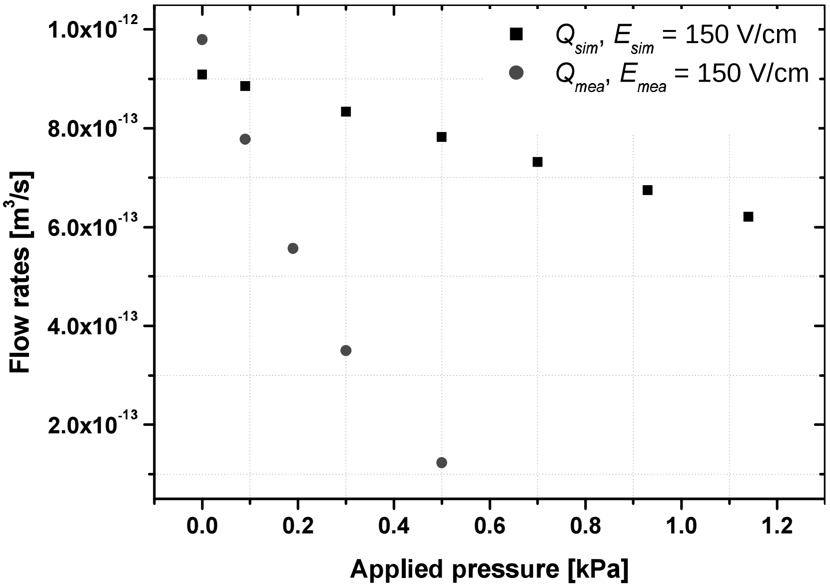

Figure 4.3

Theoretical (•) and simulated flow rate (■), for $E_{exp} = E_{sim}$ *= 150 V/cm, as a function of the applied pressure. The microfluidic device G7 (*A_1 *= 1.48 x* 10^{-9} m^2*) was used to calculate* Q_{th} *and* Q_{sim}*.*

Considering the data of Figure 4.3, the slope of the curve corresponding to Q_{mea} is about 6.8 times higher than the slope of Q_{sim}. This means that, without correcting simulation parameters, fully developed bi-directional flow (Q = 0) is expected at about 3.7 kPa instead of 0.54 kPa. This result is supported by two similar comparisons with the same device but for E_{exp} = 300 V/cm and 600 V/cm. This difference between theory and simulation can come from different causes. For instance, the meshing of the 3-D solid model used for the simulation is not optimised. The number of meshed elements is 3800 in this case. However, simulations performed with finer meshing (6000 elements) did not show any relevant improvement, considering that calculation time was longer because of the large number of meshing elements. Another possible factor is the length of the 3 D model which is equal to 3.3 cm. It had not been verified if simulations were more accurate with shorter modelled devices. However, as discussed in the introduction, simulations need experimental results or parameters to yield results which are closer to the reality. It must be kept in mind that simulations can not exactly reflect experiments. On the other hand, in the absence of counter pressure and when flow is induced by electro-osmosis, the relative error between E_{sim} and E_{mea} is on average 2 % (this value is higher than those obtained for microchannels with rectangular cross-sections, for example). Thus, for the remaining sections, it is assumed that $\Delta p_{sim} = \gamma_{\Delta p}\Delta p_{exp} = \Delta p$ where $\gamma_{\Delta p} = 0.15$ and $E_{sim} = E_{mea} = E$. This statement is only valid for DC1 and for a given μ_{EOF}.

4.3.2 Simulation of the Bi-directional Flow

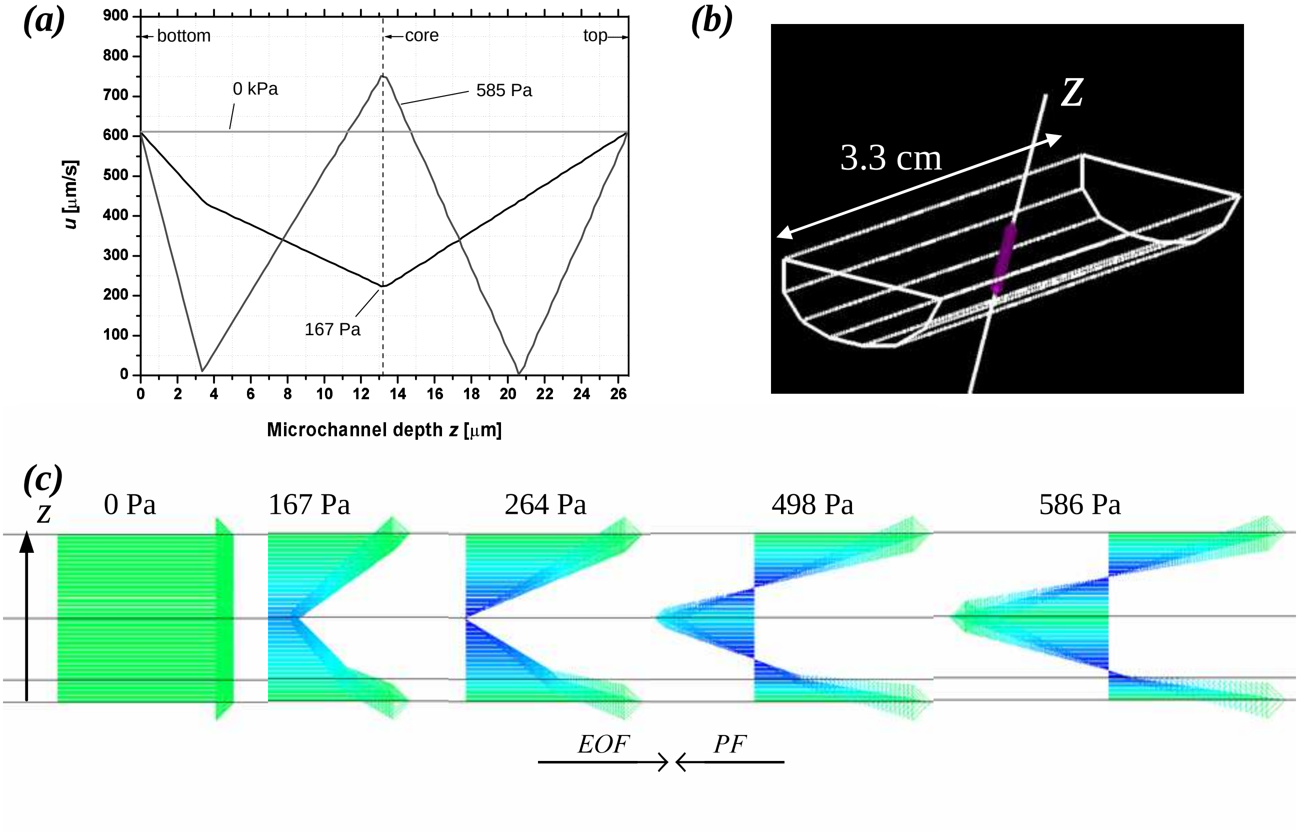

Figure 4.4
Simulations of the bi-directional flow in G7. (a) Velocity magnitude as a function of the microchannel depth. The bottom, the core and the top of the microchannel are indicated. The velocity distribution is not symmetric from the bottom of the microchannel to the top. (b) Sketch of the modelled device G7 showing the z-axis.(c) Evolution of the velocity vectors, across G7, as a function of the counter pressure.

Simulations of the velocity magnitude and the velocity vector field of the flow as a function of the depth across the microchannel G7 are reported in Figure 4.4. EOF is opposed to PF, and *E* is fixed at 150 V/cm while Δp ranges from 0 Pa to 1 kPa. As expected, the velocity induced by EOF at 0 Pa is constant across the microchannel. As the counter pressure increases, the velocity decreases around the core of the microchannel until reaching zero at 264 Pa (Figure *(c)*). Then, flow becomes gradually bi-directional. Bi-directional flow is almost fully developed at 498 Pa. In fact, velocity magnitudes induced by EOF at the microchannel top wall and bottom wall are almost the same as velocity magnitude induced by PF around the core. Zero net flow occurs at about 540 Pa. It should be noted in this case that the profile of the flow is not symmetrical with resppect to the core of the microchannel. This is due to the 90°-rotated-D-shaped cross-sections. In comparison, the simulation of the velocity magnitude distribution is symmetrical around the core for a device with a rectangular cross-section (data not shown).

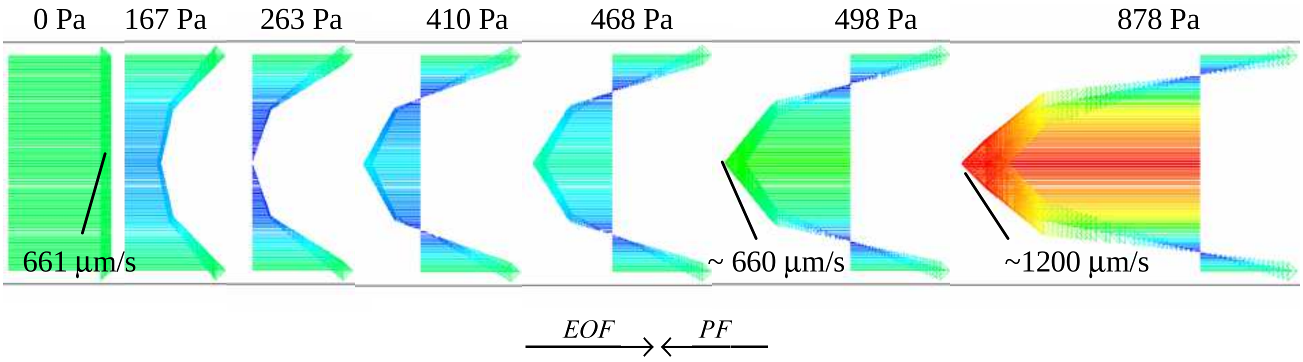

Figure 4.5
Top view of the simulation of the velocity vector field of the flow (µm/s) for E = 150 V/cm. The vectors are located in the middle of the microchannel. The flow becomes bi-directional because of the application of a counter PF.

Figure 4.5 illustrates the evolution of the velocity vector field of the flow as a function of the applied counter pressure at *E* = 150 V/cm. Vectors are located in the middle of the microchannel G7 and they are viewed from the top.Note that the profile of the flow is symmetric in this plane. Around 498 Pa, the bi-directional flow is almost fully developed.

4.4 Simulation Results for Microchannels with Divergent and Convergent Elements

As in the previous section, the modelling of device DC1, which features 2 diverging and 2 converging microchannels elements (see Chapter 2 for dimensions), requires experimental data to adjust the E_{sim} and Δp_{sim} with experimental values. Once the simulations are calibrated with the experimental results, the modelling of the buffer flow and / or bead flow under conditions where EOF and PF are opposed can be achieved. However, the determination of Q_{mea} is not as obvious as in the previous section since the cross-section is not constant in this case. To compare Q_{mea} and Q_{sim}, we assume that $Q_{mea} = \Gamma \Delta t$, where Γ is the total volume of DC1 ($\cong$ 100 nL) and Δt is the time obtained with the current monitoring method (see section 3.3.1, Chapter 3).

4.4.1 Calibration of Simulations with Experiments for DC1

The numerical calculation of the average flow rates, Q_{sim}, and the measured flow rates, Q_{mea}, are reported as a function of Δp at different E values in Figure 4.6.

When the flow rate is due only to the EOF or PF, the solver was in agreement with experimental results for microchannels of uniform cross-section. This is no longer the case when the device features diverging and converging microchannel elements. This can be seen at $\Delta p_{sim} = \Delta p_{mea} = 0$ in the graphs shown in Fig. 4.6(a). The numerical calculation of the average flow rates, Q_{sim}, and the measured flow rates Q_{mea} are reported as a function of Δp at different E values in this figure.

In Figure 4.6 (a), Q_{sim} is about 1.4-fold lower than Q_{mea} when the applied pressure is zero for each measurement. This also has to be considered in order to adjust the solver operating parameters. This difference between Q_{sim} and Q_{mea} was also reported by

Zang et al. [11] and other studies [4],[7]. In their study, Zang et al., showed that when a fluid pumped by EOF experiences a sudden contraction and expansion at the microchannels inlet and the microchannel outlet, an unrecoverable energy loss results. They demonstrated that EOF induces a pressure gradient at the entrance/exit of the microchannels leading to mismatch between simulation and experiment. In the case presented here, the difference between Q_{sim} and Q_{mea} when only EOF is present, may also be due to pressure gradient induced by the presence of converging and diverging elements present in the fluid stream. Figure 4.7(a) shows the velocity flow profile when only PF is present in DC1 whereas Figure 4.7(b) shows the case when only the EOF is present. In the case of the latter, the profile is no longer flat, as was the case in G7 (see Figure 4.7). Simulations indicate therefore that diverging and converging elements can induce a pressure drop of the EOF. This effect, shown in Figure 4.7, was not studied in detail.

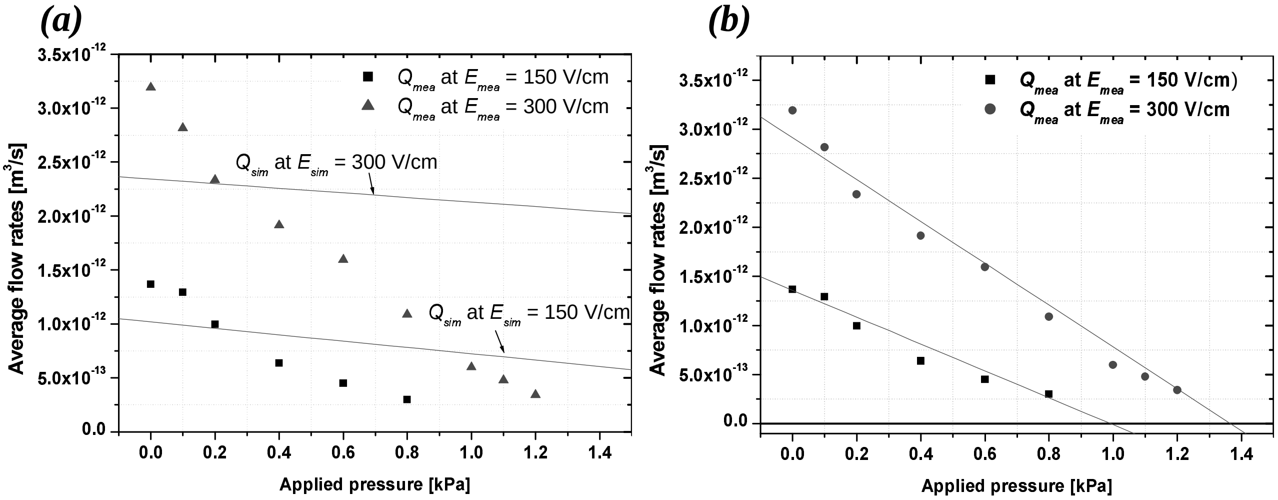

Figure 4.6

Average flow rates as a function of Δp for different E.(a) Comparison between the simulated flow rates (solid curves) and the measured flow rates for DC1. (b) Corrected Q_{sim} (solid curves) using experimental results.

It was observed that the adjustments of Δp_{sim} are different from one set of experimental data to the other. The numerical calculation of Q_{sim} at E_{sim} = 150 V/cm and 300 V/cm requires that the Δp_{mea} values have to be multiplied by 0.2 and 0.1, respectively, in order to make sure that $Q_{sim} = Q_{mea}$. Thus, the new set of boundary conditions at the entrance and exit of DC1, for having $E_{sim} = E_{mea} = E$ and $\Delta p_{sim} = \Delta p_{mea} = \Delta p$, requires that $\gamma_E = 0.7$, and $\gamma_{\Delta p} = 0.2$ at 150 V/cm and $\gamma_{\Delta p} = 0.1$ at 300 V/cm. The modifications performed on the simulations can be seen in Figure 4.6 *(b)*. The numerical calculation of the average flow rates, Q_{sim}, and the measured flow rates Q_{mea} are reported as a function of Δp at different E values in this Figure.

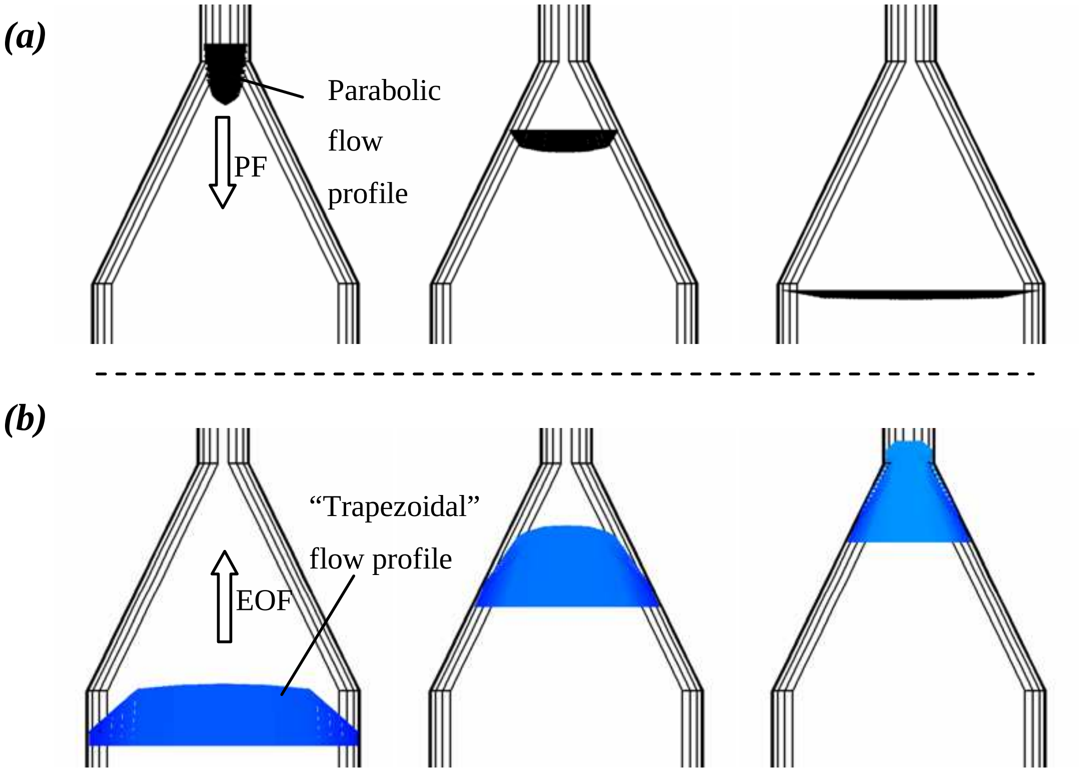

Figure 4.7
Simulation of the velocity vector field of the flow in DC1 (2^{nd} diverging element). (a) Unidirectional flow induced by PF at Δp = 1 kPa (E = 0 V/cm).(b) Flow induced by electro-osmosis without counter pressure at E = 150 V/cm. Note that no flow recirculation is observed in both cases.

4.4.2 Simulation of Recirculating Flows

Once calibrated, simulation tools can be used to visualize the streamlines produced by the recirculating flows, to visualize the flow pattern in 3 dimensions and to help to predict and to understand the mechanisms of this phenomenon. These topics are discussed in the next sections.

4.4.2.1 Visualisation of Recirculating Flows in DC1

Simulations of the streamlines in DC1 indicate that as the flow rate approaches zero, PF entering a diverging channel slows down, divides and is deflected to the sides to give rise to a flow pattern similar to a pair of vortices (Figure 4.8). The situation at a converging channel element is reversed, with PF inducing an adverse pressure gradient to EOF. Flow separates from the walls as a result, creating steady recirculating motions similar to that at a diverging channel. This is illustrated by the vector plots of the simulated velocity profiles at the diverging and converging elements for DC1 shown in Figure 4.8. Boundary conditions are similar to the experiments and are set so that the flow rate is close to zero. The 3-D model of DC1 was reduced to a substructure with the aim to obtain more detailed information about flow patterns at convergent and divergent elements while keeping the same number of meshed elements (= 3400). The flow rate is about 0.2 pL/s if no EOF is present. Under these conditions, simulations and experiments performed with beads in Chapter 3 demonstrate that no flow recirculation is generated (see Figure 4.7). The same is true if only EOF is used to pump the flow or the beads.

As observed with beads in Chapter 3, the simulations confirm that recirculating flows are generated simultaneously at each diverging and converging microchannel element. Bi-directional flow is also present in all the narrow segments of the device. Simulations also confirm that the net flow is still determinated by EOF when fully developed recirculating flow of beads was observed. In this case, EOF is predominant along the walls in narrow segments and all over the wider segments (the transition regions) located after the second diverging element and before the first converging element. In the narrow channel, the flow is bi-directional. On the other hand, the recirculating flows are also observed when EOF does not determine the net flow rate.

In this case, in the transition region before the first diverging element, EOF is predominant at the walls while flow is driven by PF around the core.

In chapter 3, visualisation of the streamlines with beads showed that recirculating flows were generated as the average flow rate approaches zero. The results obtained with the simulations confirm this phenomenon.

E [V/cm]	**150**	**300**
∆p [Pa], first recirculating flows	*90*	*100*
∆p [Pa], fully developed recirculating flows (Q = 0)	*1000*	*1380*

Table 4.2
Corrected simulated data comparing the Δp *for which recirculating flows starts* ($Q \neq 0$) *and are fully developed* ($Q = 0$) *in DC1. Recirculating flows are already observed at* $\Delta p \cong 100$ *Pa which corresponds to a height difference between the reservoirs of about 1 cm.*

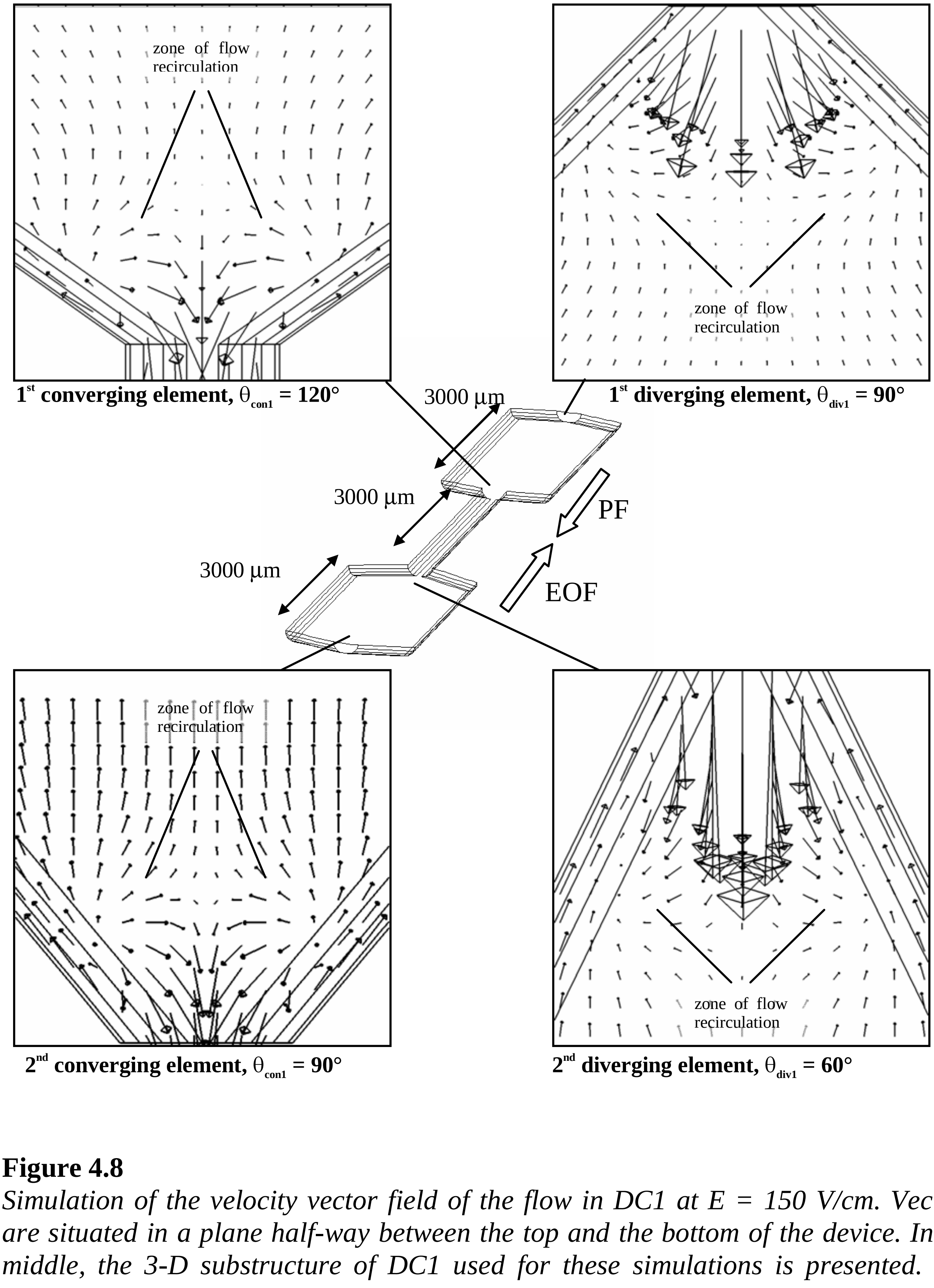

Figure 4.8
Simulation of the velocity vector field of the flow in DC1 at E = 150 V/cm. Vectors are situated in a plane half-way between the top and the bottom of the device. In the middle, the 3-D substructure of DC1 used for these simulations is presented. The Δp_{sim} *used for the simulation with the substructure was obtained from the simulation of the whole structure, including in-and outlet microchannels not shown here, for* E_{sim} *= 150 V/cm and* Δp_{sim} *= 1 kPa.*

Once the simulations were calibrated, simulations showed that recirculating flows were generated at $Q = 0$ and, furthermore, that they were already present beyond the zero net flow. Table 4.2 shows the Δp at which the first simulated recirculating flows are observed in DC1, and at which the simulated fully developed recirculating flows are observed at 150 V/cm and 300 V/cm.

4.4.2.2 3-D Simulation of Recirculating Flows

Three-dimensional simulations reveal that convective movement of the flow occurs at the diverging and the converging elements. This is illustrated in Figure 4.9. The simulated velocity vectors are viewed from the side. These simulations point out that when the PF enters the diverging elements, it drops towards the bottom of the device where EOF is predominant. Thus, a recirculating flow from the core towards the bottom of the device is also observed at the diverging elements. At the converging elements, the situation is reversed. The EOF is strongly deflected from the bottom of the device towards the core where PF is predominant. This movement in the third dimension as pointed out by simulations could not be verified with the help of beads using our optical setup. To visualize this effect, a confocal fluorescent microscope would be required. The presence of induced planar recirculating flows in addition to 3-D recirculation of the flow helps to characterize the “virtual” flow barriers which help to prevent beads from escaping the diverging and the converging microchannel elements when recirculating flows are fully developed (see Chapter 5).

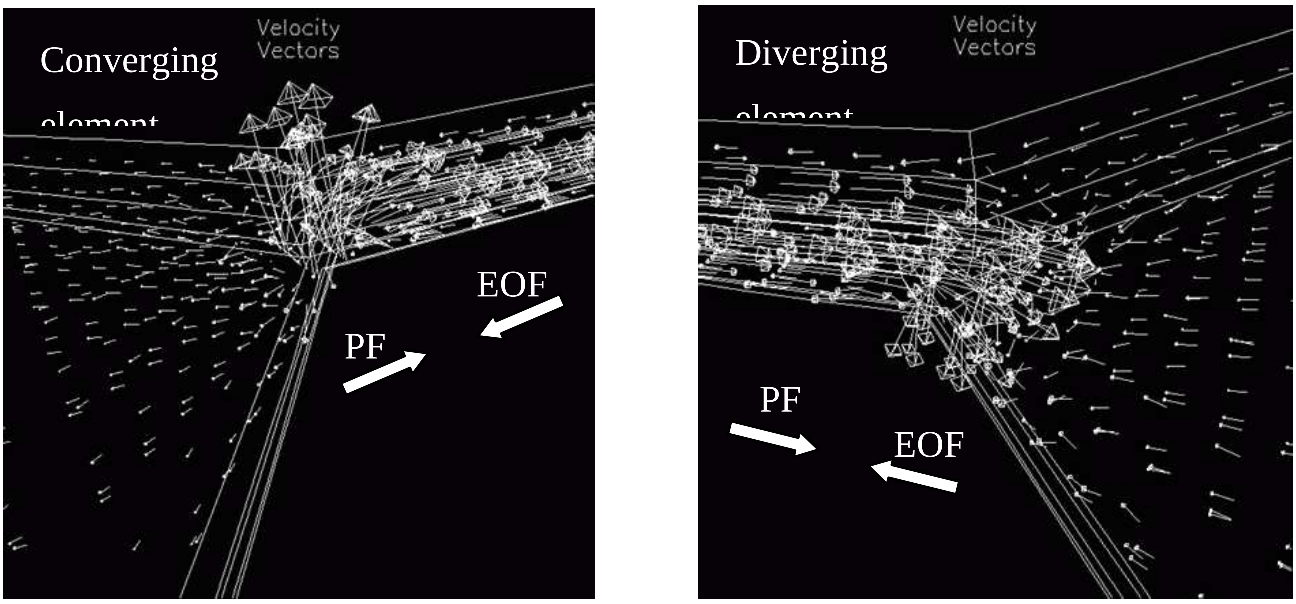

Figure 4.9
Simulation of the velocity vector field of the flow of diverging (right-hand side) and converging elements (left-hand side). Simulations help to visualize the virtual flow barriers artificially induced by opposing the PF and the EOF at these elements.

4.4.2.3 Distribution of the Velocity across the Device

The simulation of the bi-directional flow in the narrow channel at a converging element is illustrated in Figure 4.10 *(a)*. This simulation shows the different “layers” of velocity in the narrow segments due to the bi-directional flow. Figure 4.10 *(b)* gives an idea of the velocity distribution in DC1 when recirculating flows are fully developed. The differences between the velocity magnitude in the narrow segments, where a bi-directional flow is present, and the wide segments, where EOF dominates, can be observed.

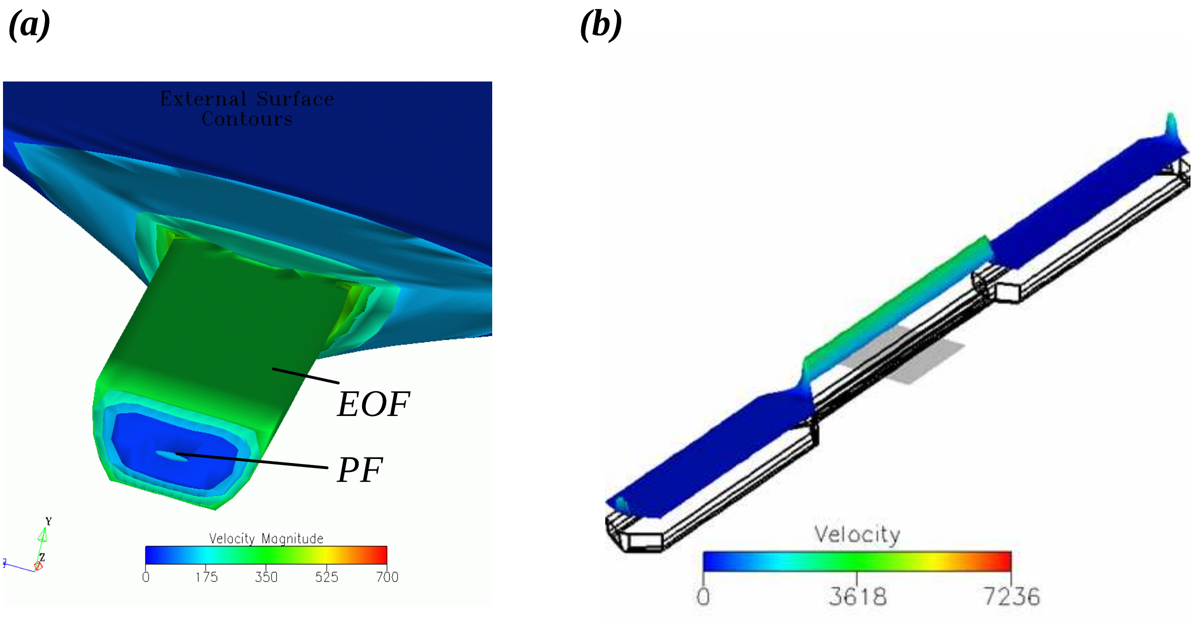

Figure 4.10
a) Details of a simulation showing the different layers of velocity when bi-directional flow is established. Close to the walls of the narrower microchannel, velocity is higher than in the centre. b) Simulation of the velocity magnitude (µm/s) when fully developed recirculating flows are observed.

Figure 4.11 shows the mean velocity taken along the core of the device DC1 with and without an applied electric field. When only PF is present in the device (dashed curve), the velocity is about 500 µm/s in the wide segments while the velocity becomes 6 x higher in the narrow microchannel segments. At these velocities, no recirculating flows are observed at the diverging and converging elements. The main consequence of the application of a counter EOF on PF is a general drop of the magnitude of the velocity in the microfluidic device. The solid line in Figure 4.11 corresponds to the simulated magnitude of the velocity when EOF and PF co-exist in opposite directions. In this case, boundary conditions were chosen such that the flow rate is close to zero. The graphic shows that the velocity reduces slightly in the narrow channel due to EOF. Flow is bi-directional and hence, PF is predominant in the core. The chart in Figure 4.11 also shows the sudden drop of the velocity magnitude at the gradual expansions and contraction elements when EOF is applied. Simulations indicate that the magnitude of the velocity at the core is reduced by a factor of two in the wide segments after the 2nd diverging element, whereas the magnitude of the velocity is nearly zero in the other wide segment. The sudden drop of the magnitude of the velocity can become more significant if larger values of *E* and of *Δp* are employed to form recirculating flows (see [12]). This illustrates the important consequence of opposing EOF and PF on the velocity distribution.

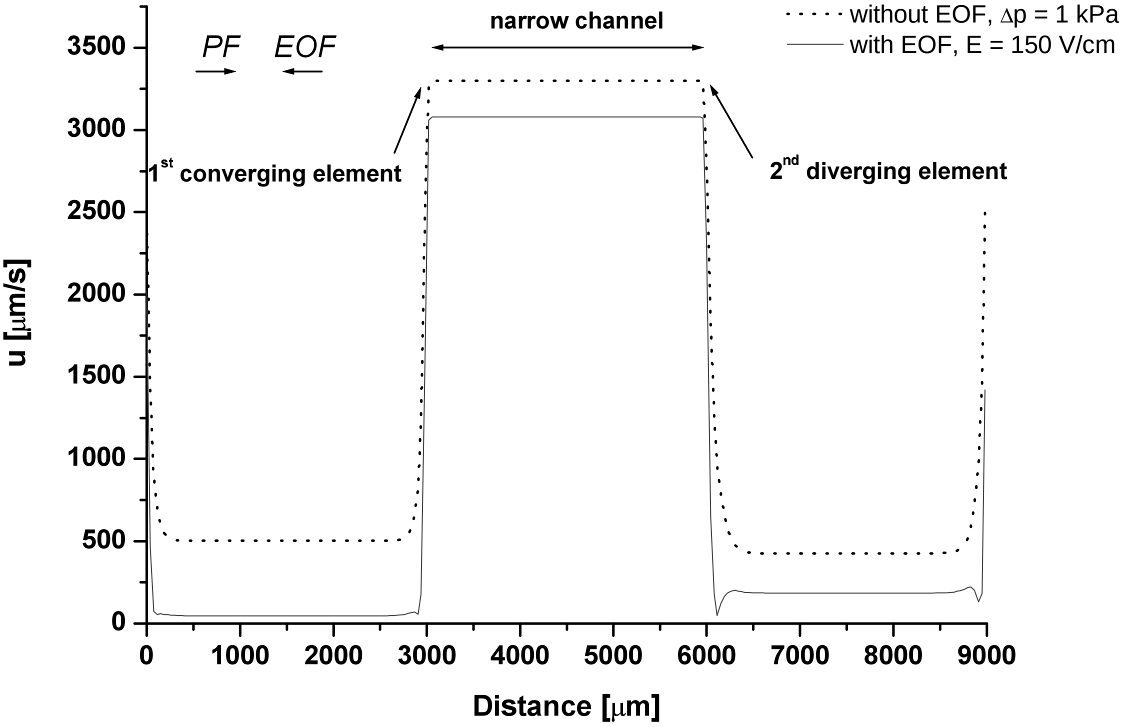

Figure 4.11
Chart illustrating the significant decrease of the velocity in the device due to the bi-directional flow (and recirculating flows) when EOF and PF are opposed. The velocity was calculated along the core of the device at Δp = 1 kPa (dot line) and E = 300 V/cm and at Δp = 1 kPa (solid line) E = 0 V/cm.

Figure 4.12 compares linear velocities obtained experimentally with the current monitoring method (u_{mea}) with uncorrected (u_{sim} uncorrected in Figure 4.12) and corrected simulated velocities (u_{sim} corrected) under conditions such that recirculating flows are fully developed (Q = 0 cm^3/s). The operating conditions corresponding to the experiment were *E* = 150 V/cm and *Δp* = 470 Pa. When these values are inserted in the solver parameters without using the calibrations (see section 4.4.1), the corresponding simulated velocity is 2 times lower than u_{mea} in the wide segment before the 1st converging element, 1.2 times lower in the narrow segment and 2 times higher in the wide segments after the 2nd diverging element. Once calibrated, it can be seen in Figure 4.12 that the $u_{sim} = u_{mea}$.

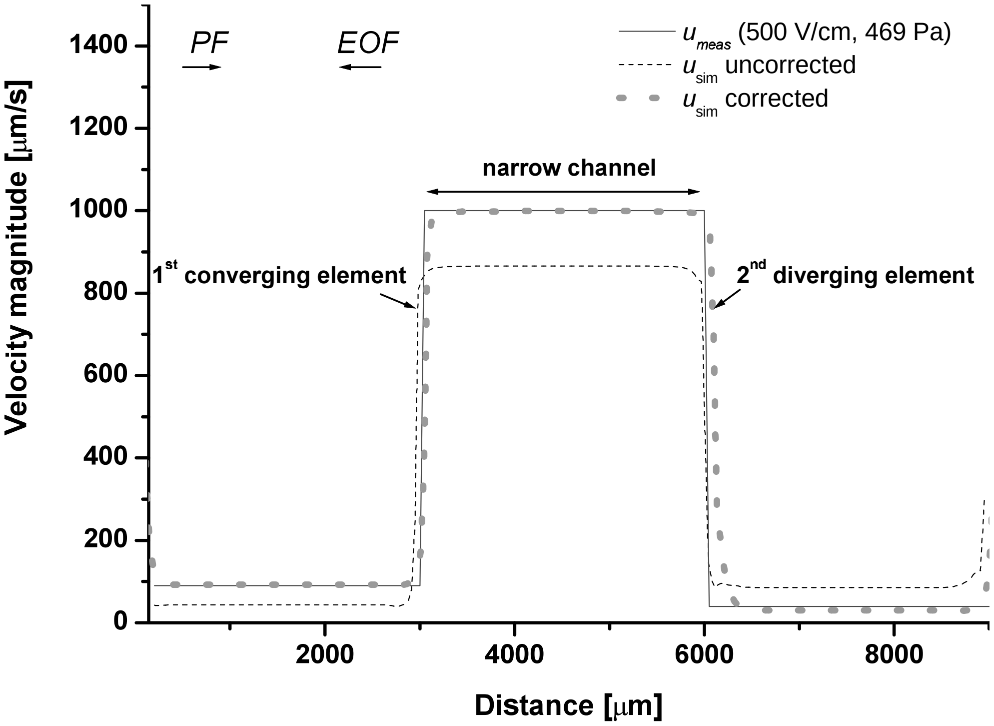

Figure 4.12
Comparison between the measured linear velocity, uncorrected simulated linear velocity and corrected simulated velocity across the 1st converging and 2nd diverging elements under conditions where recirculating flows are fully developed.

4.4.2.4 Discussion on the Generation of Recirculating Flows

Simulations of DC1 and other devices (DC2, DC3 and other devices with similar layouts), proved that minor losses were induced under conditions where a bi-directional flow is generated in the narrow microchannels, and that this happens under conditions close to zero net flow. Under these conditions, simulation results show the existence of an adverse PF-induced-pressure gradient at the convergent elements in addition to an adverse EOF-induced gradient at the divergent elements. In other words, EOF increases the resistance to the PF at the diverging elements, while PF increases the resistance to EOF at the convergent elements. The existence of an adverse pressure gradient induced by EOF at microchannel entrance/exit was also observed by Y. Zhang et al. [11]. These adverse pressure gradients become relevant when overall flow rate approaches zero. In fact, in addition to bi-directional flow formation in the narrow channels, steady and reproducible recirculating flows are generated due to these adverse pressure gradients. Recirculating flows are simultaneously created at each entrance of the divergent and convergent elements. However, depending on which transport mechanism is involved to induce these adverse pressure gradients, the influence on streamlines will be quite different. At the diverging microchannel elements, the adverse pressure gradient is induced by EOF. At these locations, simulations showed that flow divides from the core, giving rise to recirculating flows. Moreover, simulations indicate that a sort of depression is generated locally, where planar recirculating flows are observed. In fact, streamlines are suddenly deflected towards the bottom of the device as they would encounter a virtual wall. At the converging microchannel elements, the adverse pressure gradient is induced by PF. The situation is almost analogous except that flow separates from the walls of the converging elements. Another difference is that the virtual barrier forces the flow to return inside the narrow channel from the bottom to the core of the device. Thus, flow recirculation at diverging and converging channel elements situated at opposite ends of a narrow microchannel combined with bi-directional flow in the channel itself, yield a well-defined, stable, recirculating flow pattern through the channel. This is true in the plane of flow and perpendicular to the flow.

Thus, both simulation and experiment indicate that additional pressure losses are induced to the system by the generation of recirculating flows. These losses resemble minor losses observed in macroscopic pipe systems. The presence of these minor losses can explain the mismatch between the theoretical and the experimental values of the average velocity observed in section 3.3.1.2 of Chapter 3.

4.5 Simulation of Controlled Recirculating Flows

Recirculating flows, eddies, and more generally, minor losses were also observed in other microfluidic systems. In systems where no additional transducers are used, minor losses are merely due to a special geometry like sudden contractions inserted into the stream of a gas flow [13] or ridges on the floor of microchannels [14]. The recirculating flows presented in this work are generated by combining a bi-directional flow and microfluidic devices with microchannels of non-uniform cross-sections. The common point of all these systems is that particular flow patterns, not expected at very low R_e, are obtained. However, the main characteristic that differentiates the recirculating flows generated with the technology presented in this work from other systems is that these flows, formed at diverging and converging elements, are entirely controlled.

4.5.1 Recirculating Flows Control

One interesting example of recirculating flow control is the modulation of the recirculating flows. By varying one of the two pumping components, EOF or PF, velocity distribution and magnitude can be varied. This was already observed with the help of beads in Chapter 3 (sections 3.5.1 and 3.5.2) and is confirmed by the simulations. Figure 4.13 features 4 simulations of the same device for a fixed E (= 250 V/cm) and for different Δp. The μ_{EOF} corresponds to 30 mM carbonate buffer pH 9. The 3-D substructure is characterized by an opening angle of 180° and a depth of 25 µm and by $A_2 / A_1 = 3.7$. According to the direction of PF, the substructure is by definition a diverging element. The simulation shows the evolution of the velocity vector field of the flow in a plane halfway between the top and the floor of the device as a function of Δp. The size of the arrows corresponds to the velocity magnitude of the flow. The size of the recirculating flows in the plane is given by a_{sim}, and b_{sim}, shown in Figure 4.13. a_{sim} and b_{sim} correspond to the length and the width of the recirculating flows, respectively. When the recirculating flow motion is fully developed ($Q = 0$), both a_{sim} and b_{sim} do not equal zero. The size of the recirculating flows is plotted in Figure 4.14 as a function of the Δp.

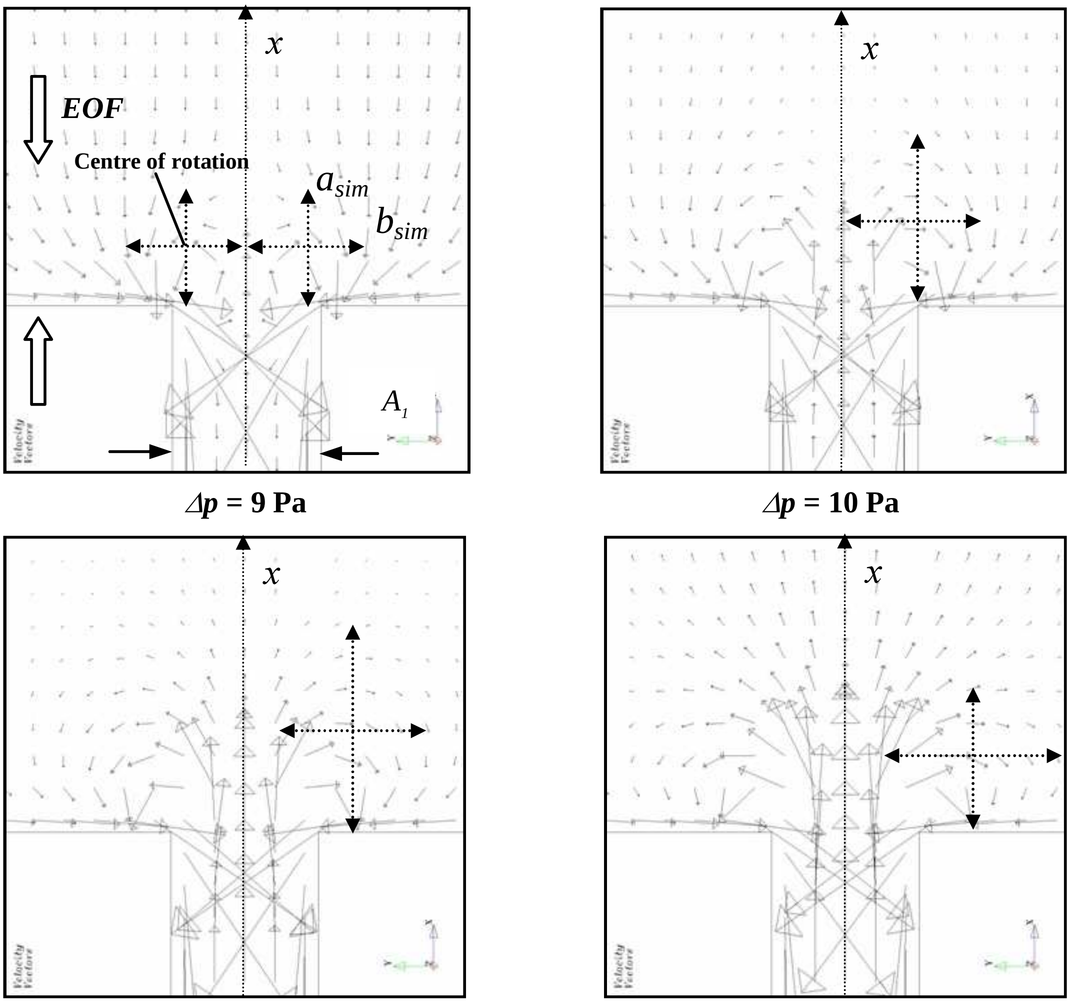

Δp = 9 Pa **Δp = 10 Pa**

Δp = 11 Pa **Δp = 12 Pa**

Figure 4.13
Evolution of recirculating flows at the diverging element as a function of Δp for E = 250 V/cm.

As mentioned previously, a pair of recirculating flows very similar to a vortex is generated symmetrically about the *x-axis*, as shown in Figure 4.13. Their center of rotation is located on each side of the central axis x, where a_{sim} and b_{sim} intercept each other. At 9 Pa, a bi-directional flow is present in the narrow microchannel, and PF coming out of the narrow microchannel is totally deflected towards the walls, while

EOF is predominant in the wider segment (the recirculating flows are fully developed). As Δp is raised up to 10 Pa, the velocity at the core of the narrow channel becomes greater. PF coming out of the narrow microchannel is much faster but undergoes also a higher deceleration at the entrance of the diverging element due to the presence of the adverse pressure gradient induced by EOF. As Δp increases, this mechanism becomes more accentuated, until the pressure is high enough to overcome the adverse pressure gradient. Simultaneously, recirculating flows cease to be fully developed and PF overcomes EOF in the wide channel. In parallel, the recirculating flows widen and seem to reach a maximum size at Δp equal to 11 Pa. Once PF starts to overcome EOF in the wide microchannel, a_{sim} starts to decrease. It can be also observed that the center of rotation of the recirculating flows moves away from the x-axis as Δp augments.

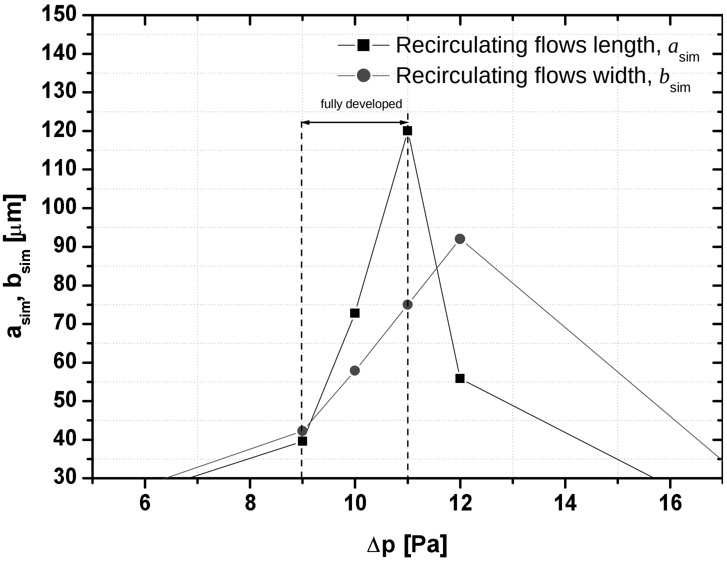

Figure 4.14

Graphic showing the evolution of the size of the recirculating flows versus Δp. The zone where recirculating flows are fully developed is between the dashed lines.

Figure 4.15 shows that the size of the steady recirculating flow patterns also be monitored by tuning the potential for a given Δp. In this case, θ_{div} = 120. It was observed that the higher the E and Δp for a given geometry, the larger the range of E and Δp where the recirculating flows are fully developed.

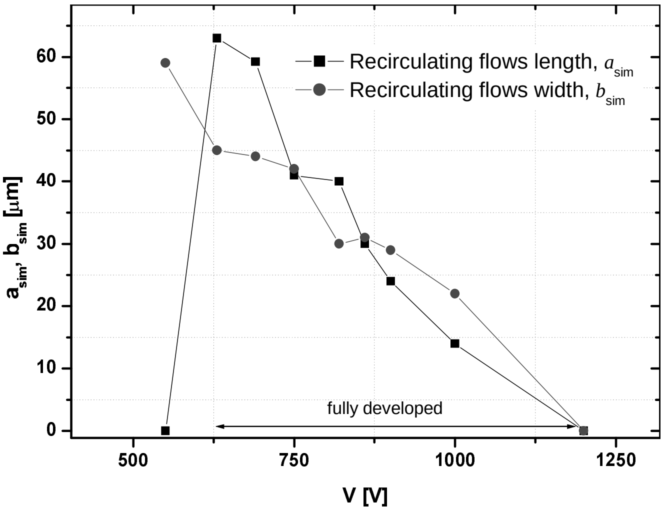

Figure 4.15
Size of the recirculating flows pattern as a function of E, for a fixed Δp, in a 120° diverging microchannel element.

4.5.2 Influence of the Geometry on Recirculating Flows

Simulations were also used to investigate the influence of diverging and converging element geometry on recirculating flow size and strength. Simulation results are compared with experiments carried out with beads under similar boundary conditions. The diverging elements of Figure 4.16 are designed so that cross-sectional area ratios (A_1/A_2) are constant and only θ varies. Wide and narrow segments have the same depth and have the D-shaped cross-sections produced by isotropic etching of Pyrex with hydrofluoric acid. Boundary conditions for Figure 4.16 are identical for each device, that is, an average electric field of E = 250 V/cm and a pressure of Δp = 10 Pa. For θ_{div} = 180° and 120°, recirculating flows are present at the entrance to the diverging microchannel. For θ_{div} = 120°, the circulatory flow zone is more extended (closer to the sidewalls), due to the shape of the expansion. For θ_{div} = 90°, recirculating flows are located about 200 µm from the entrance of the diffuser, and are smaller and characterised by lower velocities than for θ_{div} = 120° and 180°. For θ_{div} = 60°, flow recirculation is again at the beginning of the diffuser but velocities are weaker than θ_{div} = 120° and 180°.

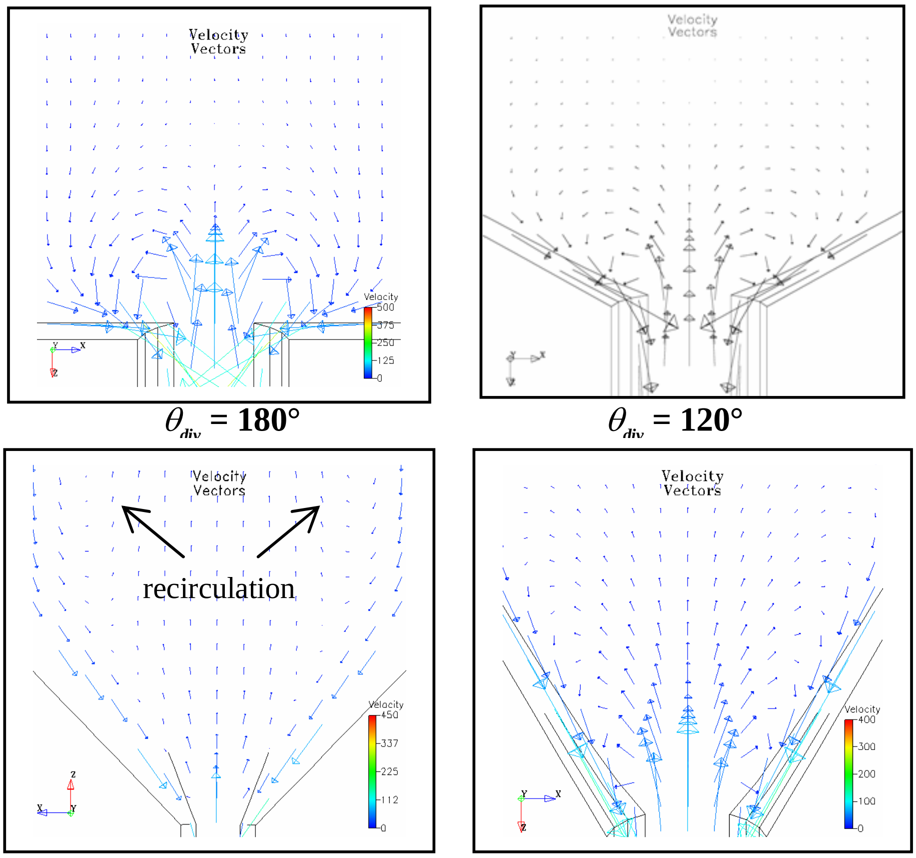

θ_{div} = 180° θ_{div} = 120°

θ_{div} = 90° θ_{div} = 60°

Figure 4.16
Simulation of the velocity vector field of the flow (μm/s) of diffusers with different values of θ.

These results illustrate the influence of diffuser geometry on the shape and the location of recirculating flows. For θ_{div} = 180° and 120°, simulations show that recirculating flows are fully developed. This means that these geometries facilitate the formation of the adverse pressure gradient induced by EOF. For 90°, the recirculating flows are almost irrelevant while for 60°, they are more developed but not as pronounced as for 120° and 180°. However, this does not necessarily mean that for $\theta_{div} < 120°$, fully developed recirculation cannot be established. In fact, simulations show that they can be generated for 90° and 60° with different boundary conditions. From the various simulations performed, it seems that as soon as a gradual contraction or expansion are present in the stream flow, adverse pressure gradients can be generated, inducing flow recirculations at those elements. Figure 4.17 (a) and (b) illustrate the differences in recirculating flows for diffusers with θ_{div} = 180° and

60°, respectively, as obtained from simulation. Figure 4.17 (c) and (d) show snapshots of the corresponding bead clusters (using the same boundary conditions) that were formed upon addition of 1 μm Protein-A fluorescent beads to the system.

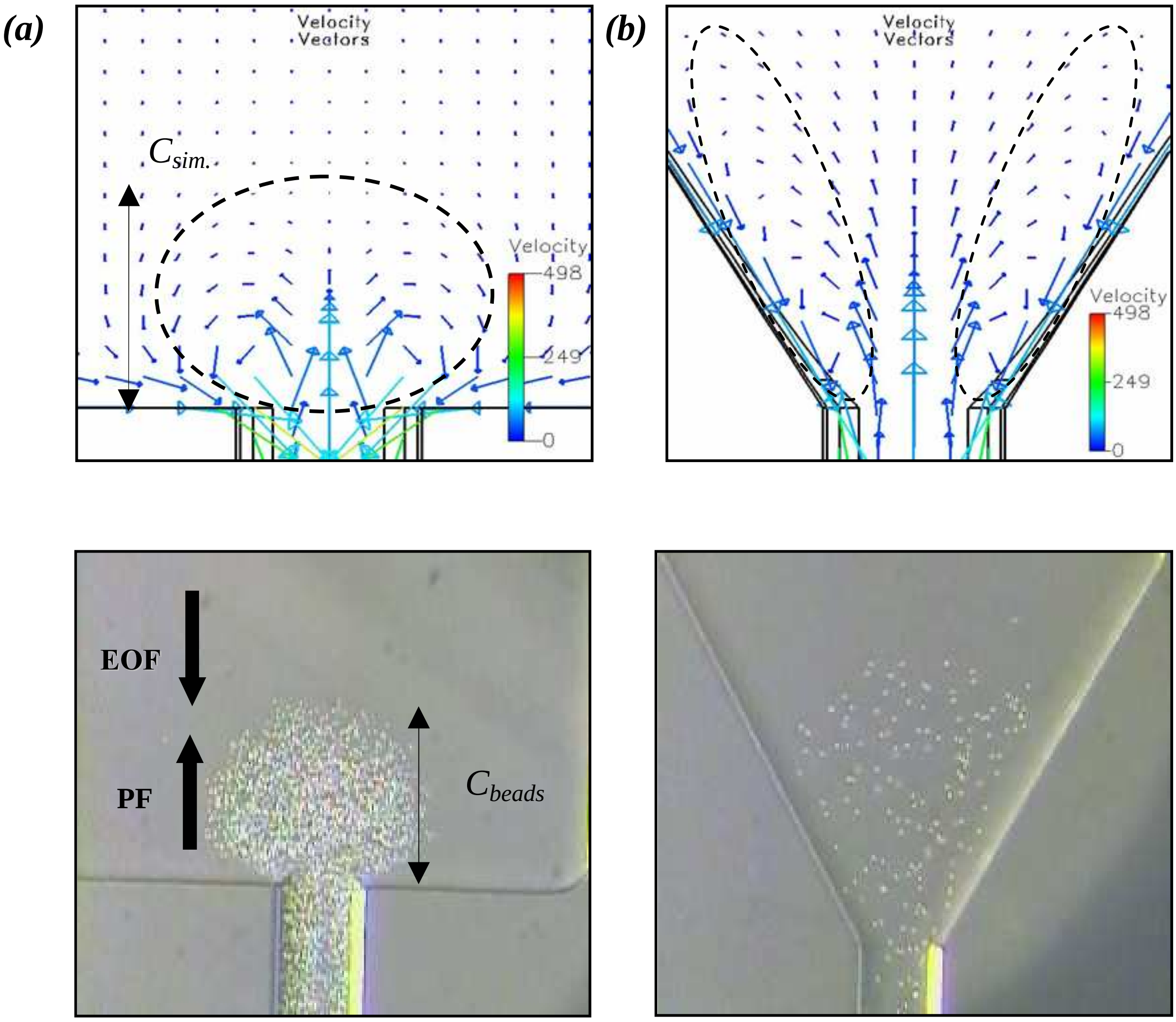

Figure 4.17
Simulation of the velocity vector field of the flow (μm/s) of diverging channels with (a) θ_{div} = 180° and (b) θ_{div} = 60°, and the corresponding photos (c) and (d) showing bead clustering. Boundary conditions are the same for both diverging channels, that is, an average electric field of E = 200 V/cm, P_H = 7 mbar and A_2/A_1 = 7. Protein-A-coated fluorescent beads (1 μm) were used to obtain these images.

For θ_{div} = 180°, the predicted velocity vector distribution for the recirculating flow is confined within an estimated maximum distance, C_{sim}, of 50 μm from the mouth of the diverging element. Most of the flow coming from the narrow channel is deflected in this recirculating flow. In fact, actual experiment shows that beads rarely escape once caught in this tight rotating pattern, and are instead fed back into the narrow channel. The size of the observed cluster is about C_{sim} = 90 µm. For θ_{div} = 60°, this velocity vector distribution is more elongated and is located closer to the sidewalls ($C_{sim.}$= 100 µm). The resulting cluster is larger and less dense than in the 180° case. It extends a distance, C_{beads}, of 130 µm from the mouth of the diverging element, due to diffuser opening angle and a weaker recirculating flow velocity on average. Not all of the flow emerging from the narrow channel is deflected. Flow in the middle of the channel escapes the zone of recirculation. Thus, recirculating flow is not fully developed and beads can escape from the zone of recirculation.

4.6 Bead Modeling

FlumeCAD cannot simulate the motion of charged beads in a flow induced either by PF or EOF. However, it was shown in section 3.3.2.3 (Chapter 3) that if the μ_{beads} is known, then beads can be assumed to behave like ions in a flow, characterized by an apparent mobility. According to this assumption, modeling of bead flow was carried out by implementing the empirical values of μ_{beads} into the solver parameters. The way to simulate beads proposed here is then to replace the electro-osmotic mobility of the buffer μ_{EOF} by $\mu' = \mu_{EOF} - \mu_{beads}$. Hence, it consists in the simulation of a buffer characterized by μ'.

4.6.1 Simulation of a Bi-directional Flow of Beads

In Chapter 3, it was observed for G7 that the flow of 2-µm polystyrene beads with a $\mu_{beads} \cong 4 \times 10^{-4}$ cm^2/Vs was bi-directional at each of the following experimental parameters: E = 150 V/cm ; 300 V/cm, 600 V/cm for Δp = 0.19 kPa, 0.49 kPa and 0. 85 kPa, respectively. In order to simulate the flow of these beads under the experimental conditions mentioned above, μ_{beads} is included in the solver parameters, by replacing μ_{EOF} with μ_{EOF} - μ_{beads}.

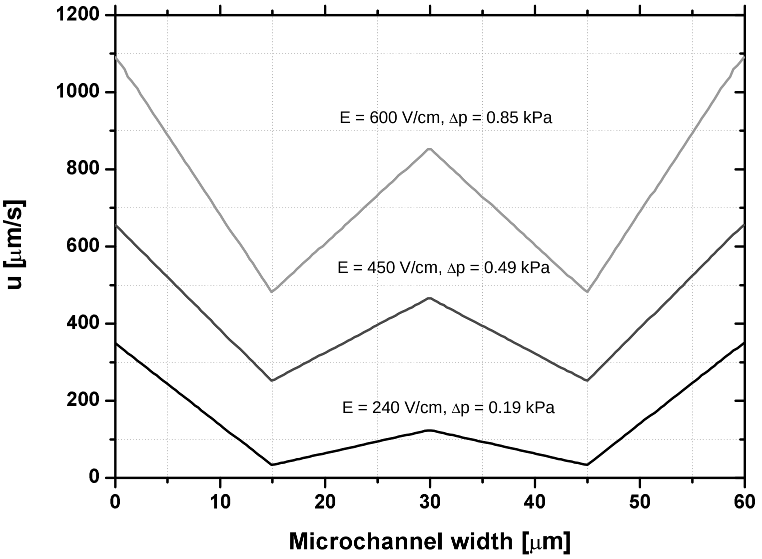

Figure 4.18
Simulations of the velocity magnitude for G7. The simulated velocity magnitudes are in a plane parallel to the top of the microchannel and located at the core. The device G7 was modelled using 3600 meshed elements.

Figure 4.18 shows the simulations of the velocity magnitude as a function of microchannel width calculated along a horizontal axis located halfway between the top and the bottom of the microchannel G7. The simulations show that a bi-directional flow is present in each situation. Simulated flow rates indicate that a bi-directional flow of beads forms close to a zero net flow of beads. Zero net flow was also observed when a bi-directional flow of buffer was simulated in section 3.1.3.1. A comparison of simulations and the experiments suggests that μ_{beads} can be considered as an apparent electrophoretic mobility. Therefore, beads undergo the same electrokinetic effect of negatively charged spherical ions in a buffer, under application of an electric field along a microchannel. Similar simulations performed with 2.5-μm polystyrene beads with a $\mu_{beads} = 1.3\text{x}10^{-4}$ cm^2/Vs confirm this trend. However, this statement can not be generalized for larger beads since this has not been verified. Moreover, effects due to friction may be more relevant as the beads size increases.

4.6.2 Simulations of the Recirculating flow of Beads

Verification of this method by comparing experimental and numerical boundary conditions necessary to generate recirculating flows of 2-µm beads in DC1 showed that it is a good approximation for bead flow modeling. It was found, for instance, that the 2-µm beads delineated recirculating flows for the following set of boundary conditions: E = 164 V/cm, 317 V/cm and 576 V/cm for Δp = 180 Pa, 450 Pa and 790 Pa, respectively. Using the calibrations performed on the solver parameters in Section 0 for DC1, μ' and the boundary conditions above, simulations showed that recirculating flows of beads are formed at converging and diverging elements.

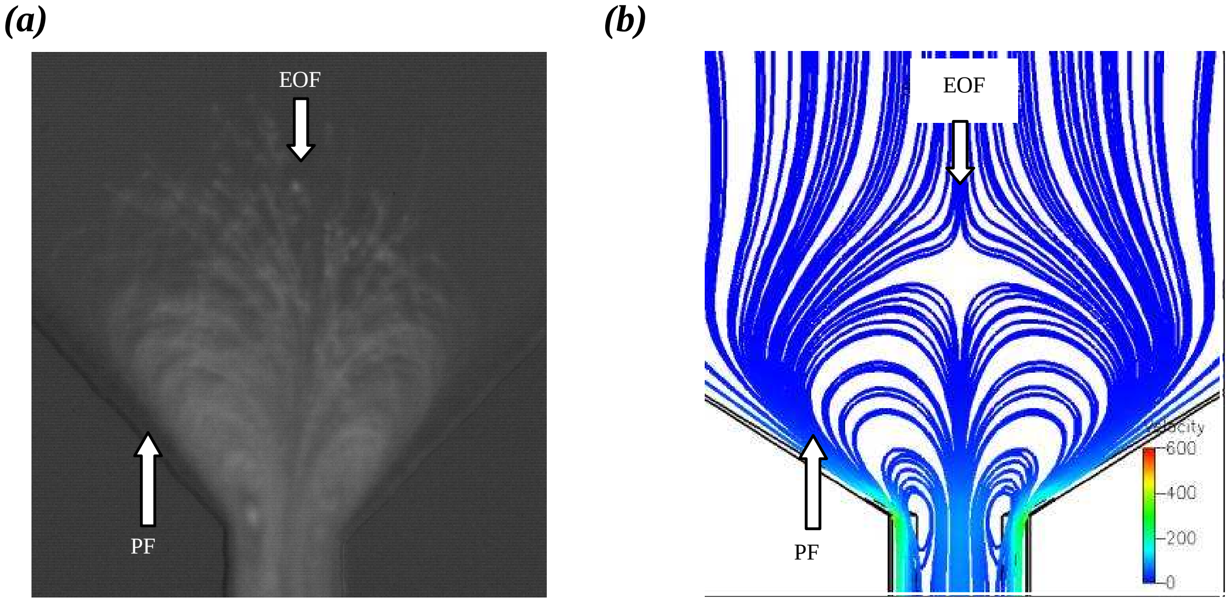

Figure 4.19
Comparison of recirculating flows of beads and simulated streaklines of the buffer.(a) 2-μm beads recirculating at a diverging element (b) simulation of the streaklines under similar boundary conditions.

The flow pattern visualized with the 2-µm polystyrene beads in Chapter 3 and the streamlines calculated with the solver are very similar. This similarity is illustrated in Figure 4.19. The averaged frames of Figure 4.19 *(a)* show recirculating flow of beads at the diverging microchannel elements. This picture makes it possible to deduce the trajectory followed by the beads. In Figure 4.19 *(b)*, the simulation of the streaklines at a diverging microchannel element shows that bead trajectory and flow streamlines are similar at this location. Note that the fluid delineate a vortex motion close to the edge of the corners at the diverging channel entrance.

4.7 Conclusion

In this chapter, it was demonstrated that simulation tools can be used to:

1. predict the generation of bi-directional flow and recirculating flows, supporting the observations made with beads
2. visualize the recirculating flows in the three dimensions
3. predict recirculating flow pattern
4. provide qualitative information on bead motion
5. predict bead cluster formation

FlumeCAD, a CFD tool, was employed to investigate the streamlines in 3-D microchannels under conditions where an EOF and a PF are opposed. It was observed that the values of the electrical field strength and the values of the applied pressure used in the simulations needed to be calibrated with experimental values in order to compare simulation results with experimental results. In the case of a microchannel of uniform cross-section, the applied pressure used in the simulations was corrected to fit with experimental results. For microchannels with diverging and converging elements, correction of both the electric field and the applied pressure was necessary.

Once calibrated, simulations showed that bi-directional flow is obtained close to zero net flow, and that recirculating flows are generated in diverging and converging elements under this condition. Comparison of the simulated streamlines of the recirculating flows of beads with experiments performed with beads shows that beads delineate faithfully the simulated flow patterns. As observed with the beads in Chapter 3, the simulation tool predicts that the recirculating flows are not only formed at zero net flow. This could explain the non-linear behaviour of the measured average velocity using the current monitoring method in Chapter 3. It was also shown that 3-D simulations revealed the presence of convective movement, in addition to the recirculating flows formed in a plane parallel to the top of the device. This convective movement is the consequence of the significant pressure gradient created by the opposition of EOF and PF. In fact, simulations suggest that the recirculating flows are due to an increase of the adverse pressure gradients generated at diverging and converging elements by the opposition of EOF and PF.

It was demonstrated that recirculating flows can be fully controlled by tuning either the electric field or the applied pressure. Simulations also allow the influence of the geometry on the recirculating flows velocity and size distribution to be determined.

A method to simulate the bead motion by incorporating μ_{beads} in the solver parameters showed good results for the beads used in this study. However, this method can be used only if the μ_{beads} is known and if it can be assumed that beads behave like spherical ions.

4.8 References

[1] L. Bousse, A. Minalla, M. Deshpande, K. B. Greiner, and J. R. Gilbert, "Optimization of sample injection components in electrokinetic microfluidic systems," presented at MEMS '99, Orlando, Fl., USA, 1999.

[2] L. Bousse, A. Kopf-Sill, and J. W. Parce, "An electrophoretic serial to parallel converter," presented at Transducers'97, Chicago, 1997.

[3] S. V. Ermakov, S. C. Jacobson, and J. M. Ramsey, "Computer simulations of electrokinetic transport in microfabricated channel structures," *Analytical Chemistry*, vol. 70, pp. 4494-4504, 1998.

[4] N. A. Patankar and H. H. Hu, "Numerical simulation of electroosmotic flow," *Analytical Chemistry*, vol. 70, pp. 1870-1881, 1998.

[5] S. V. Ermakov, S. C. Jacobson, and J. M. Ramsey, "Computer simulations of electrokinetic injection techniques in microfluidic devices," *Analytical Chemistry*, vol. 72, pp. 3512-3517, 2000.

[6] K. A. G. Qiu Fulian, Adrian C. Fisher, Nicholas P. C. Stevens, and Richard G. Compton, "Computer-aided design and experimental investigation of a hydrodynamic device: the microwire electrode," *Anal. Chem.*, vol. 72, pp. 3480-3485, 2000.

[7] L. G. Hu, J. D. Harrison, and J. H. Masliyah, "Numerical model of electrokinetic flow for capillary electrophoresis," *Journal of Colloid and Interface Science*, vol. 215, pp. 300-312, 1999.

[8] A. Olsson, G. Stemme, and E. Stemme, "Numerical and experimental studies of flat-walled diffuser elements for valve-less micropumps," *Sensors and Actuators A*, vol. 84, pp. 165-175, 2000.

[9] P. J. O'Rourke, D. C. Haworth, and R. Ranganathan, "Computational Fluid Dynamics," *ASM Handbook*, vol. 20, 1998.

[10] Deshpande et al., "Numerical framework for the modeling of electrokinetic," presented at SPIE Microfluidics conference, Santa Clara, CA, 1998.

[11] Y. Zhang, R. W. Barber, and D. R. Emerson, "Creeping electro-osmotic flow through micro-channels," presented at MME 02, Sinaia, Romania, 2003.

[12] G.-L. Lettieri, E. Verpoorte, and N. F. de Rooij, "Planar microfluidic devices for controlled vortex generation," presented at Transducers'01 Eurosensors XV, Munich, Germany, 2001.

[13] X. D. Li, W. Y. Lee, M. Wong, and Y. Zohar, "Gas flow in constriction microdevices," *Sensors and Actuators A*, vol. 83, pp. 277-283, 2000.

[14] A. D. Stroock, S. K. W. Dertinger, A. A., M. I., S. H. A., and G. M. Whitesides, "Chaotic mixer for microchannels," *Science*, vol. 295, pp. 647-651, 2002.

5 Bead based assay on-chip

5.1 Introduction

In this chapter, we present a new way of handling beads on chip that is not limited by a need for physical barriers and additional transducers (see Chapter 1). Our approach is to trap and manipulate beads using fluid flows only. Creation of a bi-directional flow in a microfluidic device with diverging and converging elements can result in the generation of controlled recirculating flow or vortices [1-3]. In Chapter 3 it was shown experimentally that small, fluorescent polymer beads delineated the streamlines induced by opposing PF to EOF in microfluidic devices with diverging and converging elements. It was also observed that they can actually be captured and preconcentrated in these rotating flow patterns as well [2]. Moreover, the clusters of freely moving beads that result are formed under conditions close but not equal to zero net flow. EOF still dictates the overall direction of flow, as discussed in section 3.4.2. Thus, clusters of freely moving beads can be held in place while being sequentially perfused by different solutions, leading to the possibility of performing bead-based chemistry [4]. In Section 5.4, we demonstrate the practical application of this phenomenon for facilitated bead handling in microfluidic devices with an analysis of fluorescein-labeled biotin at different concentrations using 2-μm streptavidin-coated beads (SC beads).

5.2 Bead Handling in Microchannels

As mentioned in Chapter 1, one of the big issues related to bead-based assay on chip is the handling of beads. There are basically four main steps for doing bead-based assay on-chip: 1) bead trapping, 2) analyte loading for reaction, mixing or extraction with the trapped beads 3) bead flushing 4) detection and release of beads. In this section, a new approach for bead trapping using only fluid flows is presented. It is shown that the three main steps for doing a bead-based assay on-chip can be accomplished by generating a bi-directional flow on a device featuring diverging and converging elements.

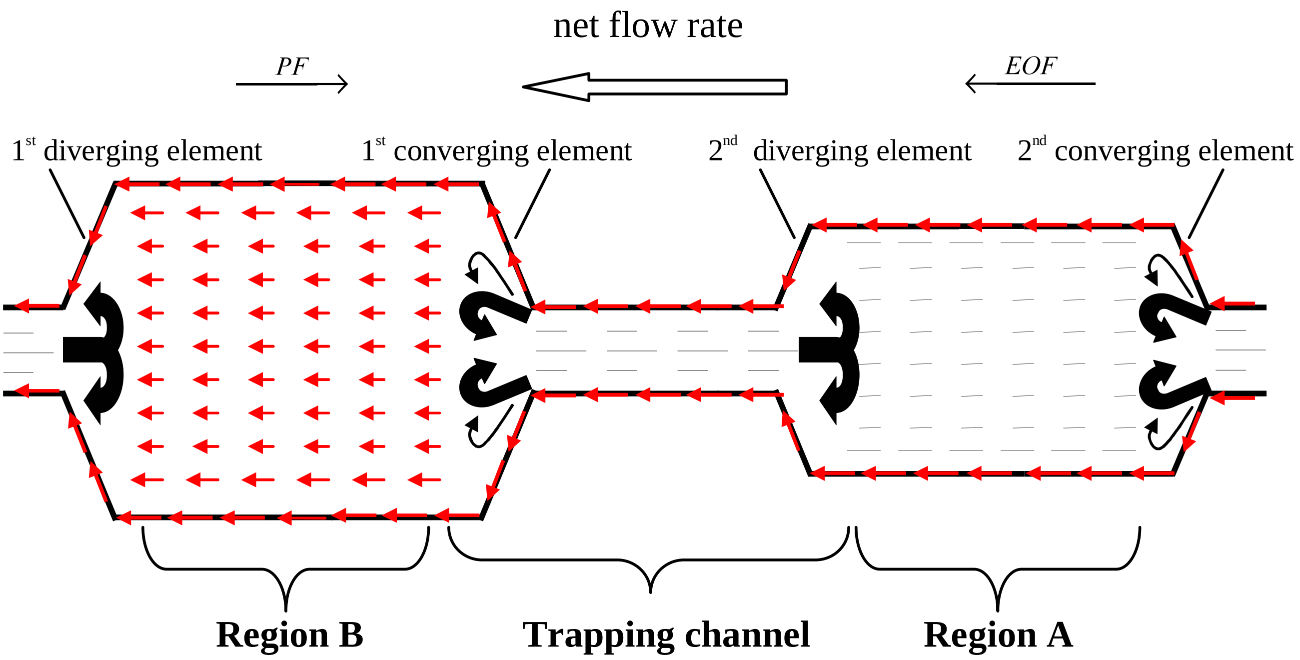

Figure 5.1
Top schematic view of the microfluidic device. Streamlines described by the beads in the plane halfway between the top and bottom of the channel (parallel to the page) are shown. EOF and PF conditions are such that recirculating flows fully developed. In the large channels, streamlines of the flow follow EOF. A pair of symmetrical recirculating flow patterns is generated at each end of the trapping channel, and beads recirculate between the diverging and converging channel elements through this channel.

The streamlines shown schematically in Figure 5.1 are substantiated by experiments performed with beads (diameter ranging between 1 and 6 μm) and simulations (see Chapter 3 and 4), which reveal the generation of recirculating flow patterns at diverging and converging channel geometries when PF and EOF are opposed and flow rates approach zero. More intriguing, beads can be captured and preconcentrated in the narrow channel between the diverging and converging channel element, to form clusters of freely moving beads at both these elements. This part of the microfluidic device is thus termed “the trapping channel” (Figure 5.1).

5.2.1 Efficiency of the Trapping Channel

Beads will be prevented from escaping from the trapping channel to any large extent depending on the equilibrium between three factors: the recirculating flows, the geometry of the microfluidic device, and the μ_{beads}.

To achieve efficient trapping of the beads, the recirculating flow of beads has to be fully developed. As shown in Section 3.4 and 3.5 of Chapter 3, fully developed and steady recirculating flow of beads are obtained when EOF equilibrates PF so that the average net velocity of the beads is close to zero. When steady recirculating flows are fully developed, different regions of flow can be distinguished in the microfluidic device with two diverging/converging elements inserted into the stream flow. Most of the beads present in the transition region A (see Figure 5.2) are attracted towards the trapping channel driven by EOF, while beads in the vicinity of the 2nd converging element are caught in the recirculating flows at this element. Once in the trapping channel, beads start to recirculate between the 2nd diverging element and the 1st converging element, caught in the recirculating flow pattern. In the other transition region (B), the EOF is also predominant and consequently beads present in this region are driven towards the 1st converging elements, where they are caught in the recirculating flow of beads present at that location. The efficiency of the trapping channel is very sensitive to the transition region B. In fact, it was noted that it was easier to confine the beads at the diverging element of the trapping channel than at the converging element. This is due to streamline configuration: if beads manage to escape the virtual barrier at the diverging element, they will be brought back because of the EOF, while at the converging elements they will be carried away by the EOF.

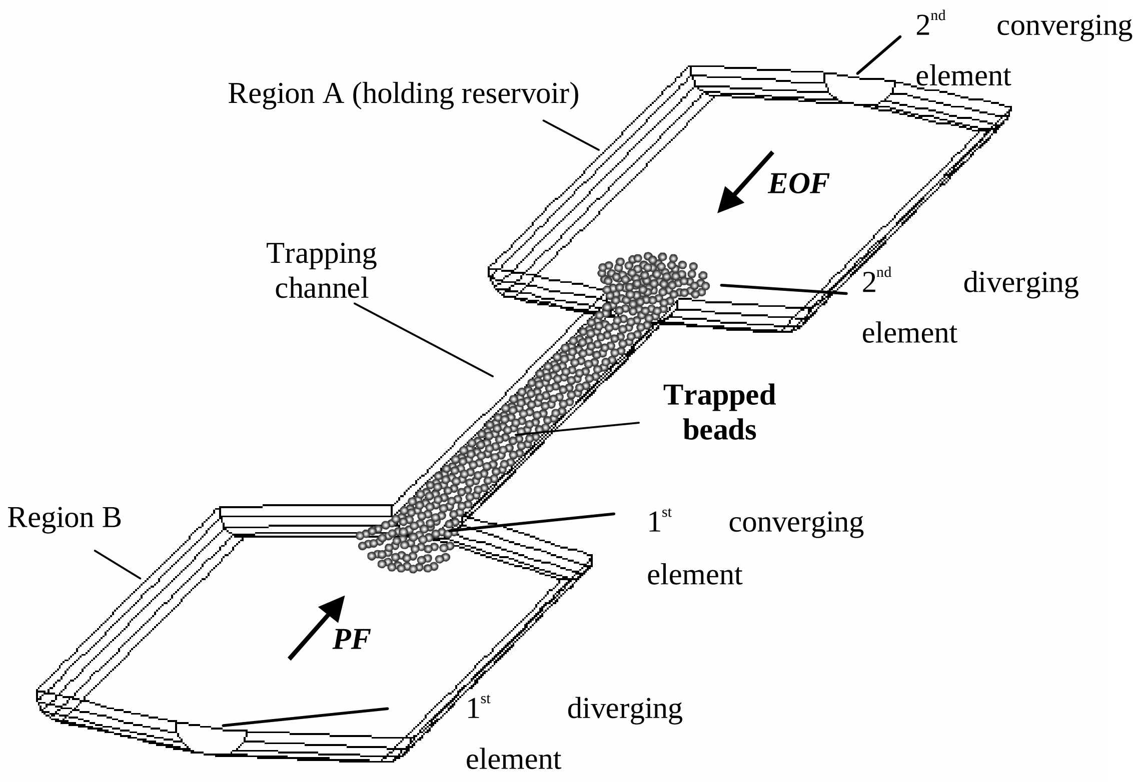

Figure 5.2
Schematic of a substructure where recirculating flow of beads are generated by opposing an EOF to a PF. As a result, beads are attracted and trapped in the trapping channel. The zone of interest is divided in 3 parts: Region A and B and the trapping channel.

The second and third factors that determine the efficiency of the trapping channel are the geometry of the device and the μ_{beads}. Video imaging shows that the length of the trapping channel, l_{tc}, and the lengths and widths of the two wider channel elements of the microfluidic device are important parameters for controlling bead trapping. If a good balance is found between the recirculating flows of beads and the geometry, beads will be prevented from escaping the trapping channel to any large extent, though a few beads will always be lost depending on their μ_{beads}. For example, it was observed that for 2-µm SC beads with a $\mu_{beads} \cong -4\text{x}10^{-4}$ cm^2/Vs, about 5 beads were lost every 2 seconds at the converging element and no beads were lost at the diverging element for $\theta_{div} = \theta_{con} = 90°$ when SB1 was used (see chapter 2 for layout and dimensions). On the other hand, for the same device, Protein A-Fluoresbrite YG-carboxylate beads (PA beads) (Polysciences, $\mu_{beads} \cong -3\text{x}10^{-4}$ cm^2/Vs in 10 mM sodium tetraborate buffer pH 9) can be totally confined in the trapping channel. It was found that for $l_{TC} \geq 3000$ µm, $A_2/A_1 \cong 7$, $A_4/A_1 \cong 5$, $60° \leq \theta_{div} \leq 180°$, and $90° \leq \theta_{con} \leq 120°$, the beads used in this study ($0 < |\mu_{beads}| < \mu_{EOF}$) were well confined to the trapping channel. These values for the various geometric parameters are empirical, however, and could be optimised using simulation tools to better predict flow patterns.

The spatial occupation of the trapping channel by the beads is strongly influenced by both the μ_{beads} and the l_{tc}. For example, in DC2 with an $l_{tc} = 3000$ µm, the 2.5-µm Alignflow beads are distributed uniformly along the trapping channel, as sketched in Figure 5.2. This was not the case for the 2-µm and 1-µm SC bead, 1-µm PA bead and 2-µm carboxylate bead (the μ_{beads} of these beads was $\geq -3 \text{ x } 10^{-4}$ cm^2/Vs). By suddenly changing streamlines, these beads tend to reverse before reaching the converging element of the trapping channel and to be more concentrated at the diverging element of the trapping channel. Consequently, a gradient of bead concentration is observed and the concentration of these beads decreases gradually as they approach the converging element. The sketch of Figure 5.3 illustrates the 1-µm PA beads spatial distribution observed experimentally. For example, depending on the operating E and Δp, it was observed that the 1-µm PA bead reversed direction about 300 to 600 µm before reaching the converging element of the trapping channel. In region A and B, beads still followed the EOF, while beads caught in the recirculating flows appeared to be more attracted towards the anaode. This phenomenon seems to be mainly due to the fact that the beads were negatively charged and therefore, had a μ_{beads} counter to EOF.

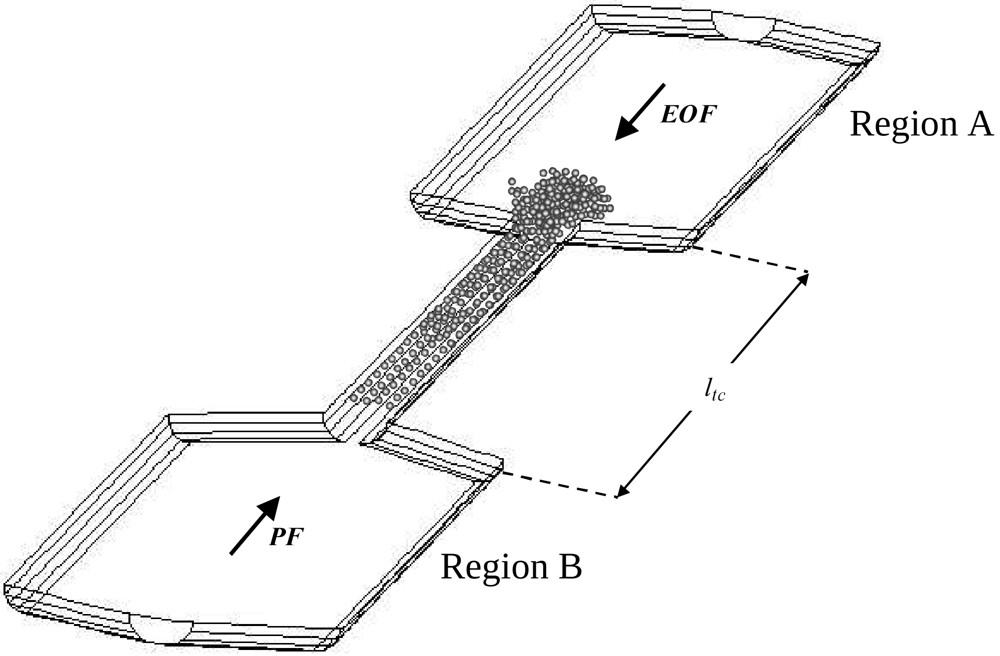

Figure 5.3
Example of uneven bead distribution observed for 1-µm PA beads. The beads were more concentrated at the diverging of the trapping channel. A concentration gradient was observed towards the converging element.

The size-to-charge ratio of the beads plays then an important role in their distribution in the trapping channel, as well as the *E* used. As a result, for the same trapping channel dimensions but for different kinds of beads with different μ_{beads} and size, the distribution of the beads in the trapping channel is dissimilar. This phenomenon explains why the detection window was located at the diverging element of the trapping channel for the PMT-based analysis discussed in section 5.4.

The preconcentration of the beads in the trapping channel depends on the initial concentration of beads prior to introduction to the microfluidic device. The initial concentration of beads was set in general at $c_{\mathrm{beads}} = 5 \times 10^7$ beads/mL, after resuspension in the new buffer (see Chapter 2). The concentration of the beads in the trapping channel was estimated using video imaging simply by counting the number of beads at the diverging element, according to the previous discussion on bead distribution. It was estimated that the concentration of the trapped beads was $c_{\mathrm{beads}} = 10^8$ beads/mL, which yields a preconcentration factor of 2. However, the number of beads that are trapped depends strongly on the number of beads present in the Region A of the microfluidic device (see Figure 5.2). Only the beads present in the wide channel corresponding to Region A will be attracted and caught in the recirculating flows generated in the trapping channel. This means that keeping l_{tc} at 3000 µm and increasing the length of Region A will lead to a higher preconcentration factor. This is an important feature of this technology that was not fully investigated. In fact, the optimisation of Region A and of the l_{tc} dimensions could allow entirely filling the trapping channel with beads and hence obtaining a range of trapped bead concentrations. Region A is therefore called the holding reservoir.

5.2.2 Bead Perfusion and Flushing Using EOF

The ability to capture and preconcentrate beads locally in a microchannel network is fundamental to bead handling in these devices. Combining this with controlled bead transport from one point to another provides an added flexibility which is not possible in packed bed systems. Recirculating flow and bead trapping in our devices is generated under conditions where a net flow still exists in the direction of the EOF. This is illustrated by the simulations of the recirculating flows of

Figur Figure 5.4. The simulations show of the velocity vector field of the flow at the converging element in three horizontal planes: *(a)* at the top (z = 20 µm) of the microfluidic device (z = 0), *(b)* in the middle (z = 10 µm) and *(c)* at the bottom.

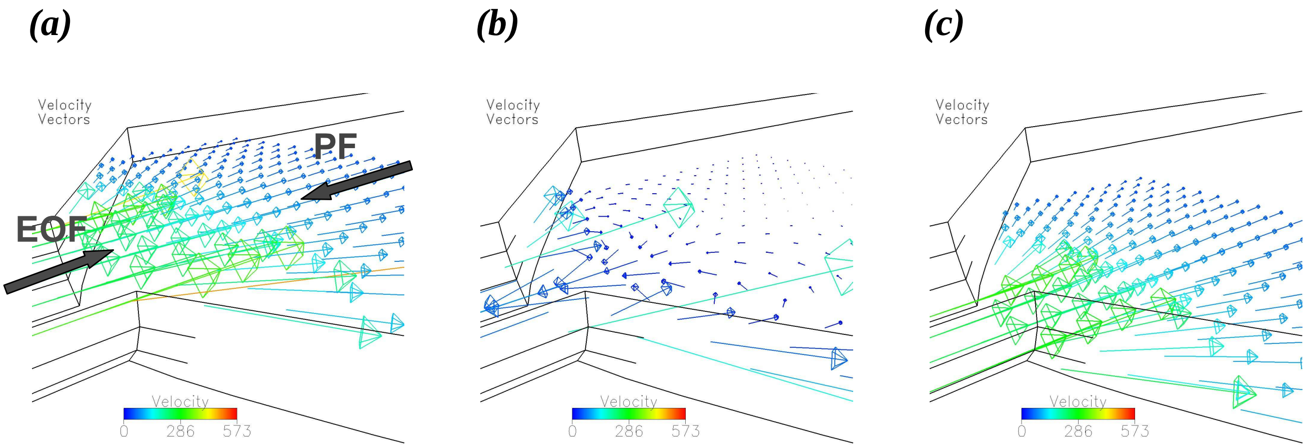

Figure 5.4
3-D simulation of the velocity vector field of the flow in three planes, at the converging element. EOF is predominant at the bottom and top of the device, while recirculating flows are located around the core of the device.

The size of the arrows corresponds to the magnitude of the flow velocity. The direction of EOF and PF are also indicated. The simulations of Figure 5.4 indicate that the recirculating flow zone is localized around the middle of the channel while close to the walls EOF is predominant (see Chapter 4 for more details). This is very important because it means that there is still a net flow rate in the direction of EOF not only in the transition region but also where recirculating flows happen. More generally, EOF is predominant everywhere along the walls when steady and fully developed recirculating flows are generated. Since the beads follow the streamlines, it means that it should be possible to retain clusters of freely moving beads in the trapping channel while sequentially pumping sample(s) and reagents from different reservoirs over them using EOF. (This assumes that conditions suitable for electrokinetic reagent delivery can be maintained upon switching from one solution to the next.) Mixing resulting from recirculating flows and bi-directional flow ensure delivery of reagent to the beads over the entire depth of the microchannel. This is the basis for doing on-chip heterogeneous assay using beads.

5.2.3 Assay Systems

The use of streptavidin-coated (SC) beads offers numerous advantages over other solid supports. For instance, they are ideal reagent delivery vehicles providing large reactive surface areas and interact strongly with the molecule biotin. However, when SC beads are used for the solid-phase in a heterogeneous assay, it is imperative to ensure that the binding capacity is completely characterized for the size and molecular weight of ligand that the final application will ultimately use. The streptavidin-biotin interaction was chosen for its large affinity constant and many applications in immunochemistry [5, 6] and in biosensors [7]. The binding of streptavidin, a protein produced by Streptomyces avidinii, with biotin, a vitamin found in every living cell, is characterized by a very high affinity K_A. In solution, K_A is about 10^{15} M^{-1} for streptavidin-biotin interaction, reflecting a bond strength approaching that of a covalent bond. It is therefore possible to reduce both the time necessary in protein conjugation as well as the expense of wasted reagents. However, in the present study, the streptavidin-biotin binding reaction occurs on a solid surface. It was reported that the K_A for streptavidin-biotin binding was lower on surfaces than for interaction in a homogeneous solution [8] [9]. It was also shown that when beads were used as substrate for the heterogeneous assay, the size of the beads influenced the affinity [10, 11]. The binding rate will decrease with increasing size of the solid phase.

Figure 5.5 *(a)* shows a sketch of streptavidin/biotin binding, while a sketch of the dynamic binding of SC bead/fluorescently-labelled biotin is shown in *(b)*. Biotin also binds to avidin, but streptavidin has a lower non-specific binding characteristic than avidin, explaining why it is more suitable for immunochemistry applications [12]. The binding of streptavidin with biotin is normally very rapid and is unaffected by a wide range of pH and temperature. In the recirculating-flow microfluidic devices, both SC beads and biotin are continuously in motion. Due to this new approach for performing the binding of SC bead with biotin, the binding is considered as dynamic, in contrast with binding systems (wells, tube etc…) where diffusion only is involved.

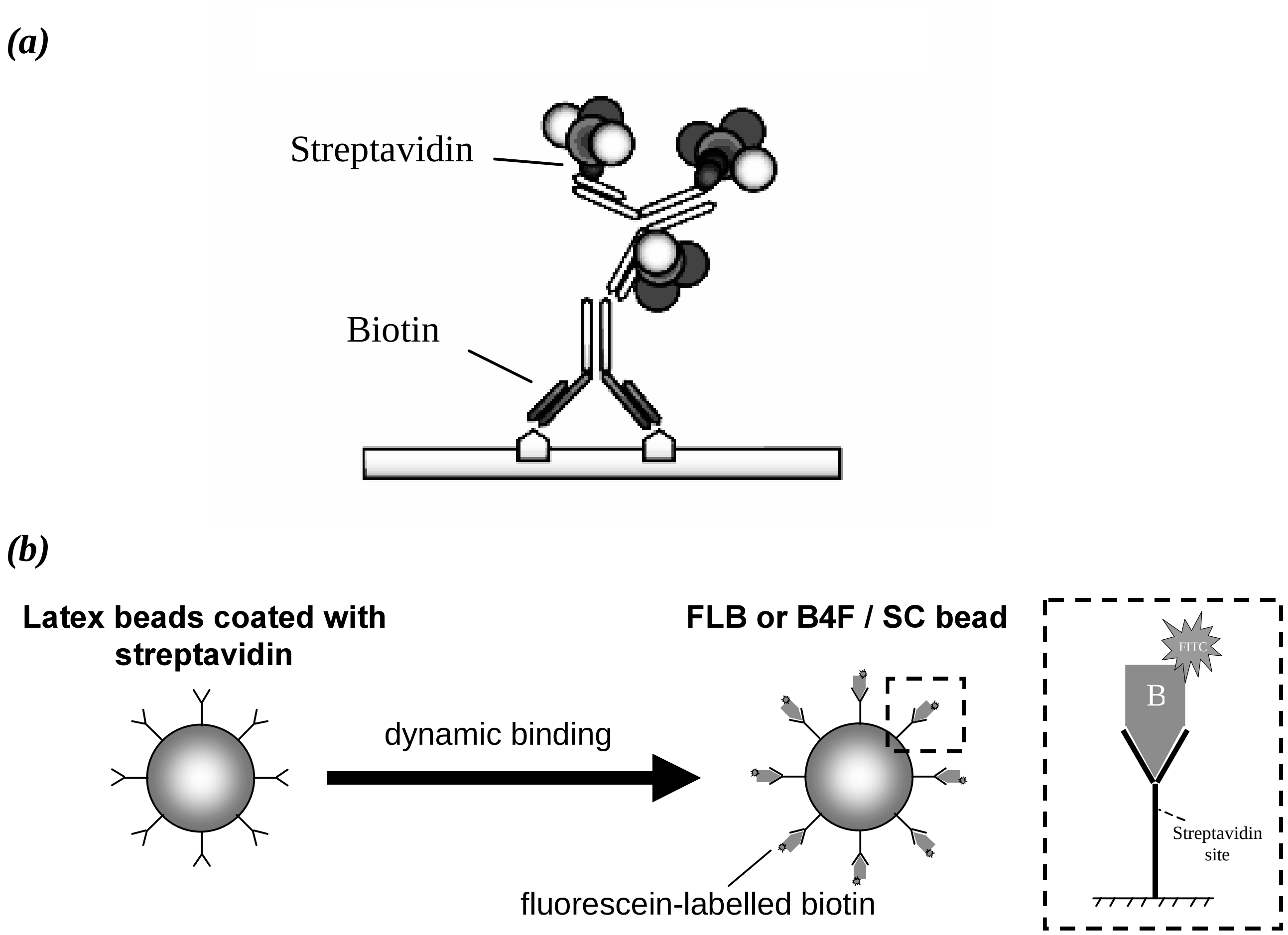

Figure 5.5
(a) Conventional streptavidin/biotin system (picture from the internet: http://www.nichirei.co.jp/bio/english/protocol/ssmp/advantages_a.html). One streptavidin molecule in solution has four biotin binding sites [13]. (b) Schematic of the dynamic bonding of an SC bead and FITC-labelled biotin.

SC beads of various dimensions can be found on the market. An important parameter that characterizes these beads is their binding capacity or the number of available binding sites. In fact, the main reason for constructing an assay based on SC beads is to simplify subsequent ligand attachment to the beads (biotinylated DNA, Protein A, antibodies or antigens).

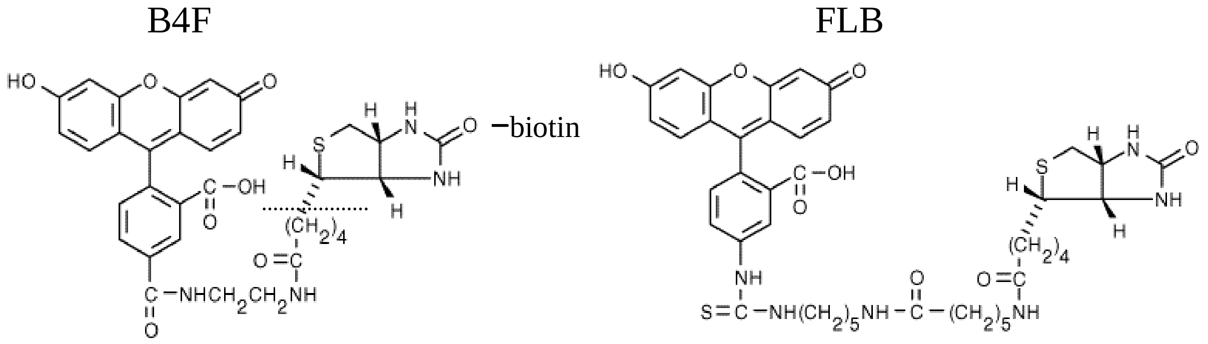

Figure 5.6
Structure for B4F ($C_{33}H_{32}N_4O_8S_2$, M.W = 644.70 g) and FLB ($C_{42}H_{50}N_6O_8S_2$, M.W. = 831.01 g). According to the manufacturer, when B4F is used as a marker, fluorescein is quenched due to close proximity of the(strep)avidin. FLB experience less quenching because of the longer spacer separating biotin from fluorescein

As analyte (or ligand), either biotin-4-fluorescein (B4F) or 5-((*N*-(5-(*N*-(6-(biotinoyl)amino)hexanol)amino)pentyl)thioureidyl)fluorescein (FLB) was used in the assay (both compounds were obtained from Molecular Probes Europe B.V., Leiden, The Netherlands). In B4F, the spacer length between fluorescein and biotin is 9 atoms long, whereas it is 21 atoms long in FLB (Figure 5.6). Hence, FLB is less prone to quenching than B4F. Using a simple kinetic model (see next section) and knowing the molecular weight of the FLB and B4F, it is possible to estimate the amount bond of each ligand to the SC beads.

5.2.4 Kinetic Model

Two important parameters can be extracted from the binding of SC beads with fluorescein-labelled biotin: (1) the forward rate constant that allows the affinity constant of the interaction to be estimated and (2) the binding capacity. To determine these values, a mathematical approach is necessary to quantitatively describe the binding. Since the SC bead/biotin system is similar to an immunoassay system, the binding theory used here is based on immunoassay binding theory [6, 14, 15].

Equilibrium binding

The bimolecular binding reaction of a specific ligand containing biotin (B) to biotin binding sites (S) can be expressed as:

$$S + B \underset{\mathrm{k_f}}{\overset{\mathrm{k_r}}{\rightleftarrows}} SB \qquad \textbf{Eq 5.1}$$

where k_f is the forward constant and k_r is the reverse rate constant. The binding rate equation is given by:

$$\frac{d[SB]}{dt} = k_f[S][B] - k_r[SB] \qquad \textbf{Eq 5.2}$$

where [S] is the concentration of binding sites (4), [B] the biotin concentration, and [SB] the concentration of complex. At equilibrium,

$$K_A = \frac{[SB]}{[S][B]} = \frac{k_f}{k_r} \qquad \textbf{Eq 5.3}$$

where K_A is the binding or affinity constant of the reaction.

The relation between *[S]* and *[SB]* is given by:

$$[S] = S_0 - [SB] \qquad \textbf{Eq 5.4}$$

where S_0 is the initial number of available biotin binding sites. The solution for the differential Eq 5.2 is:

$$[SB](t) = \frac{k_f[B]S_0}{k_f[B] + k_r}(1 - e^{-(k_f[B]+k_r)t}) \qquad \textbf{Eq 5.5}$$

In a homogeneous system, the rate constant k_f and k_r of the streptavidin-biotin system are reported to be 10^7 $M^{-1}S^{-1}$ and 10^{-8} $M^{-1}S^{-1}$, respectively [14]. The k_r being very small, the second term in Eq 5.2, which accounts for the dissociation, can be neglected. Consequently, Eq 5.5 reduces to:

$$[SB](t) = S_0(1 - e^{-k_f[B]t}) \qquad \textbf{Eq 5.6}$$

where t is the reaction time of the binding. If the starting concentration of the available biotin binding sites and the initial concentration of the ligand are known, as well as the amount of complex formed at time t, then the k_f can be estimated from Eq 5.6.

5.3 Experimental

To demonstrate that a heterogeneous analysis using beads can be performed with the new technology introduced in this work, binding experiments were carried out in microdevices SB1, SB2 and SB3 (see Chapter 2 for device layouts and dimensions), using 2-µm SC beads as reagent. Two operating modes were used to perform the dynamic experiment, depending on the way the beads were loaded up to the trapping channel: (1) the pressure-loading mode and (2) the EOF-loading mode. Initial binding experiments were carried out using the pressure-loading mode. EOF loading, developed later, was ultimately preferred to this mode because it allows more flexibility with respect to bead handling and ensures better control of the concentration of trapped beads.

5.3.1 Pressure-based Bead Loading

Figure 5.7 shows a schematic of the device and the different stages for the biotin-streptavidin binding experiment. The original bead buffer was replaced before experimentation by 10 mM sodium tetraborate buffer (pH 9) through centrifugation. Hydrostatic pressure was kept constant during the whole experiment, with only the applied potential being switched between reservoirs.

The binding experiment comprises four steps. 1) *SC bead loading and trapping:* SC beads ($c_{beads} = 10^7$ beads/mL) are introduced from reservoir 3 using a flow induced by application of hydrostatic pressure (column of buffer: 9 cm high (9 mbar)). Once past the second diverging channel, 1.5 kV is applied between reservoirs 1 and 3, giving rise to an opposing EOF. The SC beads are driven back and held in the trapping channel ($c_{beads} \cong 10^8$ beads/mL). 2) *Sample loading and binding:* While the SC beads are recirculating, the potential is switched (≅ 50 ms) from between reservoirs 1 and 3 to between reservoirs 2 and 4 (U_{24}= 1.5 kV). Labelled biotin is then loaded up to and through the trapping channel, and the freely moving SC beads are continuously perfused. 3) *Flushing:* After a certain incubation time, the potential is switched back again to reservoirs 1 and 4 to flush the excess sample away, while the newly bound labelled biotin-SC beads are still clustering. 4) *Detection:* Detection of fluorescently labelled biotin bound to SC beads is carried out at 20 μm from the second diverging channel entrance. Once an analysis is finished, the beads can be washed away by simply increasing the applied voltage, followed by collection in a waste reservoir (reservoir 4).

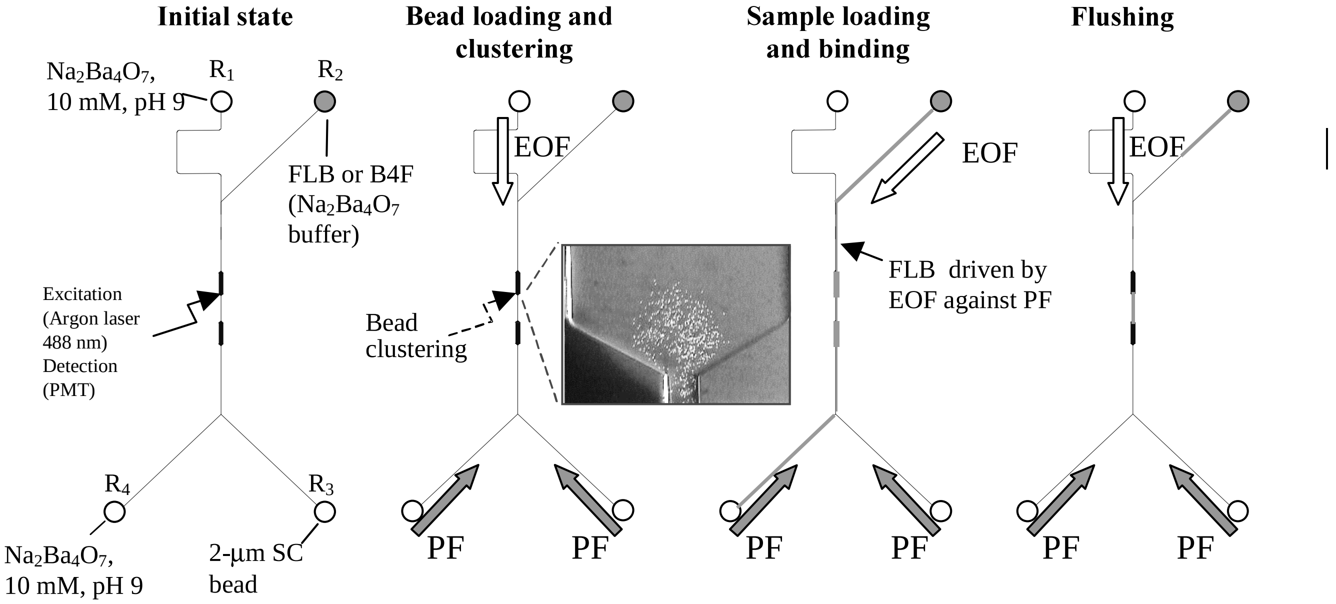

Figure 5.7
Initial state: Schematic of the 2 × 4 cm device used for the biotin-streptavidin binding experiment. Reservoirs 1 and 4 are filled with sodium tetraborate (10 mM, pH 9, $\mu_{EOF} = 6.2 \times 10^{-4}$ cm²/Vs), reservoir 2 with labelled biotin (solutions ranging from 0.4 to 4 μM in sodium tetraborate buffer were used) and reservoir 3 with 2-μm SC beads (5 μL in sodium tetraborate, $c_{beads} = 5 \times 10^7$ beads/mL).

5.3.2 EOF-based Bead Loading

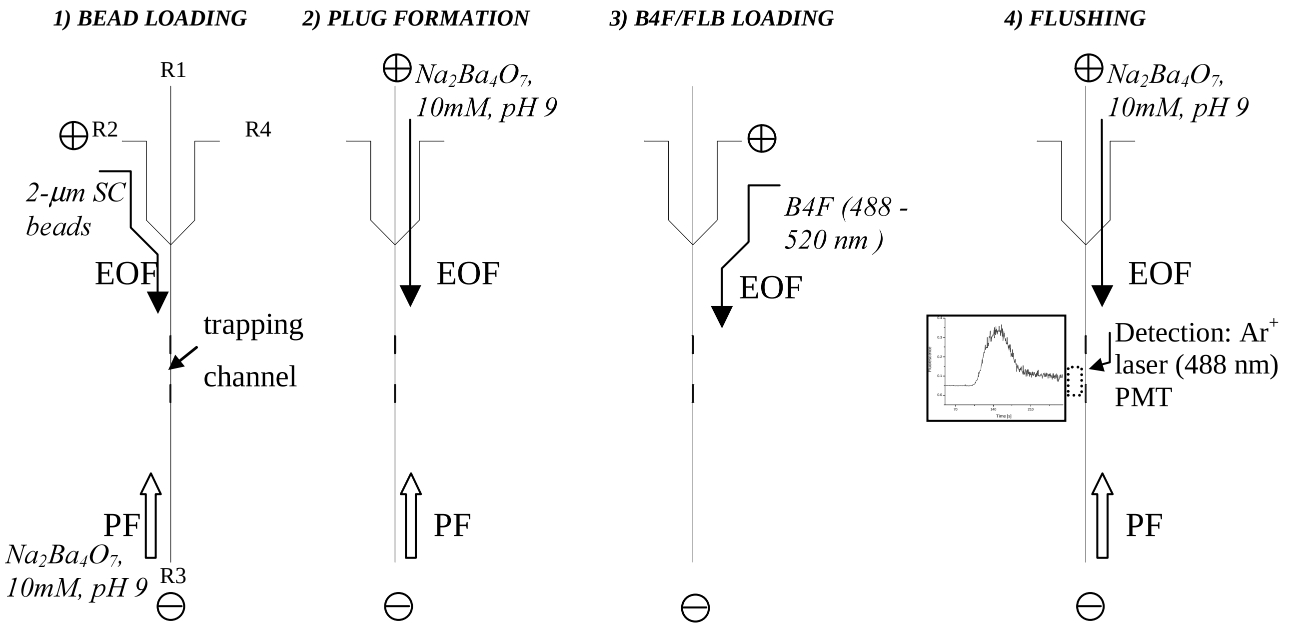

Figure 5.8

1) *The potential is applied between R2 and R3 (V_{23} = 1-3kV) during t_1= 60 - 100 s. Beads are loaded electrokinetically while a counter pressure (Δp = 0.3 – 1.2 kPa) is applied to the waste reservoir (R3).* 2) *In order to define a plug of beads, the potential is applied between R1 and R3 for a given time (t_2 ~ 10s).* 3). *B4F is driven by EOF to the trapping channel ($V = V_{43}$) and is mixed with the recirculating SC beads for a given time t_3 = incubation time.* 4) *Buffer flushes away excess unbound biotin. Once the detection is done, beads are flushed away towards R3 (V_{43} = 3kV).*

In this case SC beads are introduced into the device by electro-osmotic pumping. The experiment is performed exactly in the same way as in the pressure-loading mode, except that SC beads are loaded from R_2 by application of a large *E* so that it induces an EOF that overcomes the counter PF. When the beads reach the diverging element of the trapping channel, the *E* is switched to between R_1 and R_3 and decreased in order to create a plug of beads. The beads of this plug present in the wide segment (holding reservoir) are then trapped in the trapping channel. Hence, for each measurement, the beads are loaded for a given time t_1 (60 s to 100 s, depending on the *E*). The main advantage of EOF-based bead loading compared to the pressure-based bead loading is that the number of loaded beads is better controlled. This ensures better control on the newly bound SC bead/B4F complex concentration. Once the dynamic binding is achieved and the fluorescent signal recorded, the beads are driven towards R_3 by EOF.

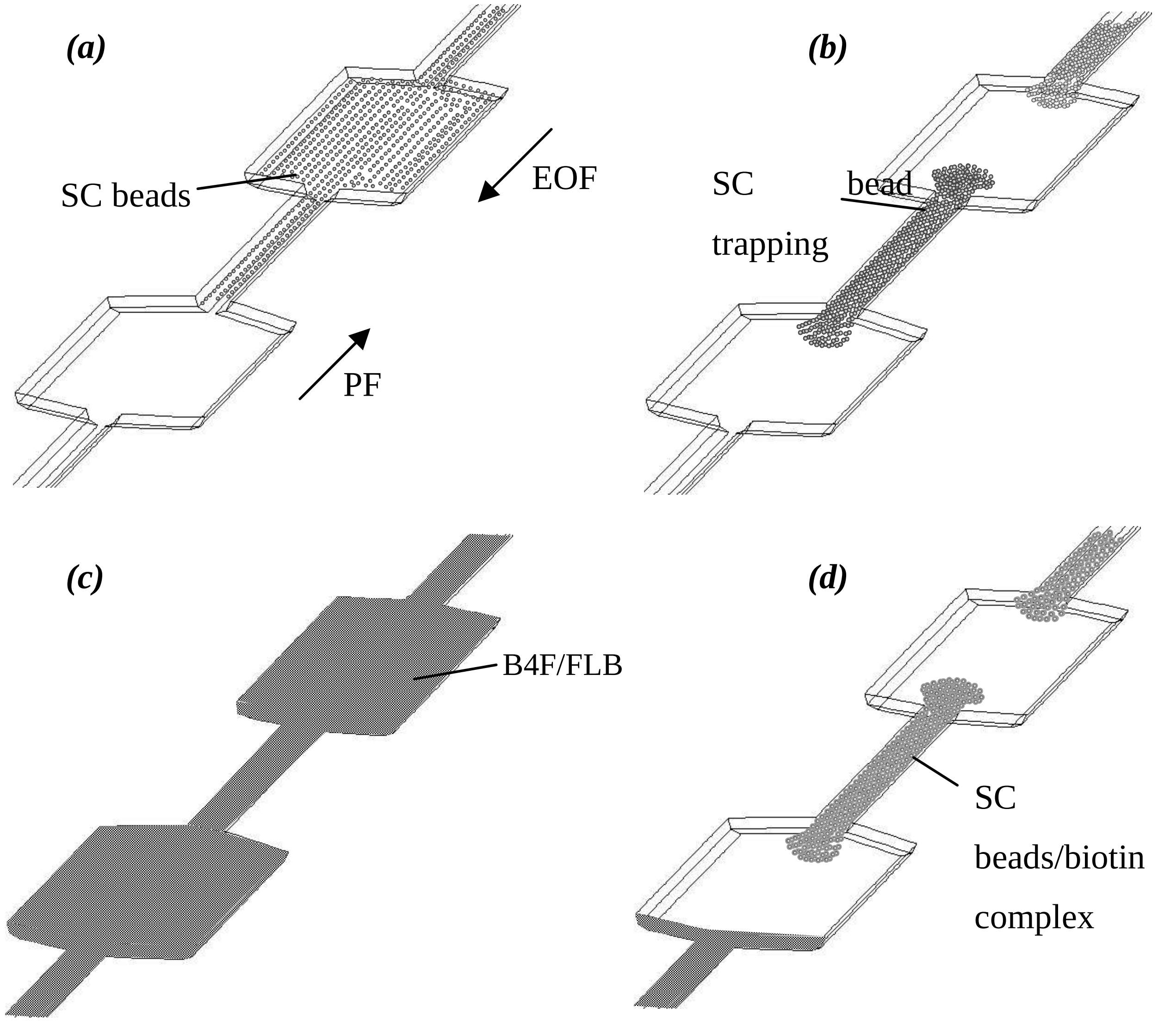

Figure 5.9
Sketch illustrating the dynamic SC bead/biotin binding in the EOF-based bead loading. (a) SC bead loading (b) SC bead trapping (c) trapped SC bead perfusion by FLB or B4F (d) flushing away of the excess unbound ligand.

The sketch of Figure 5.9 illustrates the four main steps observed experimentally during the on-chip bead/biotin binding using the EOF bead-loading mode.

Visual inspection of bead handling, using either a fluorescent microscope or video imaging, was combined with quantitative measurement of fluorescence using a PMT-based confocal detection system.

5.4 Results and Discussion

5.4.1 Dynamic Binding of Biotin/SC Bead Monitored with a Fluorescent Microscope

Figure 5.10 shows snapshots of the dynamic binding of trapped 2-µm SC beads with 200 nM B4F in the microfluidic device SB3. For this experiment, E = 130 V/cm and Δp = 5 kPa. In this case, the beads were introduced by the application of hydrostatic pressure. The dynamic binding was monitored using a fluorescent microscope. The picture frames, averaged over 2 s, were taken at the diverging element of the trapping channel. At 0 s, SC beads, caught in the recirculating flow pattern, are trapped but they are not visible since the B4F had not yet reached the trapping channel. No fluorescent signal is detected. At t = 200 s, the B4F has already reached the trapping channel and starts to bind to the SC beads. The reaction is visible because the beads become fluorescent. B4F, driven by EOF, is not visible with the fluorescent microscope settings used for this experiment. However, since the beads become fluorescent it can be concluded that the B4F preconcentrates on the bead. At 350 s, from video imaging, it appears that all the available streptavidin sites are saturated with the ligand.

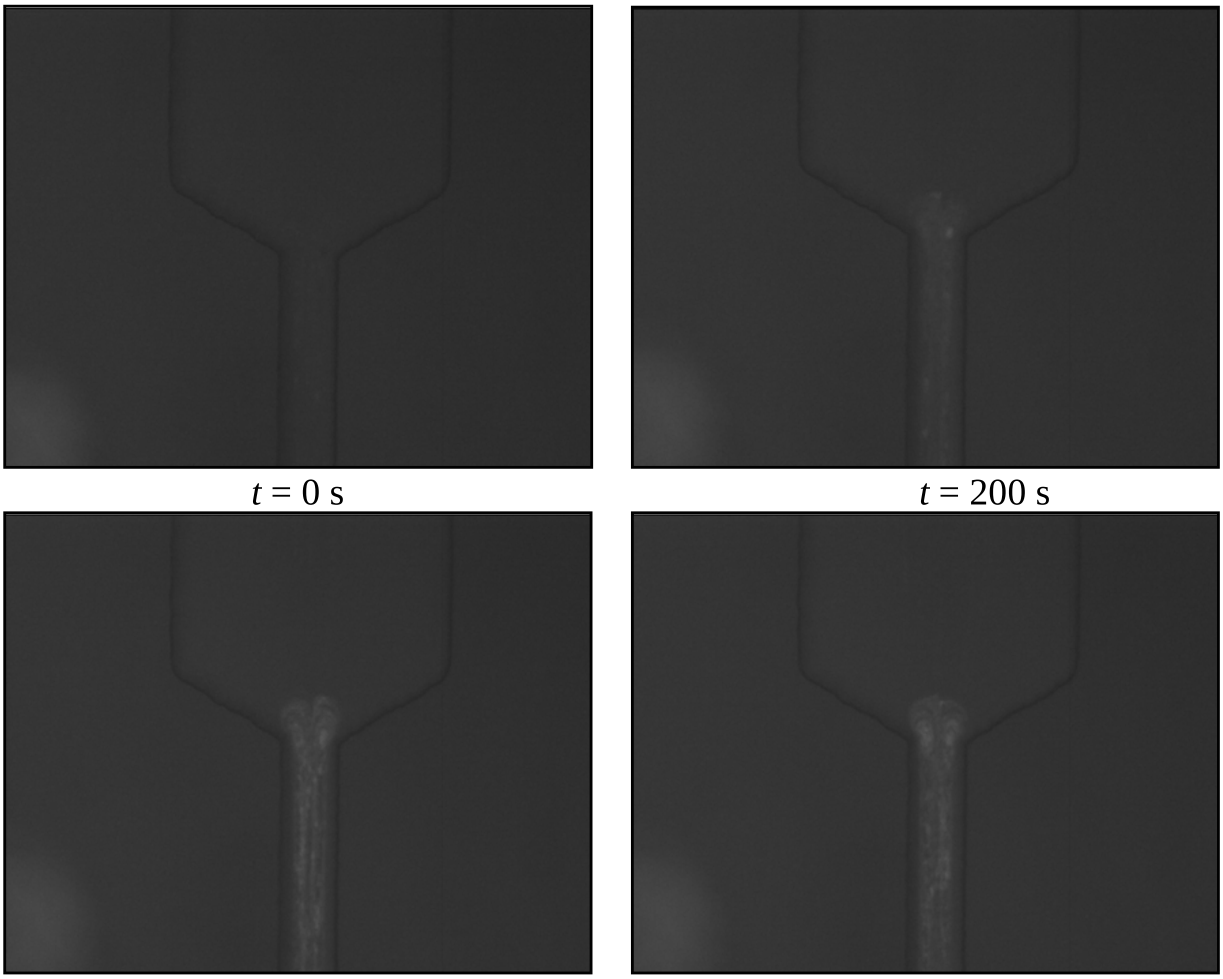

t = 0 s

t = 200 s

t = 300 s

t = 350 s

Figure 5.10
Snapshots of the dynamic binding of SC beads with B4F. B4F reaches the diverging element at $t \cong 200$ *s.*

The same experiment was repeated using the same parameters and chemicals but with a concentration of 1 μM of B4F. The plot of Figure 5.11 shows the evolution of the fluorescence versus time due to the molecules of labelled biotin bound to the streptavidin. The pixel mean intensity reported as a function of time was measured using Corel Photopaint, in a 50 μm^2 window located at the entrance of the diverging element of the trapping channel. This method allows a rapid estimate of the dynamic binding time, t_{db}, for the biotin-streptavidin solid-phase reaction to be completed. The data of the graphic indicate that streptavidin, immobilized on bead surfaces, is all bound to B4F after $t_{bd} \cong 30$ s. Even if these results are somewhat qualitative (due to the detection method used), the t_{db} for 1 µM B4F seems to be significatively faster than in the case of 200 nM B4F.

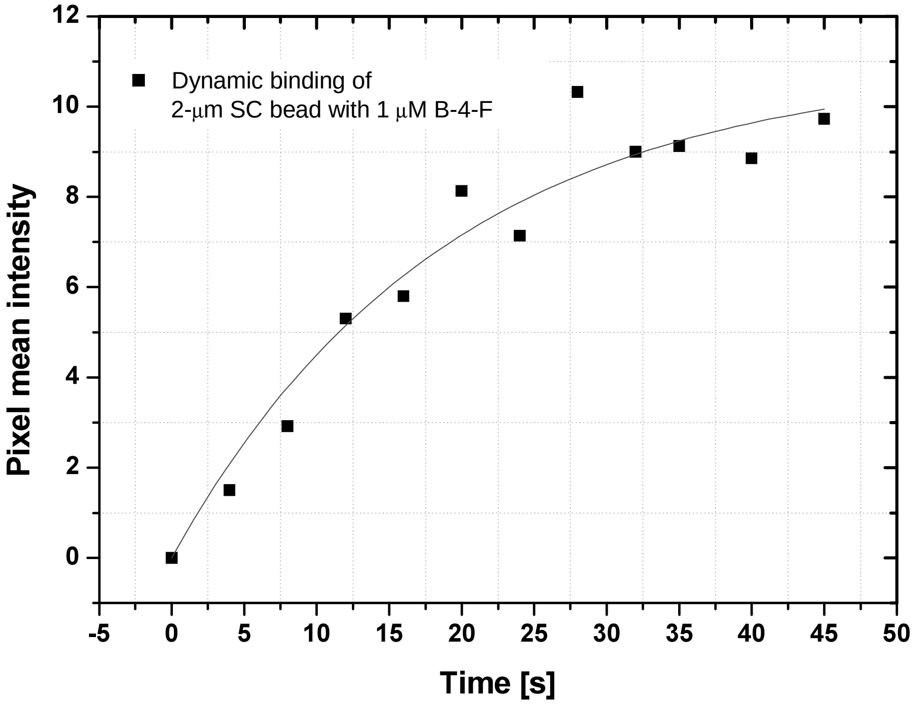

Figure 5.11
Pixel mean intensity, corresponding to fluorescent signal emitted by biotinylated fluorescein bound to SC bead, as a function of time.

The most important point demonstrated by these experiments, is that the heterogeneous assay can be achieved without using physical barriers or additional transducers to trap the beads and, at the same time, to flush samples over them. The freely moving beads, confined in the trapping channel, are actually continuously perfused with either the buffer or with the ligand. These video images confirm perfusion of beads. They represent the first visual example of this phenomenon reported in the literature.

In order to have an estimate of k_f and S_0, the dynamic binding of 2-µm SC beads with fluorescently labelled biotin was also monitored using the LIF system described in Chapter 2.

5.4.2 Dynamic Binding of Biotin to SC Beads using a LIF Detection

Binding experiments similar to the previous section and described in Section 5.3 were carried out using the LIF detection system described in Chapter 2. Figure 5.10 shows the fluorescence signal recorded by the PMT, located at the diverging element of the trapping channel, as a function of time. The device SB1 was used in this case in the pressure-loading mode. The concentration of FLB was set at 50 nM, Δp at 1.26 kPa (12.6 cm) and E_{ave} at 200 V/cm. The 2-μm SC beads were used as the solid-phase. The binding curve of Figure 5.12 can be divided in four sections. The first section, between 0 and 175 s, correspond to the signal due to the trapped SC beads, recirculating at the diverging element of the trapping channel. The difference in signal intensity recorded with the PMT-based system when beads are present and absent is negligible (not shown). At about 190 s the signal recorded starts to increase: the 50 nM FLB reaches the detection window while the beads are still recirculating. Under the Δp and E_{ave} mentioned above, the FLB takes about 175 s to travel from its reservoir up to the trapping channel, a length of 3.6 cm. This corresponds to an average flow rate of about 0.16 nL/s. Between 175 s and 260 s, the FLB mixes with the freely recirculating SC beads. This can be seen by the increase of fluorescence signal due to the newly bound SC bead/FLB complex. The signal intensity reaches a maximum at about 230 s. This signal intensity is due to both bound and unbonds FLB. Between 230 s and 260 s, the fluorescent signal is maximum and stays constant. The noise of the signal is certainly due to the continous movement of the fluorescent beads through the detection window. This section of the plot, between 175 s and 260 s, corresponds to perfusion of the beads by FLB. The third section, between 260 s and 295 s, corresponds to the flushing of the beads with buffer to remove the unbound FLB. However, during this time, the mixing of FLB and SC beads continues. The incubation time thus should include both FLB loading and flushing phases. In this particular case, the incubation time was 120 s. The last part of the graphic yields the signal due to the newly bound FLB/SC bead complex. This fluorescent signal decreases exponentially as a result of photobleaching of the fluorescein when continuously illuminated with laser light. The plot in Figure 5.10 shows the lowest FLB concentration considered with this system, 50 nM. The signal-to-noise ratio in this particular case was 3.3. In order to construct dose-response curves and to determine the forward rate constant as well as the initial number of binding sites, the signal of the FLB/SC bead complex is averaged over 20 s. The rectangle in Figure 5.12 indicates the region where fluorescent signal was averaged in this case.

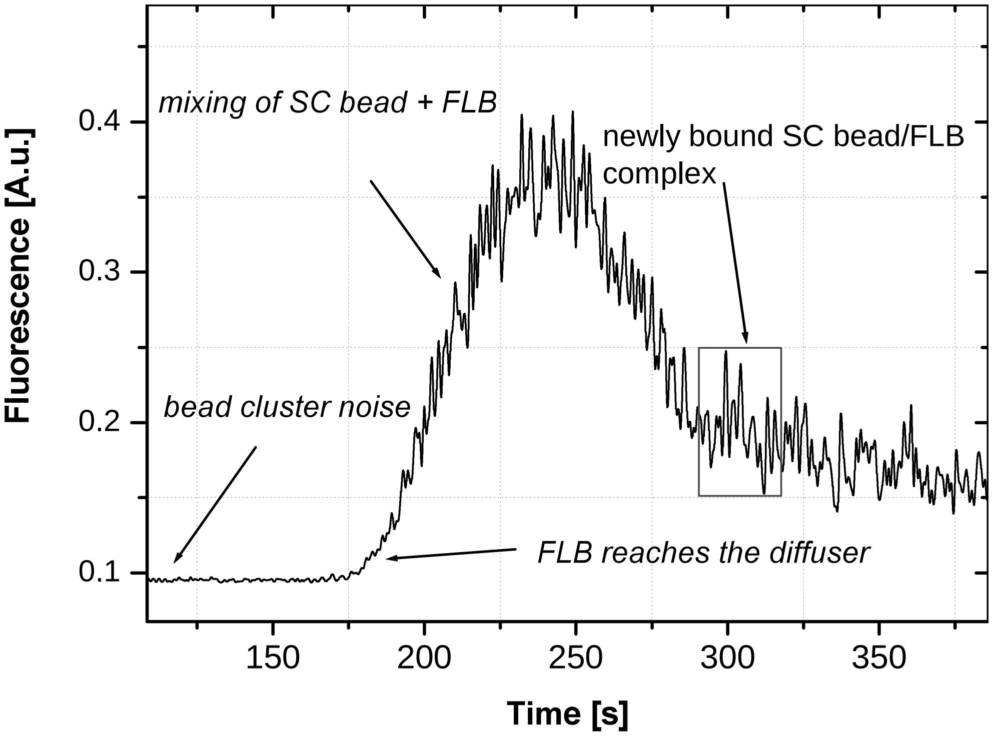

Figure 5.12
Graphic showing a complete analysis from incubation to flushing for 50 nM FLB.

For each measurement involving the EOF-based bead loading of next section, the beads were loaded for 60 s from R_2 by applying an electric field, E, of 290 V/cm. This ensures that the newly bound SC bead/biotin complex concentration remains constant during all experiments ($c_{beads} \cong 10^8$ beads/mL). This is important, since different concentrations of trapped SC beads can result in different values of detected fluorescence for a given concentration of B4F or incubation time. This is illustrated in Figure 5.13, which shows the fluorescent signal as a function of time for 1-µm PA beads recirculating at the diverging element of the trapping channel of SB1. By increasing the applied potential, the size of the bead cluster is reduced, which leads to an increased bead concentration in the detection window. Consequently, the detected fluorescent signal increases. The fluorescent signal intensity of the 1-μm beads is close to the reference when operating conditions are such that no recirculating flows are generated.

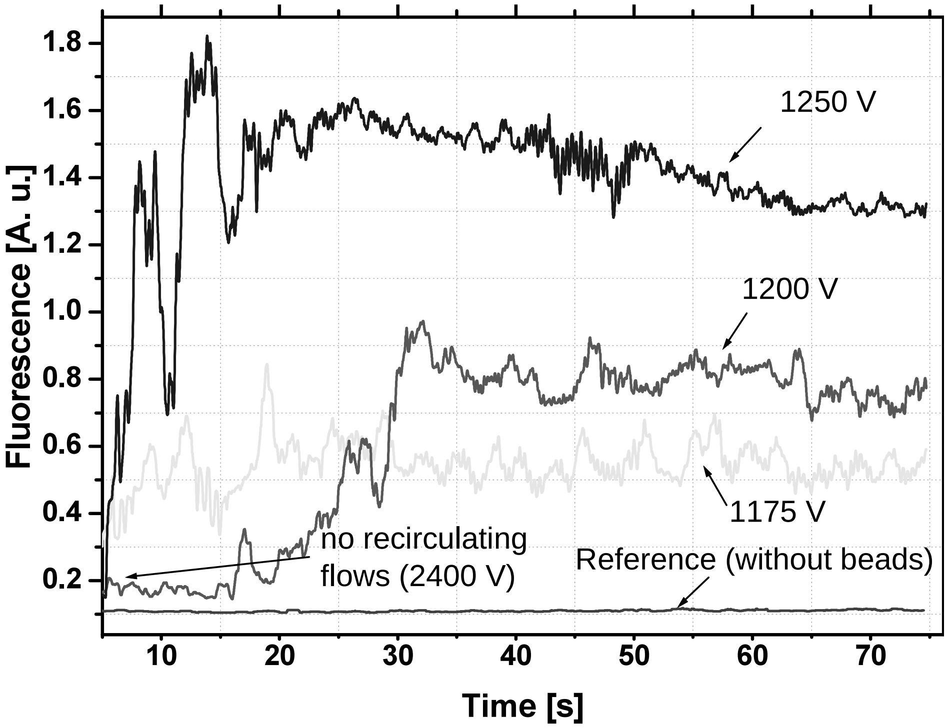

Figure 5.13
Fluorescence signal recorded in a cluster of freely moving, 1-μm Protein A-coated fluorescent beads at a diffuser element for potentials ranging from 1.175 kV to 1.250 kV. The higher the potentials, the more concentrated are the beads, leading to a larger fluorescent signal. When the flow is unidirectional (2400 V, EOF overcomes PF), the fluorescent signal is definitely lower than in the cases where recirculating flows are generated. The signal was filtered using a digital FFT filter in Origin 6.1 (OriginLab Corporation, MA, USA)

5.4.3 Characterization of SC Bead/Biotin Dynamic Binding

The dynamic binding of SC beads with biotin was quantified using a PMT-based detection system. Figure 5.14 shows the fluorescence signal recorded by the PMT, located at the second diverging channel of SB1, as a function of time. In this case, the device was operated in the pressure loading mode. The signal shown was acquired after excess B4F had been flushed away with buffer, and thus is due to the newly bound, biotin-streptavidin-coated beads still recirculating in the trapping channel. The experiments yielding the results in Figure 5.14 each used a sample perfusion, or incubation, time of 200 s, with a total cycle time of 400 s. The lowest concentration of B4F considered was 0.4 μM.

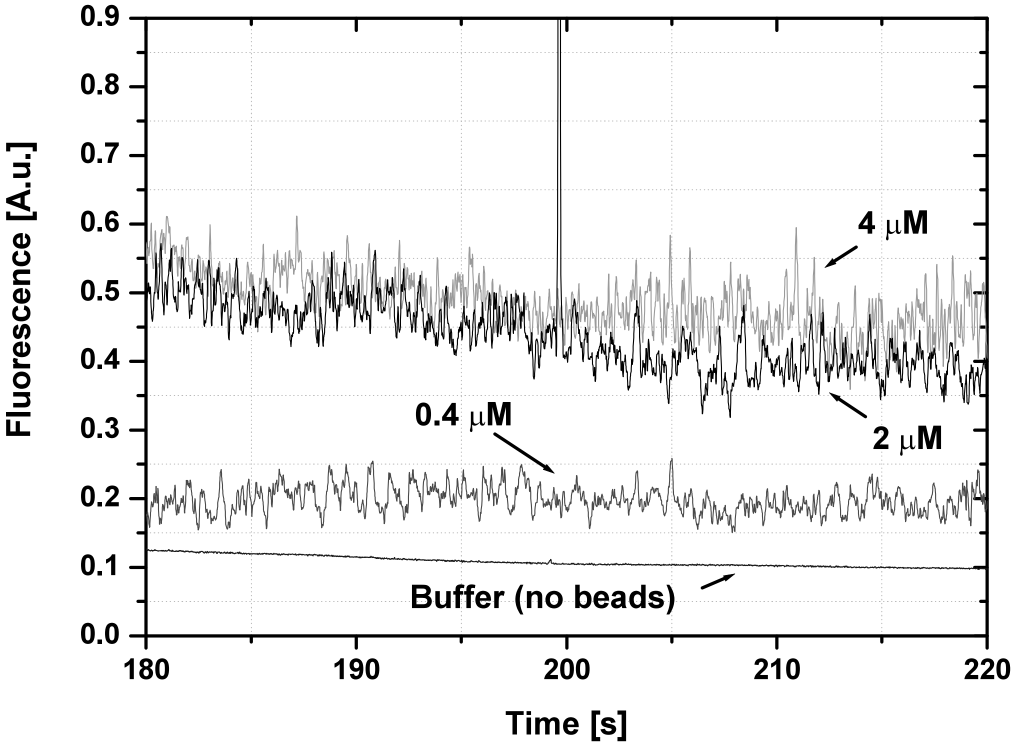

Figure 5.14

Binding curves for biotin bound to SC beads after flushing away excess biotin, obtained in SB1. A significant difference in intensity is observed for B4F-bound beads with respect to pure buffer, indicating that binding did take place. The perfusion or incubation time was 200 s, for a total cycle time of 400 s for each analyte concentration.

Comparison of signal intensities recorded for beads with that for buffer alone indicates that binding did indeed take place. Moreover, the measured fluorescence increased as a function of B4F concentration, allowing a preliminary dose-response curve to be constructed by averaging the signal at each concentration over 50 s (Figure 5.15).

The curve of Figure 5.15 is very typical of analysis based on affinity binding. As the concentration of B4F increases the number of occupied sites increases too. As a result, the fluorescent signal increases until all available streptavidin sites on the beads become occupied. For example, in Figure 5.15, the available streptavidin sites are more or less saturated in 200 s by B4F at a 2-μM concentration.

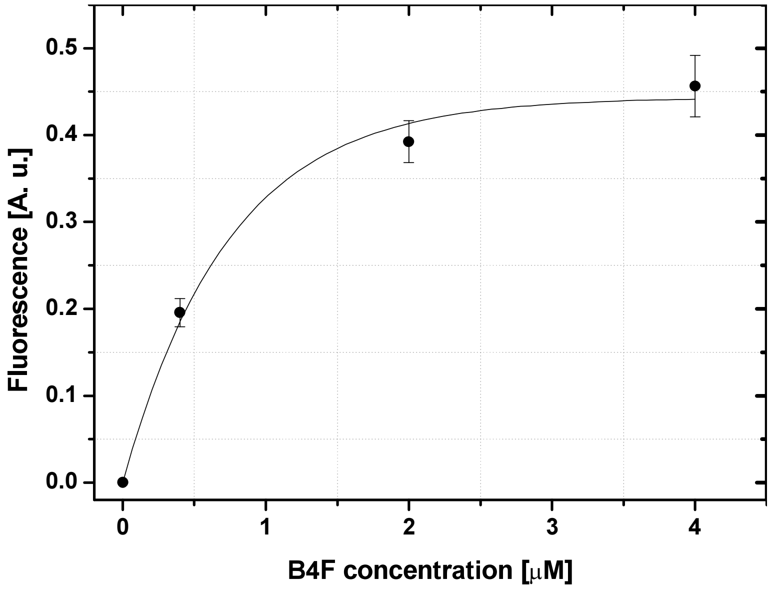

Figure 5.15
A dose-response curve (fluorescence signal as a function of biotin concentration) was constructed from the data of Figure 5.14. Non-linear fitting was added to emphasize the saturation of the available streptavidin sites by the biotin.

The data plotted in Figure 5.16 shows a dose-response curve for lower concentrations of B4F. In this case, the SB2 device was used to perform the experiment in the EOF bead loading mode. The incubation time was set at 150 s and concentrations of B4F ranged from 50 nM to 600 nM. As expected, for a lower incubation time and lower concentration than for the data of Figure 5.15, saturation of the available streptavidin sites is not reached. The graphic of Figure 5.16 verifies that the relation between B4F concentration and fluorescence signal emitted by the SC bead/B4F complex is linear at low concentrations.

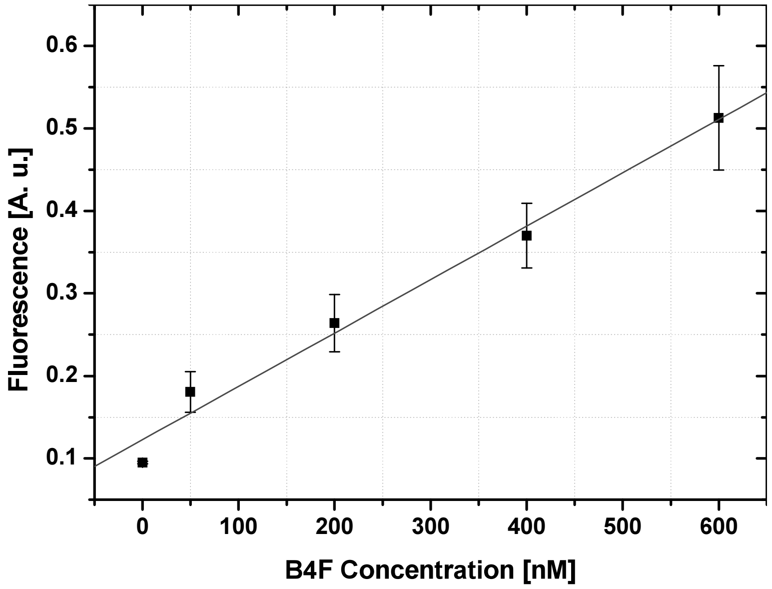

Figure 5.16
A dose-response curve for B4F concentration ranging from 50 nM to 600 nM obtained with SB2. The incubation time was 150 s.

5.4.4 Kinetics of SC bead/B4F binding

The plots in Figure 5.17 illustrate the fluorescence signal recorded with the PMT as a function of incubation time for [FLB] = 250 nM and 500 nM.

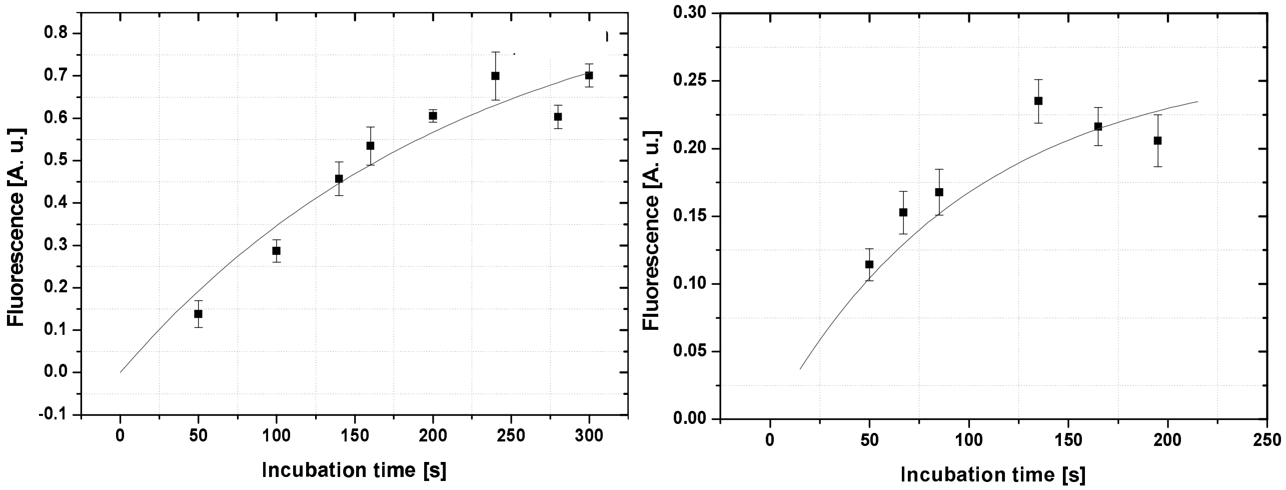

Figure 5.17
Fluorescence signal as a function of incubation time obtained with (a) 250 nM FLB and (b) 500 nM FLB. The curves are calculated using a 1^{st}-order binding model.

The data were obtained using SB2, operating at a Δp = 1.26 kPa and at E_{ave} = 180 V/cm. The flow rate of FLB, loaded up to the trapping channel by electro-osmotic pumping, was about 0.16 nL/s. The initial concentration of beads, C_i, present in R_2,was about 2 x 10^8 beads/mL in the case of Figure 5.17 *(a)* and 5 x 10^8 beads/mL in Figure 5.17 *(b)*. In both cases, the beads were loaded for 40 s at 540 V/cm. The solid lines of this figure were fit according to Eq 5.6.

As for the dose-response curves discussed in the previous section, the incubation is carried out in a flowing stream. The amount of bound biotin will depend on the number of available streptavidin binding sites on the beads and the amount of solution flushed over the beads. The longer the incubation time, the more sites will be occupied and the higher the signal will be, as shown in Figure 5.17. At some point, saturation of the binding sites will occur, corresponding to a maximum signal. The plots in Figure 5.17 show that the signal approaches saturation after 300 s in (a) and 150 s in (b). This could be due to the higher concentration of FLB or the greater availability of streptavidin sites, or both.

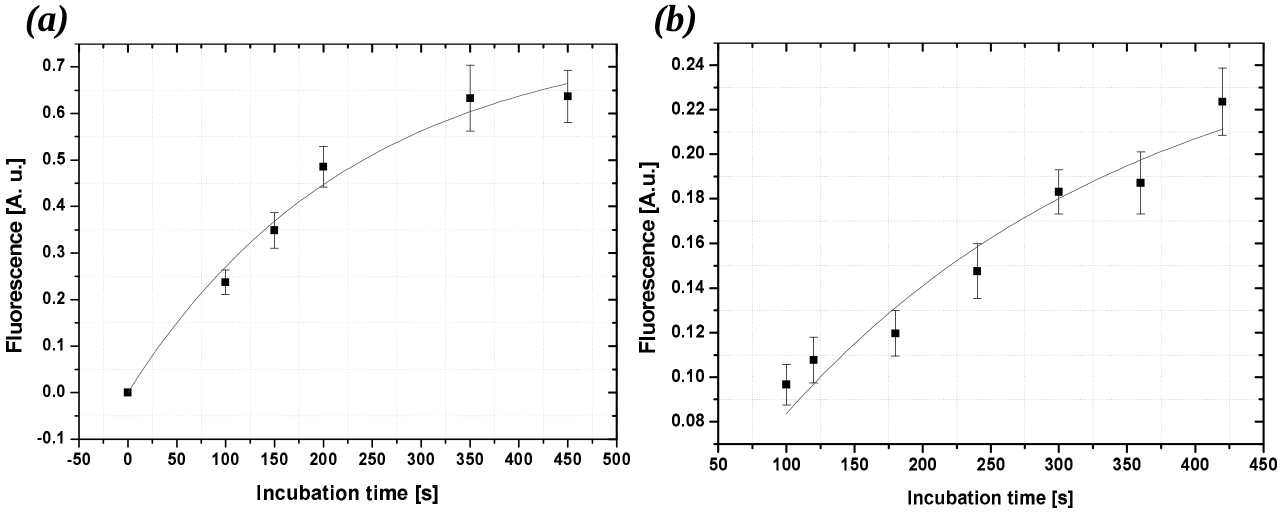

Figure 5.18

Fluorescence signal as a function of incubation time obtained with 1 μM and 0.8 μM B4F. The curve is calculated using a 1^{st}-order binding model.

[FLB][μM]	**[B4F]**[μM]	**C$_i$** [beads/mL]	Q_{biotin} [nL/s]	k_f [M^{-1}]
0.25	-	5 x10^8*	0.16	***15000***
0.25	-	5 x10^8*	0.16	***18000***
0.25	-	1.4 x10^8*	0.16	***32000***
0.5	-	2 x10^8*	0.16	***29000***
-	1	1.5 x10^8	0.07	***4500***
-	2	2 x10^8	0.07	***2500***
-	0.8	2 x10^8	0.07	***4700***

Table 5.1
Summary of values for the forward rate constant extracted from curves fit to different data sets, for different concentrations of FLB and B4F. The 2-μm SC beads used for FLB (*) and for B4F measurements came from two different batches. For each measurement, obtained with SB2, the bead loading time (40 s) and the corresponding E_{ave} *(540 V/cm) were kept constant.* Q_{biotin} *is the biotin flow rate during the incubation.*

Fluorescence signal as a function of the incubation time were also obtained for B4F, as shown in Figure 5.18, using the same device (SB2). In Figure 5.18, [B4F] = 1000 nM and C_i = 1.5 x 10^8 beads/mL while in Figure 5.18 (b), [B4F] = 800 nM and C_i = 2 x 10^8 beads/mL. The same E_{ave} and bead loading time as for FLB were used. On the other hand, the B4F was loaded at a lower flow rate, 0.07 nL/s.

The binding of biotin to the SC beads is described by Eq 5.6. By fitting the data using the function given by Eq 5.6., values of k_f and S_0 were obtained. The data corresponding to Figure 5.17 and Figure 5.18 are reported in Table 5.1 and Table 5.2 together with data obtained in other experiments performed in the same way with SB2.

Several conclusions about the forward rate constant emerge from Table 5.1. First, it can be observed from the data of Table 5.1, that the values of k_f are significantly different for FLB and B4F for binding with SC beads. For FLB, the average value of the forward rate constants is $\bar{k}_f = 23500 \pm 8267$ M^{-1} whereas for B4F, $\bar{k}_f = 3900 \pm 1217$ M^{-1}. The value for FLB is 6-fold larger than for B4F. Second, it can be noticed from the data of Table 5.1, that the k_f are substantially lower, 3 to 4 orders of magnitude, than the reported 10^7 for the streptavidin-biotin interaction in solution [10]. There are only a few studies in which the focus has been the interaction between biotin in the solution phase and streptavidin on a solid phase. In these studies, it was found that the forward constant of the streptavidin-biotin bond was smaller on surfaces than in solutions [10, 11]. According to [10, 11], the initial forward reaction often becomes limited at the interface, possibly due to steric hindrance and the inflexibility of immobilized ligand. On the other hand, the dissociation rate of the bound molecule is often faster than that characteristic of the complex in the solution. This is a result of surface-induced conformational shifts in the binding sites presented by the immobilized molecules. Thus, both the forward and the reverse reactions tend to reduce the magnitude of the binding constant. In their study, Huang et al. [10], reported values of k_f ranging between 10^3 M^{-1} to 10^6 M^{-1} for the binding between chains of biotinylated DNA (100-5000 bp) to 1-μm SC beads. They also showed that k_f decreased as the bead size increased or when the chains of DNA were longer. In our case, the beads were always of the same diameter, i.e. 2 μm. Because FLB is a larger molecule than B4F, it is somewhat surprising that it binds more readily with the SC beads. Intuitively, one would assume that binding of FLB to streptavidin would be more stericly hindered, due to its larger size. However, a possible explanation could involve the extra conformational freedom that the 21-atom spacer imparts to the FLB molecule. This could allow the biotin more freedom to bind without steric interface from the dye moiety.

The parameters S_0 (see Table 5.2) give an estimate of the number of biotin-binding sites initially available on the SC beads present in the trapping channel. From the fits, S_0 has units of Volts·second, which should be converted into a number of molecules. To calculate this, the conversion factor for fluorescence signal in V to number of fluorescent molecules was first determined [15]. The flow rate of the biotin (Q_{biotin}) during incubation was about 0.16 nL/s for FLB and 0.07 nL/s for B4F. These flow rates were measured with the PMT-based system, by measuring the time necessary for the biotin to reach the trapping channel under condtions where SC beads are trapped. Thus, the number of molecules per second is given by:

$$N = N_A Q_{biotin}\,[\text{FLB or B4F}] \qquad \textbf{Eq 5.7}$$

where N_A is Avogadro's number and Q_{biotin} the biotin flow rate during incubation. For example, for Q_{biotin} = 0.16 nL/s and [FLB]= 0.25 µM, N = 2.4×10^7 molecules/s. Integrating the incubation signal over 1 second, an area of 0.2 V·s is obtained in this particular case. Unit signal area (u.s.) is then 1.2×10^8 molecules/Vs. Converting, then, S_0 obtained from a kinetic fit of the data is equivalent to 10.8×10^7 molecules of FLB. This value corresponds to the number of available biotin sites on the SC beads (N_{sites}). The values of S_0, N, u.s., N_{sites} as well as Q_{biotin} and C_i, are reported in Table 5.2.

[FLB]	**[B4F]**	C_i	Q_{biotin}	N^1	S_0	**u.s.**^{2}	N_{sites}^3
[µM]	[µM]	[beads/mL]	[nL/s]	[molec./s]	[Vs]	[molec./Vs]	[sites]
		$\times 10^8$		$\times 10^7$		$\times 10^8$	$\times 10^7$
0.25		5*	0.16	2.4	0.90	1.2	10.8
0.25		5*	0.16	2.4	1.20	0.8	9.9
0.25		1.4*	0.16	2.4	0.39	0.7	2.9
0.5		2*	0.16	4.8	0.25	1.4	3.5
	1	1.5	0.07	4.2	0.96	0.3	3.2
	2	2	0.07	8.4	0.63	0.6	3.9
	0.8	2	0.07	3.4	0.23	1.7	3.9

[1]: number of available ligand molecules perfusing the trapped beads at a flow rate Q_{biotin}.

[2]: unit signal, extracted from the experiments, used to convert S_0 into number of available biotin binding sites

[3]: number of calculated available biotin binding sites on the beads ($N_{sites} = S_0 \times$ u.s.)

Table 5.2

Summary of values for kinetic parameters extracted from curves fit to different data sets, for different concentrations of FLB and B4F. The 2-µm SC beads used for FLB (*) and for B4F measurements came from two different batches. For each measurement, obtained with SB2, the bead loading time (40 s) and the corresponding E_{ave} *(540 V/cm) were kept constant.*

The data of Table 5.2 shows that the higher the C_i, the higher is the number of available biotin sites, as expected. It is important to emphasize that the higher the C_i, the larger the number of beads will be present in the holding reservoir and therefore, the larger the number of beads will be trapped and preconcentrated.

[FLB] [μM]	**[B4F]** [μM]	$\boldsymbol{S_0}$ [Vs]	$\mathbf{N_{sites}}$ [sites] x10^7	**N** [molec./s] x10^7	t_{sat}[1] [s]	$N_{bio, TOT}$[2] [molec.] x10^{10}	$N_{sites, TOT}$[3] [molec.] x10^{10}	n_{beads}[4] [beads]	$\varphi = N_{sites,TOT}/N_{bio,TOT}T$
0.25		0.90	10.8	2.4	350	3.8	1.4	113	**37%**
0.25		1.20	9.9	2.4	350	3.5	1.3	105	**38%**
0.25		0.39	2.9	2.4	400	1.2	0.4	33	**35%**
0.5		0.25	3.5	4.8	300	1.1	0.5	40	**48%**
	1	0.96	3.2	4.2	500	1.6	0.4	33	**20%**
	2	0.63	3.9	8.4	500	2	0.5	40	**26%**
	0.8	0.23	3.9	3.4	550	2.2	0.5	40	**24%**

[1]: *time where full occupation of binding sites is assumed*
[2]: *total number of labeled biotin molecules passing over the beads* ($N_{bio, TOT} = N \cdot t_{sat}$)
[3]: *number of available binding sites passing under the detection volume* ($N_{sites, TOT} = N_{sites} \cdot V_{TC}/V_D$)
[4]: *number of 2 μm SC beads, in the detection volume* ($n_{beads} = N_{sites, TOT}/n_{bs}$)

Table 5.3
Values calculated from the data extracted from curves fit to different data sets, for different concentrations of FLB and B4F (see Table 5.1 and Table 5.2).

To have an idea of the efficiency, φ, of the system, the ratio between the number of available binding sites ($N_{sites, TOT}$) passing under the detection volume ($V_D \cong 0.01$ nL) and the total number of labeled biotin passing over the beads ($N_{bio, TOT}$), was calculated for each concentration of FLB and B4F in Table 5.2. The results are summarized in Table 5.3. The values of $N_{bio, TOT} = N \cdot t_{sat}$, where t_{sat} is the time (extracted from the fitting curves calculated with Eq. 5.6) where full occupation of binding sites is assumed (saturation of the available binding sites). The values of $N_{sites, TOT} = N_{sites} \cdot V_{TC}/V_D$, where V_{TC} is the volume of the trapping channel ($V_{TC} \cong 4$ nL). In

Table 5.3, the number of beads, n_{beads}, in the V_D was also included. The values of $n_{beads} = N_{sites,\ TOT}/n_{bs}$, where n_{bs} is the number of sites per bead calculated from the binding capacity of the beads provided by the manifacturer ($n_{bs} \cong 1.24 \times 10^8$ sites/bead).The efficiency of the binding is on average 40 % for FLB and 23 % for B4F. These values show that at saturation, not all the sites are occupied. This may due again to steric hindrance. On the other hand, the values of φ for FLB are two times larger than for B4F, which is in agreement with respect to the k_f. The determination of the efficiency in reagent usage is essential if biotin-streptavidin coupling is to be used as a base for immobilization of antibodies for immunology or for molecular biology applications.

5.5 Conclusions

A microfluidic system using fluid flows only to trap beads was successfully used to perform the dynamic binding of SC beads with two different types of biotinylated molecules. The method used to perform this dynamic binding is new and does not require physical barriers or additional transducers to trap the beads. Beads are caught in steady and controllable recirculating flow patterns established in the trapping channel by opposing an EOF and a PF. The efficiency of the trapping channel depends on μ_{EOF}, μ_{beads}, Δp and the geometry of the trapping channel.

The concept of trapping using fluid flows only allows the four basic steps for doing a heterogeneous assay on-chip to be performed. It was demonstrated that freely moving clusters of beads, trapped in the trapping channel, can be perfused by different solutions loaded from different reservoirs and driven by EOF. Once the mixing and chemical reactions between a liquid and a solid-phase are achieved with this technology, the beads are flushed simply by removing one of the two fluid flow components. Alternatively, one flow rate can be increased to the extent that bi-directional flow ceases to exist.

Quantitative and qualitative measurements of the dynamic binding of 2-µm SC beads and fluorescently-labelled biotin were achieved using a PMT-based detection system and a fluorescent microscope, respectively. Using the latter apparatus, the dynamic binding was observed in real time, demonstrating the feasibility for doing bead-based assay on-chip. Dose-response curves and calibration curves were constructed for B4F and FLB with the PMT-based detection system. The lowest concentration detected with this system was 50 nM FLB. The forward rate onstant of the interaction streptavidin/biotin, as well as the binding capacity of the beads, were extracted from the experiments and compared with theoretical values. As reported in other studies, the forward rate constant for the heterogeneous assay is lower by 3 (FLB) to 4 (B4F) orders of magnitude compared to the forward rate constant for homogeneous systems (10^7 [11]). Effects of steric hindrance appear to be one cause for these differences. A significant difference of the forward rate constant between FLB ($\bar{k}_f$ = 23500 M^{-1}) and B4F ($\bar{k}_f$ = 3900 M^{-1}) was observed. The efficiency of the binding, an important paramater for the extension of this system to an immunoassay, was estimated for several concentrations of the two types of biotin. Average efficiencies of 40 % for FLB and 23 % for B4F were obtained, which are good results for this kind of binding.

5.6 References

[1] G. Boer, A. Dodge, K. Fluri, B. H. van der Schoot, E. Verpoorte, and N. F. de Rooij, "Studies of hydrostatic pressure effects in electrokinetically driven µTAS," in *Micro Total Analysis Systems '98: Proceedings of the µTAS'98 Workshop*, D. J. Harrison and A. van den Berg, Eds. Dordrecht: Kluwer Academic Publishers, 1998, pp. 53-56.

[2] G. Lettieri, A. Dodge, G. Boer, J. Lichtenberg, E. Verpoorte, and N. F. de Rooij, "Consequences of opposing electrokinetically and pressure-induced flows in microchannels of varying geometries," presented at Micro Total Analysis Systems 2000: Proceedings of the µTAS 2000 Symposium, Enschede, The Netherlands, 2000.

[3] G.-L. Lettieri, E. Verpoorte, and N. F. de Rooij, "Planar microfluidic devices for controlled vortex generation," presented at Transducers'01 Eurosensors XV, Munich, Germany, 2001.

[4] G.-L. Lettieri, E. Verpoorte, and N. F. de Rooij, "Affinity-based bioanalysis using freely moving beads as matrices for heterogeneous assays," in *µTAS 2001, Micro Total Analysis Systems 2001: Proceedings of the µTAS 2000 Symposium*. Monterey, California: Kluwer Academic Publishers, 2001, pp. 503-504.

[5] M. B. Meza, "Bead-based HTS applications in drug discovery," *Drug Discovery Today*, vol. 1, pp. 38-41, 2000.

[6] E. P. Diamandis and T. K. Christopoulos, *Immunoassay*. San Diego, CA: Academic Press, 1996.

[7] N. Dontha, W. B. Nowall, and W. G. Kuhr, "Generation of biotin/avidin/enyme nanostructures with maskless photolithography," *Anal. Chem.*, vol. 69, pp. 2619-2625, 1997.

[8] Y. L. e. a. Wang, "Implications for the developement of dynamically modified optical-fiber sensors," *Anal. Chim. Acta*, vol. 298, pp. 105-112, 1994.

[9] M. Haun and S. Wasi, "Biotinylated antibodies bound to streptavidin beads: a versatil solid matrix for immunoassays," *Anal. Biochem.*, vol. 191, pp. 337-342, 1990.

[10] S.-C. Huang, H. Swerdlow, and K. D. Caldwell, "Binding of biotinylated DNA to streptavidin-coated polystyrene latex," *Analytical Biochemistry*, vol. 222, pp. 441-449, 1994.

[11] V. H. e. a. Perez-Luna, "Molecular recognition between genetically engineered streptavidin and surface-bound biotin," *J. Am. Chem. Soc.*, vol. 121, pp. 6469-6478, 1999.

[12] C. Stamm and W. Lukosz, "Integrated optical Difference interferometer as biochemical sensors," *Sensors and Actuators B*, vol. 18-19, pp. 183-187, 1994.

[13] S. M. Hedrick, D. I. Cohen, E. A. Nielsen, and M. M. Davis, *Nature*, vol. 308, pp. 149-153, 1984.

[14] S.-C. Huang, S. M. D., W. R., and K. D. Caldwell, "Binding of biotinylated DNA to streptavidin-coated polystyren latex: effects of chain length and particle size," *Analytical Biochemistry*, vol. 237, pp. 115-122, 1996.

[15] A. Dodge, K. Fluri, E. Verpoorte, and N. F. de Rooij, "Electrokinetically driven microfluidic chips with surface modified chambers for heterogeneous immunoassays," *Analytical Chemistry*, vol. 73, pp. 3400-3409, 2001.

6 On-Chip Molecules Preconcentration employing the Recirculating Flows

6.1 Introduction

Beads are trapped when all three contributions to beads velocity (μ_{EOF}, μ_{bead} and Δp) lead to zero bead velocity. Hence, the E and Δp conditions under which beads are trapped are very much dependent on μ_{beads}. This suggests that other species could also be trapped, with each species having different E and Δp. This chapter considers this phenomenon to investigate the trapping of DNA molecules (section 6.2) and small biomolecules (section 6.3). The DNA trapping was inspired by the study of Takamura et al. [1] presented at the µTAS 2002 Conference held in Kyoto (Japan). Despite the resemblance with the trapping method developed in this thesis, it is still unclear how their system works to trap the DNA. Moreover, they use 0.5 µm-deep x 0.6 µm- 5 µm wide tapered channels, which is quite different from our system.

Observation with a fluorescence microscope (FM) shows that λDNA molecules follow the streamlines in the same way as beads. The molecules of λDNA recirculate and preconcentrate in the trapping channel. Boundary conditions (hydrostatic pressure and electric field) for λDNA trapping are different from all beads used (e.g. SC beads, Protein A-coated beads, carboxylate-modified beads, etc…). This is due to the relatively large observed difference between the apparent electrokinetic mobility of the beads and λDNA. Therefore, λDNA could be selectively trapped and concentrated under conditions where other substances would have flowed out of the trapping channel. This selective trapping of DNA could be relevant for on-chip DNA extraction and concentration from mixtures of other substances, and for on-chip DNA pretreatments (since the trapped DNA can be perfused by solutions in the same manner as beads) [2-4]. After preconcentration, λDNA can be easily released either by increasing or removing the electric field. No problems of clogging are observed.

Preconcentration of smaller molecular species was also investigated, using B4F (M.W. = 644.7 g/mol) as sample. Video imaging using a fluorescence microscope showed that 1-uM B4F, driven by EOF, can be stopped at a nozzle element using a pressure-driven counter flow and preconcentrated. This phenomenon was also observed with a PMT-based detection system [5].

6.2 On-chip DNA Preconcentration

The method presented previously for beads has been successfully used to trap λDNA (48 kbp, 16 μm long) in similar devices. Molecules of λDNA are loaded up to the trapping channel using electro-osmotic pumping and are trapped afterwards by adjusting the applied electric field for a given hydrostatic pressure.

6.2.1 Chip Operation

Trapping and preconcentration of purified λDNA was performed with DC2 and DNA1. The layouts and the dimensions of these devices are presented in Chapter 2. The process to trap and preconcentrate the DNA is very similar to the SC bead trapping introduced in Chapter 5. Because these are preliminary experiments, the operating E and Δp used during these experiments were not optimized.

In DNA1, 1 μM λDNA was loaded into the device from R_5 using EOF. Electric field strength of about 900 V/cm applied for 120 s was required for the molecules of DNA reached the diverging element of the trapping channel. The Δp was set at 0.3 kPa (3 cm of buffer) on R_4 and R_3. To work at lower *E* and load the sample in the same time, it is sufficient to decrease the Δp or to work with a shorter device. Once the molecules of λDNA reached the diverging element, the potential was switched to between R_1 and R_4 and the E decreased from 900 V/cm to 240 V/cm in order to trap and preconcentrate the molecules of λDNA. To flush away the preconcentrated λDNA, the *E* was increased to 500 V/cm.

In SB2, the operating steps were similar to DNA1. 2 μM λDNA was introduced into the device from R1 by electro-osmotic pumping. The counter pressure was set at 0.5 kPa (R_4). The *E* for the λDNA loading was 800 V/cm. When the λDNA reached the diverging element of the trapping channel, the *E* was decreased to 270 V/cm for the preconcentration.

6.2.2 λDNA Preconcentration

The pictures of Figure 6.1 were taken using a fluorescent microscope. They illustrate the trapping and preconcentration of λDNA stained with YOYO1 at the diverging element of the trapping channel. Figure 6.1 (a) and (b) show the loading of the stained DNA in DNA1 from the side channel. The side channel is directly connected to the wide channel located between the 2nd converging element and the 2nd diverging element. It was observed that molecules of DNA change their conformation depending on whether they are loaded or trapped. The molecules of DNA, driven by EOF, tend to be stretched out in the high *E*. Figure 6.1 (c) shows what happens when the *E* field is suddenly decreased. The molecules of DNA stop moving towards R_4 and start recirculating in the trapping channel (Figure 6.1 (d)). When loaded, they are mostly elongated (although a few can form spherical shapes). When they are trapped, the DNA molecules tend to agglomerate at the entrance of the diverging element. In fact, it was observed that molecules of DNA form two symmetrical clusters.

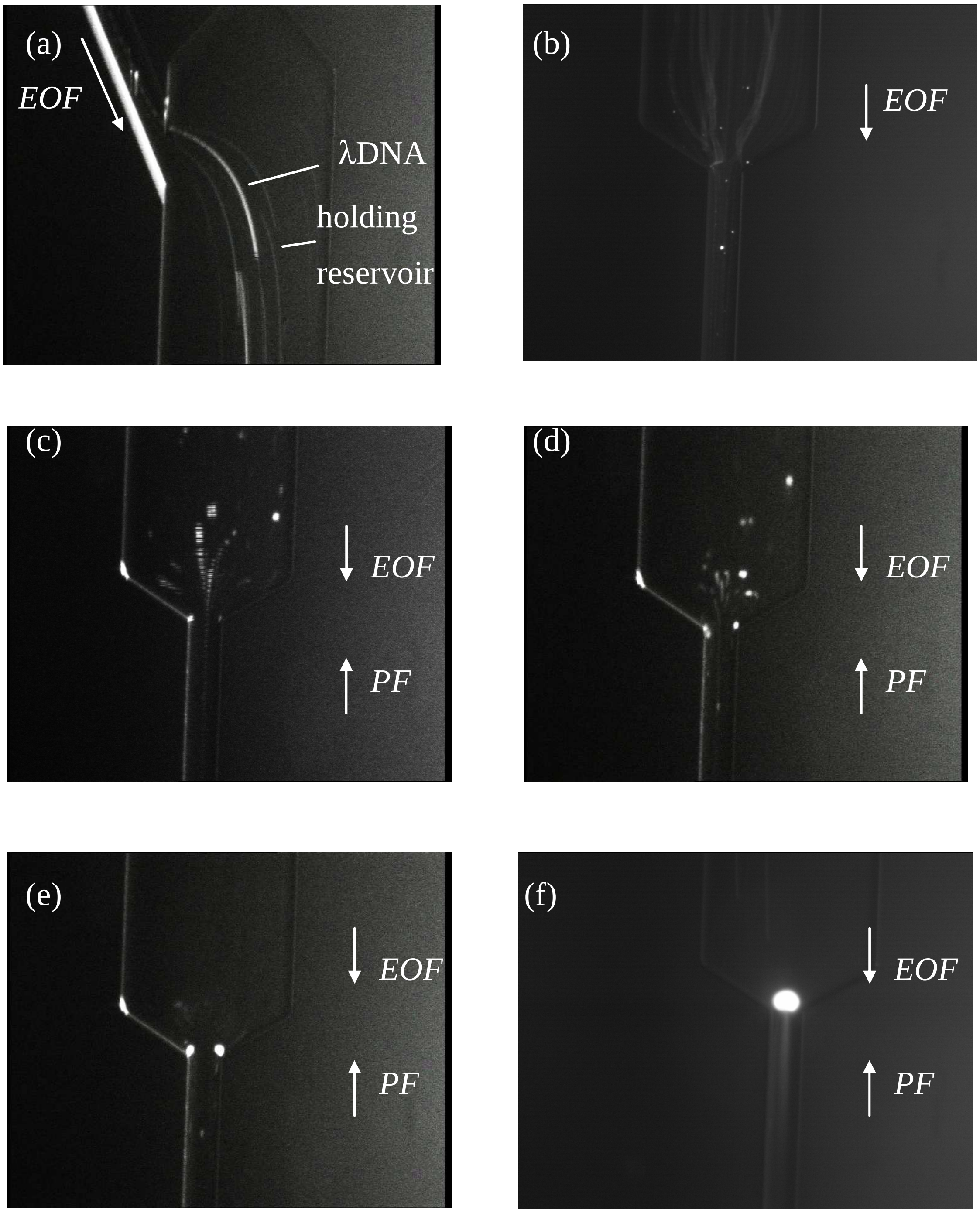

Figure 6.1
Loading and preconcentration of molecules of 1 μM λDNA using recirculating flows. The integration time was set at 2 frames/s. After 25 s from the moment where recirculating flows are generated ((c)), all the DNA present in the holding reservoir is trapped ((f)).

In Chapter 5, simulations showed that at these locations, the velocity distribution of the recirculation is faster, inducing zones of vortex motion. On the other hand, most of the molecules of DNA present in the narrow channel of the trapping channel are elongated. This is illustrated by Figure 6.1 (e). Changes in DNA conformation have been reported by Han and Craighead. They observed that the radius of gyration of the DNA was influenced by the depth of the microchannels which has a direct influence on *E* [6, 7]. In our case, the change of the molecular conformation seems to be correlated with the recirculating flow phenomenon. The size of the two clusters of freely moving molecules of DNA increases until the two clusters merge together. This is illustrated in Figure 6.1 (f). A new cluster of DNA molecules is then generated. This cluster remains stable and the overall experiment is reproducible if the same λDNA loading time and the same operating conditions (*E* and Δp) are used. In fact, it was observed that a too large *E* could induce first the trapping of a certain amount of λDNA, followed by the launching of the cluster towards the narrow channel of the trapping channel. This is shown in Figure 6.2, where *E* is slightly higher than in the previous case (290 V/cm instead of 240 V/cm).

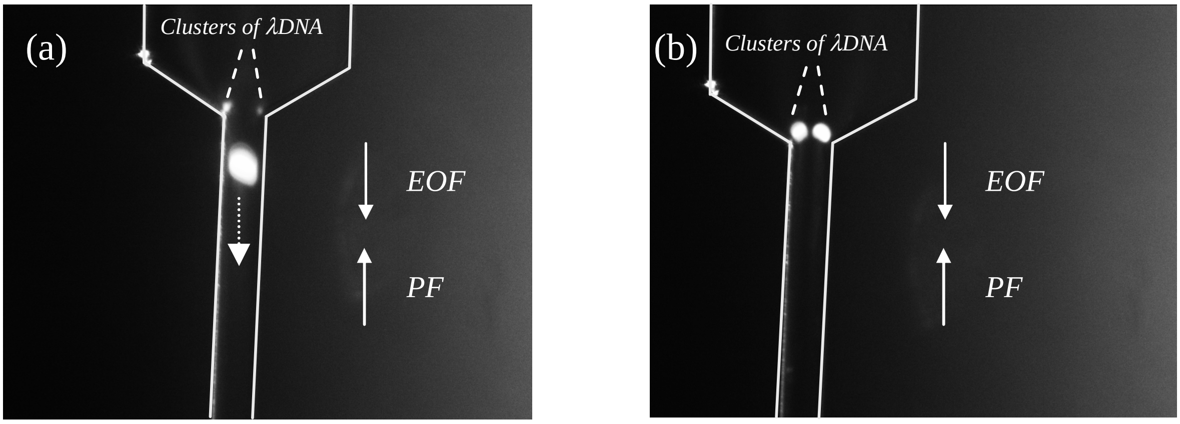

Figure 6.2
(a) λDNA (1 μM) launching, E =290 V/cm and $\Delta p = 0.3$ *kPa (b) Trapping of new 1 μM λDNA coming from the holding reservoir, E =290 V/cm and* $\Delta p = 0.3$ *kPa. The integration time (*t_i*) was set at 2 frames/s.*

It can be seen in Figure 6.2 (a) that when the launching of the DNA cluster occurs, molecules of DNA are still being attracted towards the trapping channel. As the cluster moves away from the diverging element, the generation of two new clusters of DNA can be observed (Figure 6.2 (b)).

Hence, the launching of λDNA molecules seems to depend on the amount of λDNA trapped and on the flow conditions. This is supported by experiments performed with SB2 using an initial concentration of 2 μM λDNA stained with YOYO1. In this case, experiments showed that preconcentration can occur indefinitely, regardless of the size or the amount of λDNA trapped, if the *E* and *Δp* are adequately chosen, as illustrated in Figure 6.3. In this case, the trapping channel is full of DNA. The final number of DNA molecules trapped depends only on the number of molecules present in the holding reservoir.

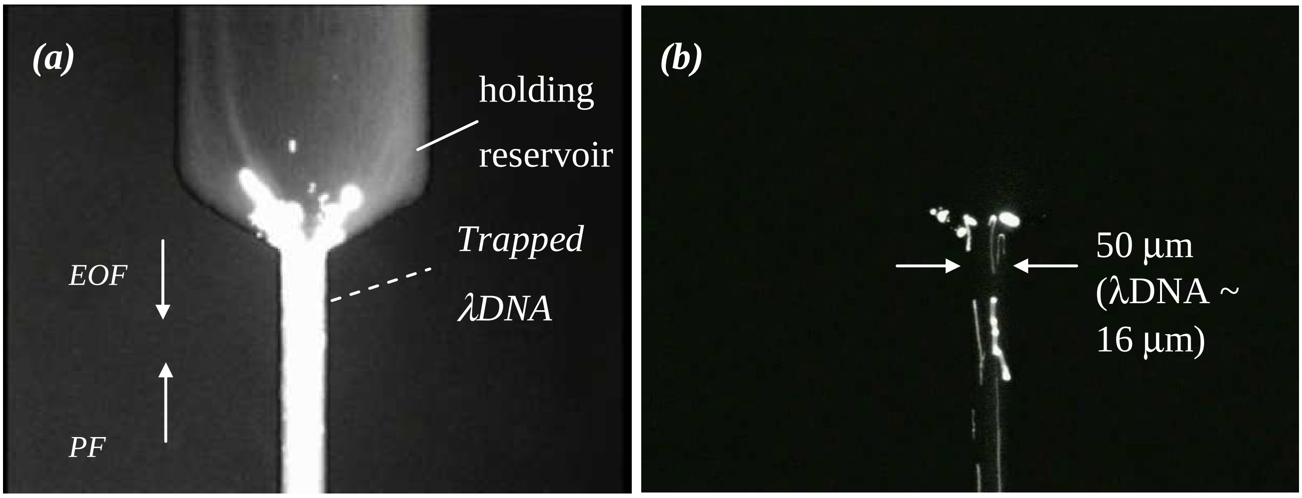

Figure 6.3
(a) Trapping of 2 μM λDNA. t_i *= 10 frames/s, E = 270 V/cm and Δp = 0.5 kPa after 90 s of loading. (b) Trapping of 2 μM λDNA. In this case, the loading time was short enough (15 s) to trap only a few molecules of λDNA.*

Figure 6.2 and Figure 6.3, the overall flow rate is still determined by EOF. In Chapter 4 and Chapter 5, it was observed that recirculating flows are obtained for a range of *E* and *Δp*. For a given *Δp* and trapping channel geometry, there is a range of *E* which results in effective trapping. The trapping of λDNA, in Figure 6.2 was achieved under conditions where the *E* for trapping had a maximum value. In this particular case, only a significant variation of the overall mobility of the λDNA cluster can explain the fact that it escapes the trapping channel. Interestingly, the overall mobility of the λDNA clusters is likely to lower than the mobility of single λDNA molecules if the λDNA clusters escape from the trapping channel. More experiments are required to investigate this phenomenon.

6.2.2.1 DNA Trap and Release

An important requirement for systems that attempt to perform on-chip DNA preconcentration is prevention of channel clogging. In the approach of Han and Craighead, for example, segments of nanochannels are used to preconcentrate and to separate DNA molecules. The risks of clogging are therefore higher in those devices. The microfluidic devices used in this work have minimum widths of 40 μm and minimum depths of about 15 μm. No clogging was observed, even for the preconcentration the 2 μM λDNA of Figure 6.3. The ability to trap and release the DNA simply by turning on and off the E demonstrates this feature. Moreover, this type of experiment shows the potential of this technology to precisely handle molecules of DNA as well as beads (see chapter 3). The trap and release of 1 μM λDNA is shown in Figure 6.4 using DNA1.

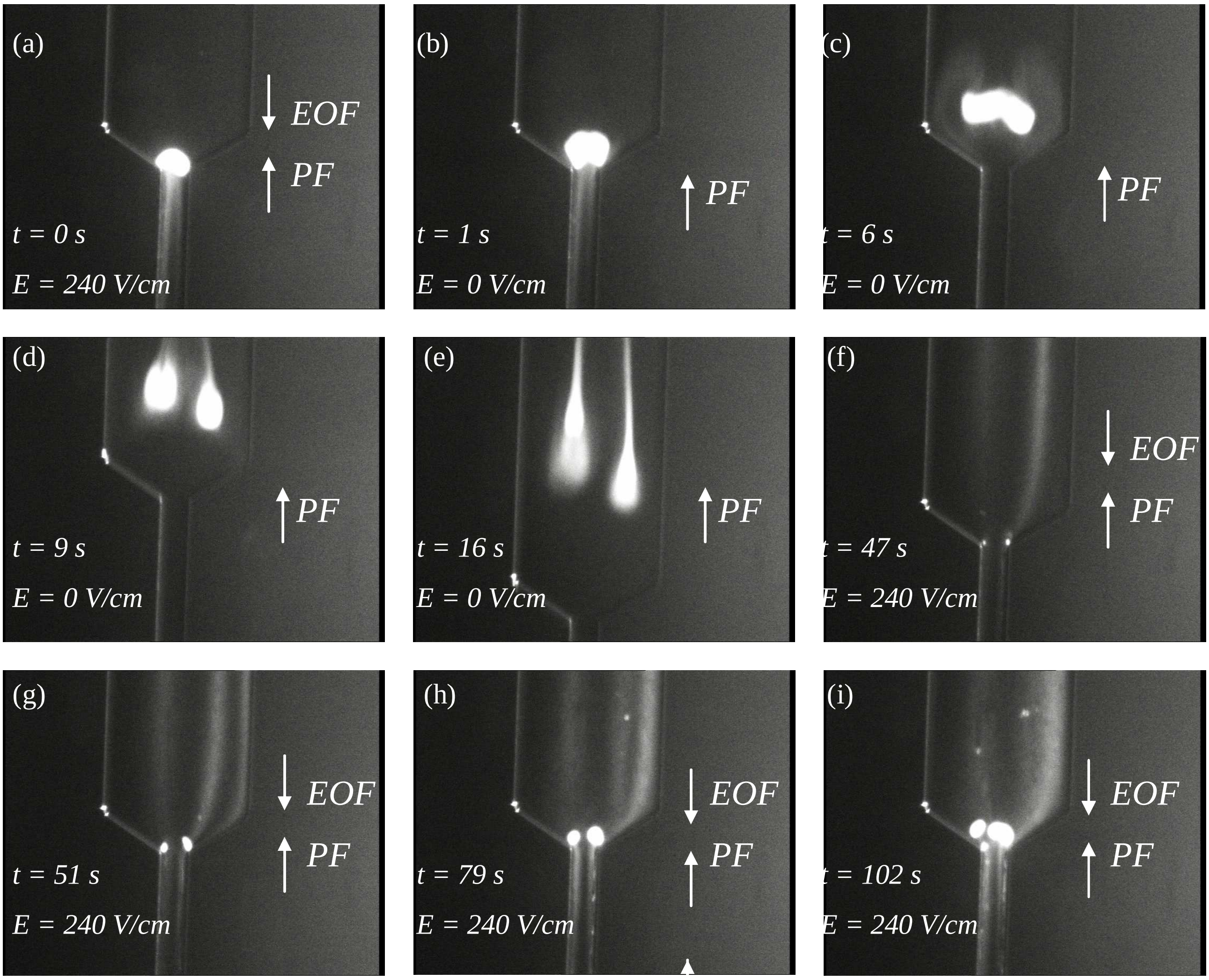

Figure 6.4
1 μM λDNA trap and release. t_i = 2 frames/s and Δp = 0.3 kPa (loading time = 90 s).

6.2.2.2 On-chip DNA Pre-treatment

DNA purification is an important step needed in addition to PCR and DNA separation for complete DNA analysis or molecular diagnostics (see section 6.1). Only a few examples of integrated microfluidic devices for DNA purification have been reported [2] [1, 8-11]. However, the on-chip pre-treatment process prior to DNA analysis still remains to be improved. The recirculating flows method presented in this work could be a viable tool for DNA cleanup. Since the efficiency of the trapping channel is dependent on species mobility, the trapping channel can be used as a selective trap of DNA from mixtures of enzyme, protein, or cell walls.

The electrophoretic mobility of λDNA should be in the range of 3 × 10^{-4} cm^2/Vs, which is similar to the μ_{beads} of SC beads (see Chapter 3). However, from the experimental results presented in the previous section for instance, a significant difference between the operating E and Δp required to generate recirculating flows of λDNA and SC beads was observed. It was observed that, for a given Δp, the E necessary to trap the λDNA is about two times higher when a 10 mM sodium tetraborate buffer (pH 9, $\mu_{EOF} \cong 6x10^{-4}$ cm^2/Vs) is used. This means that the apparent electrophoretic mobility of λDNA seems to be slightly higher in this system. A preliminary experiment using 2-μm SC beads and 0.5-μm fluoresbrite YG carboxylate beads (0.5-μm fc bead) (Polysciences), showed that trapping of these beads is highly selective with respect to apparent electrokinetic mobility. The apparent mobility of the 0.5-μm fc bead was not measured. However, it was observed that their μ_{beads} is high enough that the flow against the EOF under conditions where 2-μm SC beads are recirculating at the trapping channel. This preliminary experiment indicates that the trapped molecules of λDNA could also be selectively trapped, for two reasons:

1) species like enzymes, cells walls, etc…, with higher apparent electrokinetic mobility than the λDNA and the μ_{EOF}, should undergo electrophoretic "stripping" in the trapping channel.
2) the trapped λDNA is continuously perfused by the buffer driven by EOF (see Chapter 4 and Chapter 5) ensuring that species with an apparent mobility lower than the apparent mobility of the λDNA are flushed away through the trapping channel .

The fact that the molecules of λDNA recirculate at the trapping channel before forming localized clusters (see section 6.2.2) implies that they change direction with a certain frequency in their elongated form. This process is reminiscent of systems like slab gel pulsed-field gel electrophoresis (PFGE) and pulsed-field capillary gel electrophoresis (PFCGE). The principle of these systems consists of alternatively changing the orientation and/or the polarity of the *E*. At each modification, the DNA molecules have to reorient along the lines of the new *E*. The time of this reorientation is proportional to the length of the molecules. Each reorientation induces a delay of the migration proportional to molecular size. As was mentioned in section 6.2.2, the λDNA molecules move back and forth within the narrow section of the trapping channel, due to the presence of the bi-directional flow, before forming clusters at the entrance of the trapping channel. Figure 6.4 *(b)* illustrates a situation where the molecules of λDNA recirculate in the trapping channel. It would be interesting to see if it is possible to induce DNA separation by using a short trapping channel under conditions such that the efficiency of the trapping is low. In other words, *E* and Δp such that a bi-directional flow is formed in the narrow segments and the recirculating flows are only partially formed, allowing the DNA to be delayed but not trapped. In other words, the trapping channels are used to create a delay of DNA migration, based on their overall DNA mobility.

6.3 Preconcentration of B4F

In the next sections, the preconcentration of B4F (see Chapter 5) is investigated. As in the previous sections, the idea was to use the recirculating flows to induce the preconcentration.

Figure 6.5 shows the fluorescence signal recorded by the photomultiplier tube, located at the diverging element of the trapping channel in SB1, as a function of time. The signals recorded correspond to the B4F used for dynamic binding experiments with SC beads with B4F (see Chapter 3). When no counter pressure was applied, the fluorescent signal of the B4F was about 4 times lower than in the case with a counter pressure. Hence, the PMT signal appears to indicate that B4F is preconcentrated at the diverging element of the trapping channel.

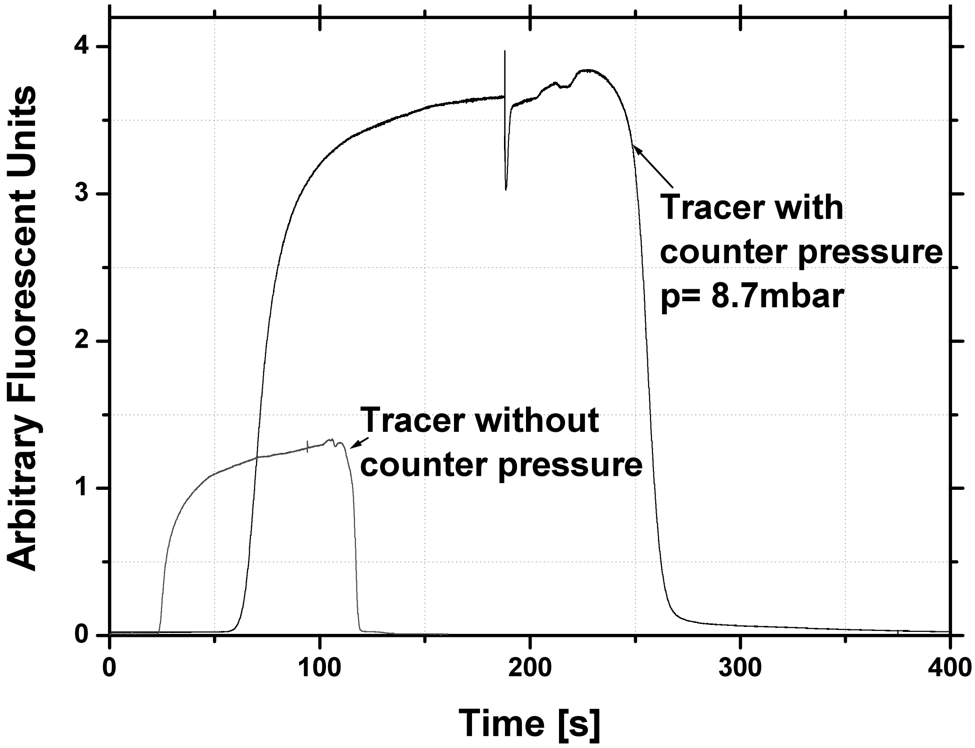

Figure 6.5
Reference curves (blank) of B4F loading with and without counter pressure. Comparison of this signal indicates that application of a counter pressure (0.7 kPa) can lead to a preconcentration of reagent at a channel expansion, as well as bead cluster formation. Note that EO-driven B4F (tracer) (E = 430 V/cm) arrives at the detector earlier when no pressure is applied.

To investigate this phenomenon in more depth, a fluorescent microscope was used to monitor the preconcentration of B4F. The chip operations are similar to those for DNA preconcentration (see section 6.2.1). The reservoir containing λDNA is simply replaced by a given concentration of B4F in 10 mM sodium tetraborate buffer pH 9. In the experiments illustrated by Figure 6.6, 2-µm SC bead and 1 µM B4F were loaded simultaneously from R_1 and R_3 of SB2 by EOF (E = 200 V/cm) in the presence of a counter pressure (0.5 kPa). The idea of this experiment is to use the beads to know when recirculating flows are generated and to follow the evolution of the B4F concentration under this condition. The electrophoretic mobility of the B4F (μ_{B4F}) was unfortunately not accurately measured. However, according to Figure 6.5 when counter pressure was not applied, we estimated μ_{B4F} to be -3.4 × 10^{-4} cm^2/Vs

which slightly smaller than the μ_{beads} of the 2-μm SC beads (~ -4×10^{-4} cm^2/Vs). It is then probable that when recirculating flows of beads are formed, the B4F is also influenced by this particular flow pattern. This is confirmed by the snap shots of the experiment in Figure 6.6.

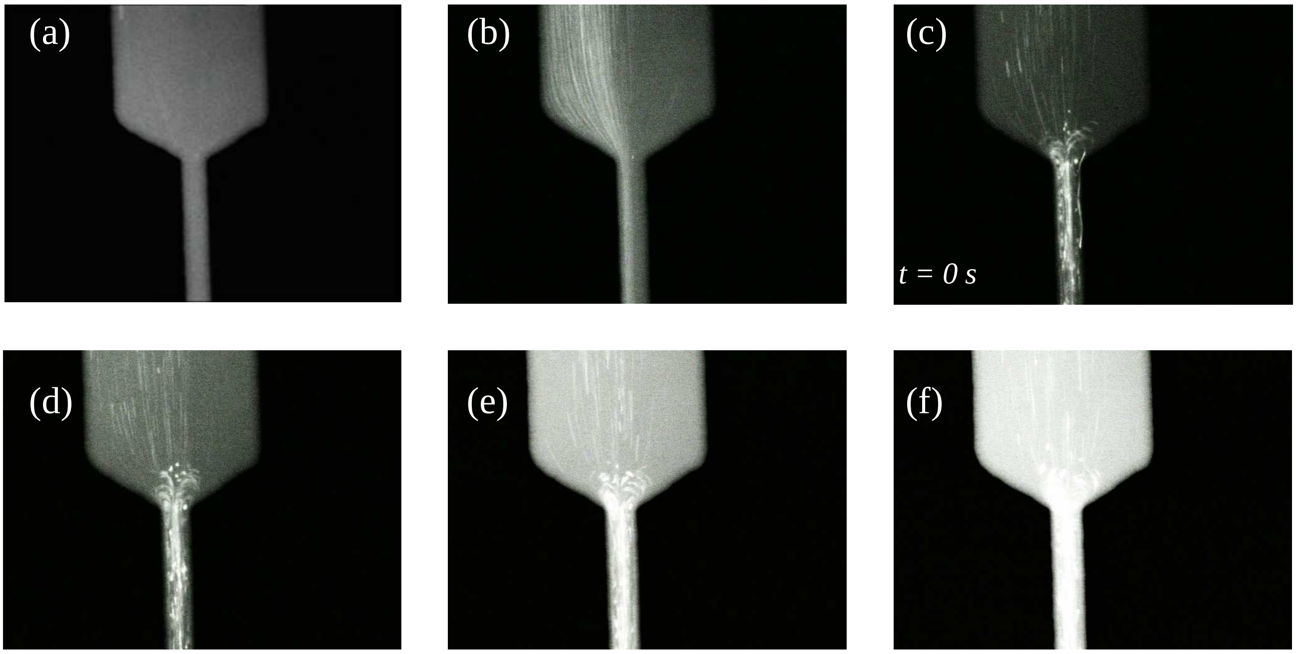

Figure 6.6
Comparison of the B4F fluorescent intensity when flow is uni-directional ((a) and (b)) and when recirculating flows are generated.

In Figure 6.6 (a) and (b), the beads and the B4F are driven by EOF (E = 200 V/cm, Δp = 0.5 kPa). When the beads reach the diverging element of the trapping channel, they are already fluorescent because of the binding of streptavidin with B4F. It can be also observed in Figure 6.6 (b) that, in the absence of recirculating flows, the beads flow occupy the left part of the microchannel (left lane) without overlapping the right part occupied only by B4F (right lane). On the other hand, because of diffusion, B4F is also present in the left lane explaining why the beads are fluorescent. As soon as the E (135 V/cm) is set such that recirculating flows of beads are generated, the beads start to overlap the right lane (Figure 6.6 (c) and (d)) and after few seconds, it can be observed that the fluorescent background signal increases dramatically (Figure 6.6 (e) and (f))).

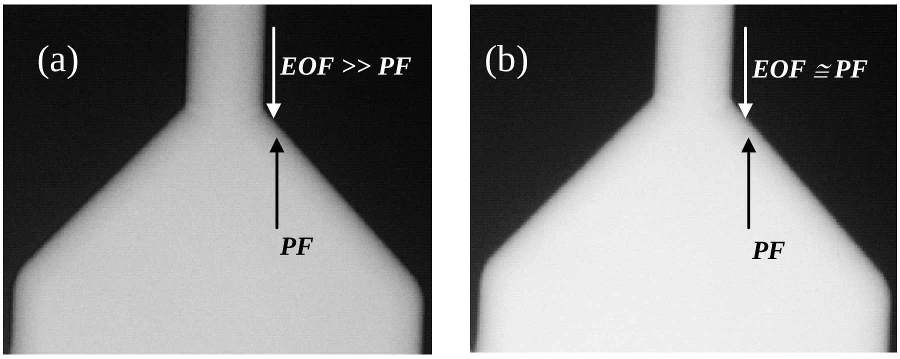

Figure 6.7
(a) 1 μM B4F loading (EOF >> PF) (b) Preconcentration of B4F by equilibrating EOF with PF.

An experiment using the same device and similar operating conditions but loading only 1 μM B4F confirms the previous observations. In Figure 6.7 (a), 1 μM B4F solution driven by EOF without counter pressure yields a certain signal intensity for a given E (E = 135 V/cm). Application of a counter pressure (0.5 kPa) induces an increase of the fluorescent signal intensity as illustrated by Figure 6.7 (b).

6.4 Conclusions

The trapping and the preconcentration of λDNA was carried out using the recirculating flow method. It was demonstrated in this Chapter that relatively large molecules of DNA (48 kbp), can be loaded up to the trapping channel using EOF. They can then be caught in the recirculating flows and preconcentrated by equilibrating the EOF with the PF, and be released from the trapping channel (either by increasing the E or by removing the PF component) without clogging. Clogging is not an issue, since the widths of the microchannels are at least 40 μm and the λDNA length is 16 μm. The trapping is also selective since it is highly dependent on the mobility of the species. The recirculating flow devices may then be used as a system to purify the trapped DNA molecules.

Preliminary experiments demonstrated that it was also possible to increase the concentration of B4F when recirculating flows are generated. These two examples of applications are in the first phases of development, but show the potential of the recirculating flow devices for bio(chemical) applications.

6.5 References

[1] Y. Takamura, T. Hayama, M. Ueda, Y. Baba, and Y. Horiike, "DNA Trap-and-release Element Employing Electric and Hydro Drag Force Fields for On-chip Pre-treatment," presented at Micro Total Analysis Systems 2002, Proceedings of the µTAS 2000 Symposium, Kyoto, Japan, 2002.

[2] H. Tian, A. F. R. Hühmer, and J. P. Landers, "Evaluation of silica resins for direct and efficient extraction of DNA from complex biological matrices in a miniaturized format," *Analytical Biochemistry*, vol. 283, pp. 175-191, 2000.

[3] R. Boom, C. J. A. Sol, M. M. M. Salimans, C. L. Jansen, P. M. E. Wertheim-van Dillen, and J. van der Noordaa, "Rapid and simple method for purification of nucleic acids," *Journal of Clinical Microbiology*, vol. 28, pp. 495-503, 1990.

[4] W. R. Boom, H. M. A. Adriaanse, T. Kievits, and P. F. Lens, "Process for isolating nucleic acid,"., 1990.

[5] G.-L. Lettieri, E. Verpoorte, and N. F. de Rooij, "Planar microfluidic devices for controlled vortex generation," presented at Transducers'01 Eurosensors XV, Munich, Germany, 2001.

[6] J. Han and H. G. Craighead, "Separation of long DNA molecules in a microfabricated entropic trap array," *Science*, vol. 288, pp. 1026-1029, 2000.

[7] J. Han and H. G. Craighead, "Characterization and optimization of an entropic trap for DNA separation," *Anal. Chem.*, vol. 74, pp. 394-401, 2002.

[8] L. Ceriotti, J. Lichtenberg, A. Dodge, N. F. De Rooij, and E. Verpoorte, "Combined nucleic acid extraction and enrichment in bead-packed plastic beds," presented at Micro Total Analysis Systems 2002, Kyoto, Japan, 2002.

[9] N. Y. Lee, M. Yamada, and M. Seki, "Integrated Microdevice for DNA Extraction from a Single Hair," presented at Micro Total Analysis Systems 2002, Kyoto, Japan, 2002.

[10] Q. e. a. Wu, "Monolithic sol-gel microchip device for efficient isolation of nucleic acid from clinical sample," presented at Micro Total Analysis Systems 2002, Kyoto, Japan, 2002.

[11] L.-S. Jang, D. R. Meldrum, and M. Holl, "An active mixer for microscale purification and sequencing reaction clean-up," presented at Micro Total Analysis Systems 2002, Kyoto, Japan, 2002.

7 Conclusion

7.1 On-Chip Controlled Micro Recirculating Flows at Small Re

The generation of on-chip controlled steady recirculating flows at Re < 0.01 Hs been demonstrated. These recirculating flows are formed when 1) an EOF and a PF are opposed in a device featuring diverging and converging elements 2) when the overall flow rate approaches zero (in other words, when a bi-directional flow is formed). Recirculating flows are formed at the diverging and converging elements while bi-directional flows are established in the straight microchannel segments. The recirculating flows are generated regardless of the Re, since there exists an infinite range of E and Δp for which bi-directional flow can be generated. Only the velocity distribution of the recirculating flows and the bi-directional flow is influenced by the Re. The main consequence of the formation of the recirculating flows is that EOF and PF cease to be independent. In fact, the recirculating flows are induced by the an increase of the adverse pressure gradients at the diverging and converging elements, due to the presence of EOF and PF, respectively. Based on the current monitoring method, a simple theoretical model that takes into account minor losses due to recirculating flows was developed. This model correlates the EOF with the PF and allows the averaged velocity of the flow as a function of the PF, the EOF and the geometry to be estimated. Recirculating flows of buffer and beads can be predicted if the respective mobilities are known. Furthermore, this model can be used for any kind of particles and biomolecules if the mobilities are known.

Micro polystyrene beads and CFD tools were successfully used to visualize and simulate the recirculating flow, respectively. By incorporating the μ_{beads} in the solver parameters, simulations of recirculating flow of beads were also performed. It was demonstrated that the size and the magnitude of the velocity distribution of the recirculating flows can be controlled by tuning either the E or the Δp, or by varying the geometry of the diverging and converging elements.

7.2 A New Flexible Method for on-chip Species Handling

The microfluidic system presented in this work shows a significant flexibility in the handling of particles using fluid flows only. It was demonstrated that a variety of particles and biomolecules can be trapped in the recirculating flows and released without problems of clogging or back flows. As an application of this phenomenon, a heterogeneous assay using 2-µm SC beads and FLB or B4F was carried out, as well as preliminary experiments for DNA extraction and biotin preconcentration.

7.2.1 On-chip Bead-based Reaction using Controlled Recirculating Flows

It was demonstrated that beads can be attracted and confined in a trapping channel using the recirculating flows. To obtain efficient bead trapping, that is to prevent beads from escaping the trapping channel, fully developed recirculating flows are required. The fully developed recirculating flows are defined as follow: bi-directional flows present in the narrow channels segments, overall net flow across the device dominated by EOF and recirculating flows at the diverging and converging elements. Under these conditions, beads can be trapped while continuously perfused by a liquid phase. Therefore, recirculating beads coated with a reagent can be sequentially perfused by an analyte and a buffer. As an application, the dynamic binding of SC beads and fluorescein-labelled biotin was carried out. Characterization of the binding showed that the forward rate constants and the efficiency of the binding were in good agreement with theoretical values for heterogeneous systems.

7.2.2 DNA Extraction and Preconcentration

The trapping of large molecules of DNA (λDNA, 48 kbp, 16 μm long) was performed using the recirculating flows in microchannels with typical widths of 40 μm and depths of 20 μm. The molecules of λDNA were trapped while continuously perfused by the buffer meaning that DNA is undergoing “electro-osmotic cleaning”. Molecules of DNA were trapped, preconcentrated and released without issues of clogging or instabilities due to eventual backflows. In essence, the trapping is selective with regard to the electrophoretic mobility of the species. It is proposed that the system can be used to clean, by electro-osmosis or electrophoretic means, molecules of DNA from proteins, enzymes or salts, if their mobilities are different from molecules of DNA.

Preliminary experiments demonstrated that it was also possible to increase the concentration of B4F when recirculating flows are generated. These two examples of applications are in the first phases of development but show the potential of the recirculating flow devices for bio(chemical) applications.

7.3 Outlook

Efforts will focus on the investigation of DNA extraction but also on DNA separation using the trapping channels to induce size-dependent migration rates.

A brief feasibility study will show whether cells (bacteria like E-coli) can be selectively trapped and separated using the recirculating flows.

Acknowledgments

First of all I would like to thank Prof. Nico de Rooij for giving me the opportunity to do this Ph.D Thesis. My special thanks to Prof. Elisabeth Verpoorte that introduced me to the world of analytical chemistry and to the multi-disciplinary and fascinating field of microfluidics. Thanks for your advices and guidance during the project. My gratitude to her and S. Koster for time given to read and corrections of this manuscript.

I would like to thank all members of the IMT for their help in the lab and for the pleasant atmosphere and working environment. A special thanks to J. Lichtenberg for his help in the manufacturing of the power supply, A. Dodge for his continuous encouragement and for the pictures of Figure 3.16… and the other members of the famous µTAS team: Alexandra Homsy, Laura Ceriotti, Roose, Vincent Linder, Antoine Daridon, Prof. Takayuki Shibata, Prof. Teruo Fujii, Anna-Maria Spehar, Thomas Hug and Anpan Han. I also really appreciated the discussions with Peter van der Waal. Thanks also to the highly skilled technical teams: il "Cavaliere" Gianni Mondin, Sylvain Jeanneret, Sabina Jenny, Pierre-André Clerc, Nicole Hegelbach-Guye, Sylviane Pochon, José Vaquera, Giovanni Bergonzi, Edith Millotte and Pierre-André Kuenzi.

I would like to thank the different people with whom I shared my office during my thesis and with whom I recall with pleasure the great moment of scientific discussion and fun: Sebastian Gautsch "the Martian" (Seb, I am the hairy guy that was sitting in front of you during 4 years and I also spent all my education with you in case…☺), Vincent Auger (thanks for your advices in biology and for making me laugh a lot every morning…☺), Luca "Bestial" Berdondini and "the" Patricks (Weber and Carazzetti). Thanks also to Laure Aeschimann, Phuong Quyên Pham, Giovanni Egidi, Philipe Dubois, Claudio Novelli (Forza Napoli…!), Olivier Guenat, Massoud Dadras, Mireille Leboeuf, Florence Rohrbach, Milena Koudelka-Hep, Urs Staufer, Terunobu Akiyama, Danick Briand, Bart van der Schoot, Cornel Marxer, Marc Boillat, Winston

Sun, Maurizion Gullo, Raphael Imer, Tobias Kraus, Andreas Kuoni, Thomas Overstolz, Daniel Parrat, Yves Petramand, Kaspar Sutter, Michael Zickar, Jean-Charles Fiaccabrino and the ”three magic mentors” G. Schürmann, S. Roth and L. Dellmann.

I also express my gratitude to Dr. T. Boone who gave me the opportunity to do an internship at Aclara Biosciences in California. Thanks also Dr. A. Ricco and all the people I met during this fantastic period. I would like to thank Yves-Alain Peter and his wife Marie as well as Antoine Daridon and his wife Karine for their hospitality in San Francisco.

Finally, a big “thank you” to my girlfriend Mélanie, to my sisters Antonella and Katia and to my parents and friends who supported me during all my studies.

This work would not have been possible without the financial support of the Centre Suisse d’Electronique et de Microtechnique SA.